DISS. ETH NO. 24221

THERMAL TRACER TOMOGRAPHY TO CHARACTERIZE AQUIFER HETEROGENEITY

A thesis submitted to attain the degree of

DOCTOR OF SCIENCES of ETH ZURICH

(Dr. sc. ETH Zurich)

presented by

MÁRK SOMOGYVÁRI

M.Sc. of Geophysics, Eötvös Loránd University, Budapest

born on 07.07.1990

citizen of Hungary

examination board

Prof. Dr. Simon Löw, examiner
Prof. Dr. Peter Bayer, co-examiner
Dr. Ralf Brauchler, co-examiner
Prof. Dr. Olivier Bour, co-examiner

2017

DISS. ETH NO. 24221

THERMAL TRACER TOMOGRAPHY TO CHARACTERIZE AQUIFER HETEROGENEITY

A thesis submitted to attain the degree of

DOCTOR OF SCIENCES of ETH ZURICH

(Dr. sc. ETH Zurich)

presented by

MÁRK SOMOGYVÁRI

M.Sc. of Geophysics, Eötvös Loránd University, Budapest

born on 07.07.1990

citizen of Hungary

examination board

Prof. Dr. Simon Löw, examiner
Prof. Dr. Peter Bayer, co-examiner
Dr. Ralf Brauchler, co-examiner
Prof. Dr. Olivier Bour, co-examiner

2017

“Reality is frequently inaccurate.”

Douglas Adams

Abstract

Tomographic methods in hydrogeology are developed to characterize the spatial variability of the hydraulic properties of aquifers. These methods have successfully utilized pressure signals and solute tracers, but only few studies considered using thermal tracers in a tomographic setup. Although density effects and strong diffusion suggest that heat is not an ideal choice for investigations, the ease of signal detection and its harmlessness to the environment makes this tracer appealing, especially for tomographic utilization.

Thermal tracer tomography employs repeated thermal tracer injections at different injection depths and distributed temperature measurements to map the hydraulic conductivity distribution of aquifers. The irregular propagation of the injected thermal signals may reveal the heterogeneous aquifer structure by highlighting the dominant transport pathways. This thesis presents two different approaches to interpret tomographic thermal tracer data and thus to characterize porous and fractured aquifers.

The travel-time based thermal tracer tomography approach exploits the similarities between tracer and hydraulic tomography. The similarity in experimental design and approximation of signal propagation allows the use of the same inversion algorithms for both methods. After identifying the tracer travel times between the different source-receiver combinations, the travel time dataset is inverted by standard tomographic solvers that use the ray-tracing technique known from seismic tomography. The inversion yields a tomogram, a grid-based continuous distribution of the mean tracer velocity, which is then converted to a hydraulic conductivity distribution using Darcy`s Law. The inversion also provides estimations on the fastest transport trajectories, which are used to estimate the reliability of the tomogram in the form of a null-space energy map.

The method was developed and tested on an aquifer analog dataset, a synthetic model of a porous aquifer. Three 2-D cross-well profiles and one 3-D multi-well profile with different characteristic heterogeneities were examined. Continuous thermal tracer injections repeated in multiple isolated well intervals were simulated. Early time diagnostics of the observed temperature breakthrough curves were used to minimize distortions due to density and viscosity changes. The resulting hydraulic conductivity tomograms demonstrated that thermal tracer tomography was suitable to reconstruct the aquifer structure and to characterize the high permeability zones, where dominant transport takes place. Sensitivity analysis revealed that the results were not dependent on the temperature of the injection, but the tomograms

became distorted at very low and high injection rates. The limits of thermal tracer tomography were further investigated using diverse hydraulic and thermal conditions in order to derive a suitable application window. These investigations showed that thermal tracer tomography would be applicable to any advection-dominated aquifer if the utilized injection provided detectable temperature signals at the observation well.

To validate the method, a tomographic thermal tracer experiment was conducted in a thoroughly examined fluvial aquifer in northeast Switzerland. Heated water was injected as a pulse temperature signal via a double packer system under forced gradient conditions. In contrast to continuous injection, long temperature recovery periods were not required between the repeated injections when pulse injection was used. However, the amplitudes of the induced temperature signals were much smaller, requiring high-resolution temperature measurements and limiting the scale of reconstruction. A small 2-D cross-well profile was investigated with the proposed experimental design. The obtained hydraulic conductivity tomogram was validated with the results of the findings from previous field investigations at the same site. The reconstructed profile showed similar heterogeneous features as previous hydraulic and tracer tests with similar inverted hydraulic conductivity values. The experiment demonstrated the potential of the travel-time-based thermal tracer tomography method to characterize porous aquifers.

For hard-rock aquifer characterization a different approach was developed, using discrete fracture networks to model the fractured media. These type of models provide realistic representations of the fracture network geometry, and may be generated based on the statistical properties of the fractured rock, such as fracture intensity or fracture length distribution. The calibration of these models is challenging because the number of fractures, which determine the number of model parameters, is unknown prior to the inversion. Transdimensional inversion methods such as the reversible jump Markov Chain Monte Carlo algorithm can overcome this challenge by providing model calibration with variable parameter dimensions. The method was applied to the example of conservative tracer tomography, but it could be used to interpret any tomographic data after adjusting the forward model. Flow and tracer transport were modelled via a fast finite difference model. The proposed DFN inversion method iteratively evolved DFN realizations by geometry updates to fit the observed tomographic data evaluated by the Metropolis-Hastings-Green acceptance criteria. The method was suitable to evaluate DFN realizations after updates when the dimensionality of the model had changed due to fracture addition or deletion. The

stochastic algorithm created an ensemble of thousands of DFN realizations that can be utilized for identification of fractures in the aquifer. In the presented hypothetical and outcrop-based case studies, cross-sections between boreholes were investigated. The procedure successfully localized major transport pathways in the DFN and separated fracture zones with different densities. The ensemble was further analyzed in the form of fracture probability maps and by multidimensional scaling.

This PhD research project demonstrates that thermal tracer tomography is an investigation method with great potential. The proposed travel-time-based tomographic inversion is a fast and robust algorithm to identify the heterogeneous aquifer structure, and to characterize detected heterogeneities. The presented experimental design could be a cost-effective alternative for solute tracer tomography. Finally, the transdimensional discrete fracture network reconstruction may allow thermal tracer tomography to characterize hard-rock aquifers in the field.

Zusammenfassung

Tomographische Methoden in der Hydrogeologie wurden entwickelt, um die räumliche Variabilität der hydraulischen Eigenschaften in Grundwasserleitern zu bestimmen. Diese Versuche wurden bisher als hydraulische oder Tracertomografie durchgeführt, aber nur selten mit Hilfe von thermischen Tracern. Obwohl thermische Tracer auf Grund von Dichte- und Diffusioneffekten nicht ideal verhalten, machen es die einfache Signalerfassung und die Umweltfreundlichkeit zu einer erfolgsversprechenden Methode.

Bei der thermischen Tracertomografie werden thermische Signale in verschiedenen Injektionstiefen eingebracht und verteilte Temperaturmessungen durchgeführt. Die ungleichmässige Ausbreitung der eingebrachten Signale bildet die heterogene Leitfähigkeitsverteilung im Grundwasserleiter ab und hebt somit die dominanten Transportwege hervor. In dieser Arbeit werden zwei unterschiedliche Ansätze zur Interpretation thermischer Tomografiedaten, als Methode zur Charakterisierung von porösen und geklüfteten Grundwasserleitern vorgestellt.

Die laufzeitbasierte thermische Tracertomografie nutzt die Ähnlichkeiten im experimentellen Aufbau und der Signalausbreitung zwischen Tracer und hydraulischer Tomographie. Dies ermöglicht die Verwendung der selben Inversionsalgorithmen. Nach der Bestimmung der Tracerlaufzeiten zwischen den verschiedenen Injektions- und Messintervallen werden diese mittels Standard-Tomographie-Solver, beruhend auf der seismischen Raytracing-Technik, invertiert. Die Inversion liefert eine gitterbasierte kontinuierliche Verteilung der mittleren Tracergeschwindigkeit als Tomogramm,, das auf Grundlage des Darcy-Gesetzes in hydraulische Leitfähigkeitsverteilungen umgewandelt wird. Zusätzlich werden durch die Inversion die schnellsten Transportwege ermittelt und zur Abschätzung der Zuverlässigkeit des Tomogramms mittels einer Nullraum-Energiekarte verwendet.

Die Methode wurde auf einem synthetischen Datensatz eines porösen Grundwasserleiters entwickelt und getestet. Dazu wurden drei Profile zwischen je zwei Messstellen und ein 3D Modell zwischen mehreren Messstellen mit verschiedenen Heterogenitäten untersucht, indem in mehreren isolierten Bohrlochintervallen wiederholt kontinuierliche thermische Injektionen simuliert wurden. Mit Hilfe der beginnenden Temperaturdurchbruchskurve wurden durch Dichte- und Viskositätsänderungen erzeugte Verzerrungen minimiert. Die daraus resultierenden hydraulischen Leitfähigkeitstomogramme zeigen, dass die thermische Tracertomografie geeignet ist, die Struktur des Grundwasserleiters zu rekonstruieren und

hoch permeable Transportzonen zu charakterisieren. Eine Sensitivitätsanalyse zeigt auf, dass die Injektionstemperatur einen geringen Einfluss ausübt, jedoch sehr niedrige und hohe Injektionsraten die Tomogramme deutlich verzerren. An Hand verschiedener hydraulischer und thermischer Szenarios wurde ein Anwendungsbereich der thermischen Tracertomographie definiert. Die Untersuchungen zeigen, dass die thermische Tracertomographie auf jeden advektionsdominierten Grundwasserleiter anwendbar ist, falls in den Messintervallen Temperatursignale nachweisbar sind.

Zur Überprüfung der Methode wurde eine thermische Tracertomografie in einem gut untersuchten fluvialen Grundwasserleiter in der Nordostschweiz durchgeführt. Erwärmtes Wasser wurde unter vorgegebenem Gradienten in ein von Packern begrenztes Intervall injiziert. Im Gegensatz zur simulierten kontinuierlichen Injektion war keine lange Temperaturerholung zwischen den Dirac-Injektionen notwendig. In Folge geringerer Amplituden der gemessenen Temperatursignale war die tomografische Rekonstruktion trotz hochauflösender Temperaturmessungen räumlich auf ein kurzes Profil zwischen zwei Messstellen begrenzt. Das invertierte hydraulische Leitfähigkeitstomogramm weist eine ähnliche hydraulische Leitfähigkeitverteilung, wie frühere hydraulische und Traceruntersuchungen am gleichen Ort auf. Das Experiment verdeutlicht das Potenzial der laufzeitbasierten thermischen Tracertomografie zur Charakterisierung poröser Grundwasserleiter.

Für die Charakterisierung von geklüfteten Festgesteinsaquiferen wurde ein Ansatz unter Nutzung diskreter Kluftnetzwerker entwickelt. Dieser Ansatz basiert auf, statistischen Verteilungen der Geometrie des Kluftnetzwerks, wie Kluftabständen oder Kluftlängen. Die Kalibrierung dieser Modelle ist schwierig, da die Anzahl der Klüfte und somit die Anzahl der Modellparameter vor der Inversion unbekannt ist. Transdimensionale Inversionsmethoden, wie der auf reversiblen Sprüngen basierende Markov Chain Monte Carlo Algorithmus, können die Modellkalibrierung mit variablen Parameterabmessungen durchführen. Die Methode wurde am Beispiel der konservativen Tracertomographie angewandt, bietet aber auch das Potenzial, nach der Kalibrierung der Vorhersage andere tomographische Daten zu interpretieren. Das Fliessfeld und der Tracertransport wurden mittels eines effektiven Finite-Differenzen-Modells modelliert. Die Inversionsmethode passt die DFN-Geometrieiterativ an die beobachteten tomografischen Daten an, die durch die Metropolis-Hastings-Green-Akzeptanzkriterien ausgewertet wurden. Diese Methode wertet die durch die Erhöhung oder Verringerung der Kluftanzahl induzierten Änderung der Dimensionalität des Modells

selbstständig aus. Mit diesem stochastischen Algorithmus können mittels Tausender DFN-Realisierungen Klüfte in Festgesteinsaquiferen identifiziert werden. In den hier vorgestellten hypothetischen und realen Aufschlüssen wurden Profile zwischen Bohrlöchern untersucht. Das Verfahren lokalisierte wichtige Transportwege im DFN und unterscheidet Zonen unterschiedlicher Kluftdichte. Die Realisationen wurden ferner durch Kluftwahrscheinlichkeitskarten dargestellt und durch mehrdimensionale Skalierung analysiert.

Dieses Dissertationsprojekt zeigt, dass die thermische Tracertomographie eine Untersuchungsmethode mit großem Potenzial ist. Die entwickelte laufzeitbasierte tomographische Inversion ist ein schneller und robuster Algorithmus, um die heterogene Grundwasserleiterstruktur zu identifizieren und Heterogenitäten zu charakterisieren. Das dargestellte experimentelle Design stellt eine kostengünstige Alternative zur solute Tracertomographie dar. Und ausserdem ermöglicht die thermische Tracertomographie transdimensionale diskrete Bruchnetzwerke zu rekonstruieren und Festgesteinsaquifere zu charakterisieren.

Table of contents

1 Introduction to thermal tracer tomography

1.1 Introduction

Characterizing the heterogeneous structure of aquifers represents arguably one of the most important challenges in hydrogeology. Further improving our ability to describe, quantify, and model heterogeneity is, therefore, an active field of research, ranging from lab- and field-scale experiments to numerical studies. In porous media, heterogeneities can modify flow patterns (Freeze and Witherspoon, 1967) and strongly control the transport of solutes (Dagan, 1988; Feehley et al., 2000; Jussel et al., 1994) and heat (Hidalgo et al., 2009). The impact of heterogeneity is also significant in fractured aquifers where most of the flow and transport only take place within discrete, permeable fractures (Berkowitz, 2002; Neuman, 2005). Developing understanding of the heterogeneous structure of aquifers is also important to many applications, such as water resources, where the installation of water wells needs to be optimized according to the most permeable units encountered. By capturing heterogeneities, it is possible to provide better predictions for contaminant propagation, more reliable estimation of the geothermal potential, and more accurate identification of the dominant transport routes.

Different techniques have been developed for the characterization of heterogeneous aquifers. Among them, the use of heat as a tracer has been established for decades, but its potential has only started to be further evaluated in recent years. By combining the interpretation of multiple thermal tracer signals, it is possible to reconstruct the heterogeneous structure of an aquifer. Using a tomographic source-observation setup, the pathways of the thermal signals are optimized to cover the major part of the aquifer domain. This technique is known as thermal tracer tomography.

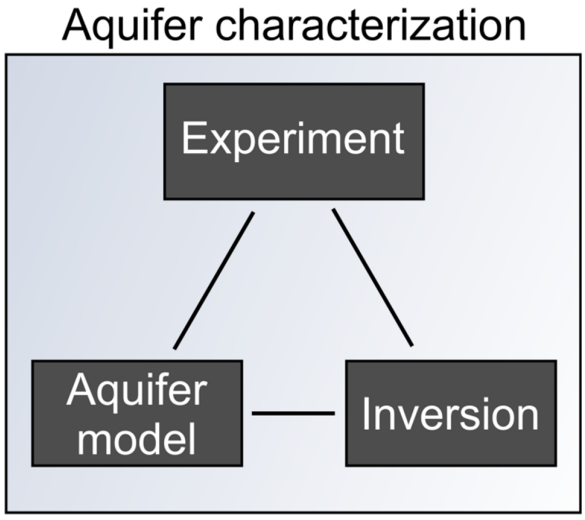

Figure 1-1. Key elements of aquifer characterization.

Similar to other standard field investigation methods in hydrogeology, thermal tracer tomography is indirect. This means that the hydraulic properties are derived by inversion of data provided from a set of field observations. The indirect observations are related to the hydraulic properties, and this relation can be expressed by applying an operator on the model parameters of the aquifer, which reads as:

$$\xi = f(\theta) \qquad (1\text{-}1)$$

where ξ is the vector of the observed data (experiment), θ is the model parameter vector (aquifer model) and f is the so-called forward operator (forward model of the inversion), which are the three main components of aquifer characterization (Figure 1-1.). Equation (1-1) is known as the objective formulation of the inverse problem (Aster et al., 2013; Menke, 1984). Solving this equation for θ is inversion, which reads as:

$$\theta = f^{-1}(\xi) \qquad (1\text{-}2)$$

However, in reality the forward operator is almost never invertible even when it is linear. Inversion methods thus simulate the observation for an initial parameter vector first, and then try to modify it to converge the simulated observations to the real ones. The forward model approximates the physics of the experiment and the aquifer model is only an approximate representation of the real geological aquifer structure. As such, an exact fit with the observed data is not possible. Complications also arise when the number of parameters exceed the number of observations; the inverse problems is ill-posed with unstable solutions (Aster et al., 2013).

For thermal tracer tomography, the forward model reads as:

$$T_{obs}(x_{obs}, t) = f(K(x), \phi(x), \lambda(x), C(x), T(x,t), T_{inj}(x,t)) \qquad (1\text{-}3)$$

The temperature evolution (T_{obs}) at the observation points (x_{obs}) is a function of the hydraulic (hydraulic conductivity (K), porosity (ϕ)) and thermal properties (thermal conductivity (λ), heat capacity(C)), the used thermal tracer signals (T_{inj}) and the thermal state of the aquifer ($T(x,t)$).

Aquifer characterization with thermal tracer tomography requires solving this complex inverse problem for the hydraulic parameters. In the following, the concepts and methods that were used in this research project to solve the inverse problem of thermal tracer tomography are introduced. First, the experimental concept is presented, then different modelling approaches are shown to parametrize porous and fractured aquifers. Finally, inversion methods used to interpret the thermal tracer tomography are introduced.

1.2 Thermal tracer tomography

Classic hydraulic investigation methods such as pumping tests, slug tests and tracer tests are the standard tools for aquifer characterization. In recent decades, however, new high-resolution techniques have emerged, which provide significantly more information about the aquifer structure.

Tomographic methods, such as hydraulic tomography or tracer tomography, are designed to map aquifer heterogeneities and to identify dominant transport routes. Meanwhile, growing interest in geothermal energy use has brought thermal tracer tests into focus. The combination of thermal tracer tests and tracer tomography is thermal tracer tomography, a novel investigation method in aquifer characterization.

1.2.1 Thermal tracers

Tracers represent a broad family of investigation methods to indicate the transport routes in groundwater flow systems. Tracer tests are among the most established techniques to provide insight into the hydraulic properties of aquifers and to reveal dominant transport pathways of flow.

Thermal tracer testing is not a new concept. The intensive research on heat storage in the 1980s revealed the potential of using temperature for aquifer characterization (Keys and

Brown, 1978; Molz et al., 1981; Sauty et al., 1982). Even so, it did not become a popular method until the 2000s, when the interest in geothermal aquifer energy use required a better understanding of heat transport in groundwater systems.

Thermal tracers have some appealing properties for practical use. Changes in temperature can be monitored inside the aquifer in real time without taking groundwater samples. Modern temperature sensors provide temperature values with high accuracy, while their costs are low compared to other scientific equipment. These measurements have significantly lower noise than any lab or onsite measurements on solute concentrations. Background noise is also less of a problem, because natural changes in the groundwater temperature are slow and their effect can be easily removed from the observed data by frequency filtering or by using baseline measurements.

Still, thermal tracers have some significant drawbacks. Physical properties of rocks and fluids are temperature dependent; changes in temperature will modify the density and the viscosity of the pore fluid and even the hydraulic conductivity of the aquifer. Furthermore, when the introduced temperature difference is above a certain limit, the change in water density initiates buoyancy driven flow and alters the existing flow field. If the density difference within the fluid is higher than 0.8 kg m^{-3}, the flow field changes (Schincariol and Schwartz, 1990). In an aquifer where the in-situ temperature is 10˚C, this limit value is 8˚C, as it was shown by Ma et al., (2012). This tight limit means that in most cases, thermal tracer experiments take place in a buoyancy-altered flow regime, and in order to obtain information about the aquifer, these alterations have to be considered in the interpretation of measurements.

In addition, heat is not only transported in the pore spaces, as other tracers, but in the rock matrix as well by thermal diffusion. Heating the aquifer matrix slows down the heat transport. This effect is known as thermal retardation (Molson et al., 1992; Palmer et al., 1992), which can be quantified and corrected based on thermal tracer travel times (Shook, 1999). Heat exchange with the aquifer matrix also strongly attenuates the temperature signals. This effect should be considered by the choice of heat sources, to provide a signal that can be detected at the observation points.

Two main types of thermal tracer tests exist: passive thermal tracer tests, where the natural variability of temperature is utilized, and active thermal tracer tests, where temperature anomalies are artificially induced. Passive thermal tracer tests are generally used for large-

scale investigations (Saar, 2011), but they are also suitable for the characterization of fractured media. Klepikova et al., (2014) presented a concept, where after pumping in a hard-rock aquifer, fractures could be localized and characterized using borehole temperature data.

Active thermal tracer tests most commonly use injected heated or cooled water with respect to the in-situ temperature. The propagation of the generated temperature anomaly, called thermal plume, is used to assess the hydraulic conductivity of the aquifer. An overview of active thermal tracer tests reported in the literature is shown in Table 1-1.

Table 1-1. Thermal tracer tests reported in literature

Location	Aquifer type	Source type	Signal type	Test type	Observation type	Reference
Texas, USA	porous	well screen	diurnal	tracer test	temperature log	Keys and Brown (1978)
Mobile, USA	porous	well screen	continuous	storage test	temperature sensor	Molz et al., (1981)
Bonnaud, France	porous	well screen	boxcar	tracer test	temperature sensor	Sauty et al., (1982b)
Toronto, Canada	porous	well screen	boxcar	storage test	temperature sensor	Palmer et al., (1992)
Kansas, USA	porous	well screen	continuous	tracer test	DTS	Macfarlane et al., (2002)
Gent, Belgium	porous	well screen	boxcar	storage test	temperature sensor	Vandenbohede et al., (2011)
Hanford, USA	porous	well screen	pulse	tracer test	temperature sensor	Ma et al., (2012)
Plomeur, France	fractured	point (fracture)	boxcar	tracer test	DTS	Read et al., (2013)
Hermalle, Belgium	porous	well screen	continuous	tracer test	temperature sensor	Wildemeersch et al., (2014)
Lauswiesen site, Germany	porous	well screen	pulse	tracer test	temperature sensor	Wagner et al., (2014a)
Plomeur, France	fractured	well screen	ambient	passive tracer test	temperature sensor	Klepikova et al., (2014)
Widen site, Switzerland	porous	point	continuous	tracer test	temperature sensor	Schweingruber et al., (2014)
Ferrara, Italy	porous	point	pulse	tracer test	temperature sensor	Colombani et al., (2015)
Lauswiesen site, Germany	porous	tomographic	continuous	tracer tomography	temperature sensor	Doro et al., (2015)
Altona Flat Rocks, USA	fractured	point	continuous	tracer test	DTS + sensor	Hawkins et al., (2015)
Hermalle, Belgium	porous	well screen	continuous	tracer test	DTS + ERT	Hermans et al., (2015)
Castricum, Netherlands	porous	heating cable	in situ heating	tracer test	DTS	Bakker et al., (2015)
Widen site, Switzerland	porous	tomographic	pulse	tracer tomography	temperature sensor	Somogyvári et al., (2016)
sandbox	porous	well screen	pulse	tracer test	temperature sensor	Djibrilla Saley et al., (2016)
UFZ test site, Germany	porous	heating cable	in situ heating	tracer test	DTS + sensor	Seibertz et al., (2016)

The most common thermal tracer injection type is the continuous injection of water warmed by a heating device (Doro et al., 2015; Hawkins et al., 2015; Hermans et al., 2015; Macfarlane et al., 2002; Molz et al., 1981; Schweingruber, 2014; Wildemeersch et al., 2014). Continuous injection provides the strongest temperature signals possible. This benefit makes the method very popular, although the operation costs can be very high and maintaining constant injection could be challenging under field conditions. Theoretically, continuous thermal tracer injection provides a Heaviside temperature signal. If the injection is switched to cold water after a period of time, a second, cold thermal front is created. In this case, the injection follows a boxcar signal (Palmer et al., 1992; Read et al., 2013; Vandenbohede et al., 2011).

A different solution is to provide a fix amount of heated water in a tank and inject it as a single impulse (Colombani et al., 2015; Djibrilla Saley et al., 2016; Ma et al., 2012; Wagner et al., 2014b). This is a cost-effective alternative of continuous injection, but it is important to inject sufficient amount of heat which is detectable at the observation points.

Correspondingly, natural surface water bodies can be used as periodic temperature signals, as their temperature follows the diurnal cycle. After injection, periodic temperature variation provides a phase-shifted signal at the observation points, and the value of the phase shift can be related to heat transport (Keys and Brown, 1978).

Instead of injection, it is also possible to heat the water of the aquifer in situ by using a heating coil or cable (Bakker et al., 2015; Seibertz et al., 2016). Note that only very smooth temperature signals can be generated by this method. This makes them more favorable for diffusion related investigations, like thermal response tests (Raymond et al., 2011; Wagner et al., 2014a).

The implementation of all the abovementioned active thermal tracer test sources are technically more challenging than solute tracer tests, as they require a large amount of thermal energy on-site. Monitoring the propagation of the thermal tracer is much easier. With distributed temperature sensors (DTS) the temperature can be measured along a borehole (Bense et al., 2016). DTS uses the physical phenomenon that the light backscattering behavior of a fiber optic cable is temperature dependent. Since with this method it is possible to measure temperature along very long fiber optic cables, DTS systems are popular in a broad range of disciplines (Coleman et al., 2015; Hermans et al., 2015; Leaf et al., 2012; Read et al., 2015). Although significant developments have occurred in recent years, these

devices still fall behind the temperature resolution of traditional sensors. DTSs are very expensive, and they are more suitable for long-term or permanent installations.

A distributed measurement configuration can also be obtained by using multiple individual temperature sensors. Traditional temperature sensors provide very accurate measurements at one point. In addition, as they are commonly used for a wide variety of applications, they are very cheap and reliable (Saar, 2011).

1.2.2 Tracer tomography

Traditional tracer tests are integrative methods providing average values of the hydraulic parameters while considering the aquifer as one homogeneous domain. To localize heterogeneities and map the spatial distribution of the hydraulic properties, tomographic tracer methods have emerged in the last two decades.

The concept of tomography is widely used in many disciplines, from medical research to seismic exploration. In tomography, closed systems are accessed by penetrating signals, and the travel time of the signals is related to the physical properties of the domain. A tomographic source-receiver measurement array provides a large number of signal pathways to dissect the domain between the sources and receivers. Hence, the collected travel time dataset contains information on the spatial distribution of the physical properties.

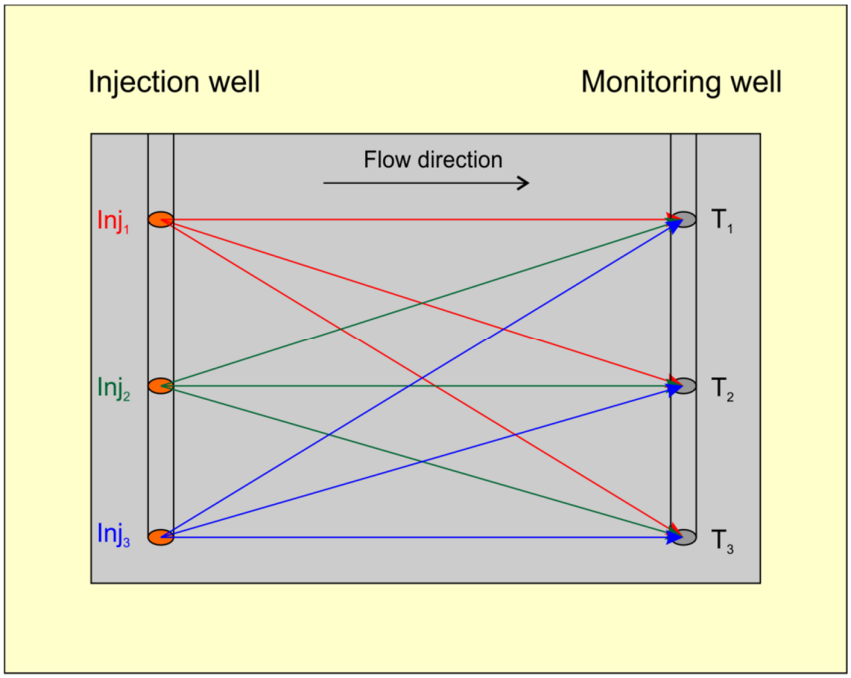

Figure 1-2. Concept of tracer tomography.

Figure 1-2 summarizes the concept of tomography. Point sources and point receivers are used in a tomographic measurement array. For aquifer characterization the propagation of the chosen signals should depend on the hydraulic parameters of the aquifers.

Hydraulic tomography uses pressure signals generated by short-term pumping tests or slug tests (Butler et al., 1999). The propagation of the generated pressure front is related to the hydraulic diffusivity of the aquifer. As these experiments can be performed with the same instrumentation used for classic pumping or slug tests, hydraulic tomography is widely used (Brauchler et al., 2013b).

For transport-related investigations, tracer tomography techniques have been developed in parallel with hydraulic tomography. As these methods require repeated tracer injections and multilevel sampling, they are more difficult to execute. Therefore, only a few tracer tomography studies are reported in the literature (Brauchler et al., 2013a; Datta-Gupta et al., 2002; Deuber et al., 2017; Illman et al., 2010; Jiménez et al., 2016; Vasco and Datta-Gupta, 1999).

Vasco and Datta-Gupta (1999) presented a numerical approach to reconstruct the hydraulic parameters of an aquifer using tracer tomography. Since then, tracer tomography has been used to identify dense non-aqueous phase liquids in aquifers (Datta-Gupta, 2002; Yeh and Zhu, 2007; Zhu et al., 2009), to find different sediment layers in porous aquifers (Jiménez et al., 2016), and to locate fractures in hard rocks (Brauchler et al., 2013a). In the numerical study of Schwede et al., (2014), thermal tracer tomography was used for aquifer characterization to demonstrate its potential for tomography. Doro et al., (2015) provided a field design for thermal tracer tomography, and conducted a field campaign using this method. However, no further aquifer characterization was done with the collected dataset.

1.3 Aquifer models

In order to invert the tomographic data, the investigated aquifer has to be parametrized and described mathematically using a parameter vector θ. The two most important attributes of model parametrization are the model complexity and the level of detail. An optimal aquifer model should be detailed enough to represent every aquifer feature that could influence the experimental results, keeping the size of the parameter vector limited in order to avoid inversion instability. This means that porous and fractured aquifers require different parametrizations.

1.3.1 Continuum models

Tomographic investigation methods are principally used to map the continuous spatial distribution of physical properties, whether it is the seismic velocity distribution of the subsurface or the structure of the human body. Porous aquifers can be modelled by continuous parameter distributions as heterogeneous features such as sand lenses or different sediment layers usually show smooth boundaries. Continuous aquifer models are stored in a discretized form for the inversion.

Grid-based models

The most common discretization type is a grid. Each grid cell stores an average value of the hydraulic parameters inside. However, with standard grids, the real heterogeneous features are described along a regular pattern. Therefore, homogeneous zones of the aquifer are sampled with the same physical resolution as zones with strong heterogeneities.

Adapted grids overcome this sampling problem by increasing the local grid resolution at heterogeneous model parts (Vesnaver and Böhm, 2000). Triangular grids are especially suited for this task, thus they are widely used for forward modelling with complex geometries (Shewchuk, 1996). However, in inversion applications, the adapted grid must be defined over an unknown model geometry, which limits its applicability to such cases when an iteration-based inversion method is used or when the model geometry is known prior to the inversion.

For a well-posed tomographic inverse problem, the number of cells should be equal to the number of travel-times. This fact strongly limits the possible resolution of tomographic reconstruction, because the ill-posed inverse problems are unstable and non-unique (Aster et al., 2013; Menke, 1984; Yeh, 1986).

With the application of staggered grids, the nominal resolution of the final result can be higher without making the inversion unstable, because it comprises the means of spatially shifted coarse grids (Brauchler et al., 2007, 2013a; Hu et al., 2015; Jiménez et al., 2013; Vesnaver and Böhm, 2000). However, it requires running the inversion algorithm multiple times, increasing the total computational time.

Interpolated models

To reduce the number of parameters, continuous aquifer models may be stored in an interpolated form. In this case, the distribution of hydraulic properties is interpolated from so-called pilot points (de Marsily et al., 1984). The interpolation is based on field observations

of the geostatistical properties of the aquifer. Pilot points should be placed more frequently in highly heterogeneous aquifer areas, thus improving the model resolution locally. Using pilot points results in an optimized inversion with fewer unknown parameters; therefore, the method is widely used for aquifer characterization (Doherty, 2003; Illman, 2014; Jardani et al., 2013; Jiménez et al., 2013, 2016; Yoon and McKenna, 2012).

Continuum models for fractured media

The continuum model approach is also suitable to describe hard rock aquifers, where flow and advective transport are restricted to the fractures. These aquifers may be modelled as highly heterogeneous but continuous domains. Continuous models are able to delineate the main flow channels within aquifers, but due to their smoothing behavior, individual fractures are not likely to be identified with them (Day-Lewis et al., 2000; Hao et al., 2008; Illman and Neuman, 2003; Sahimi, 2011; Zha et al., 2015). Therefore, the application of the continuum approach is limited for fractured rocks with high fracture density. Continuous models can also provide decent results when flow channeling plays an important role (Sahimi, 2011). However, complex fracture patterns cannot be resolved using continuum models.

1.3.2 Discrete models

Discrete fracture networks (DFNs) are realistic representations of fractured aquifers. DFNs consist of interconnected permeable fractures embedded in a low-permeability rock matrix. DFNs are commonly used to generate stochastic fracture network realizations after field observations of the statistical properties of fractured rocks (such as fracture length distribution, fracture spacing, and fracture density).

In DFN models the hydraulic parameters are assigned to the individual fractures. Additionally, each fracture requires geometric parameters on its location and size. Hence, DFNs have a large number of parameters, which makes them difficult to use for calibration purposes. In addition, the number of fractures is usually unknown prior to the inversion, meaning that the number of parameters is undefined. Traditional inversion methods are incapable of solving these types of problems. Available automated calibration methods either keep the number of fractures fixed (Le Borgne et al., 2007; Dorn et al., 2013; Le Goc et al., 2010; Klepikova et al., 2014), activate-deactivate fractures (Hestir et al., 1998; Niven and Deutsch, 2012), or solve the inverse problems over the statistical parameters of the fracture network instead (Jang et al., 2008). Dorn et al., (2013) suggested that using variable dimension inversion would be an ideal choice for DFN characterization.

1.4 Inversion methods

The last element of aquifer characterization is solving the inverse problem, fitting the parameter vector of the aquifer model to the observed data. In geophysics, two main types of inversion methods are known: deterministic and stochastic (Francis, 2006). Deterministic inversion methods always give the same model parameter vector as a result when the same observation data are used as input. In contrast, stochastic inversion results in a set of parameter vectors. Although the individual parameter vectors are different for each inversion run, the probabilistic properties are the same.

1.4.1 Deterministic methods

For tomographic aquifer characterization, various deterministic inversion methods have been presented in the literature. A summary of these studies is shown in Figure 1-3 with respect to the evolution steps in the methodologies.

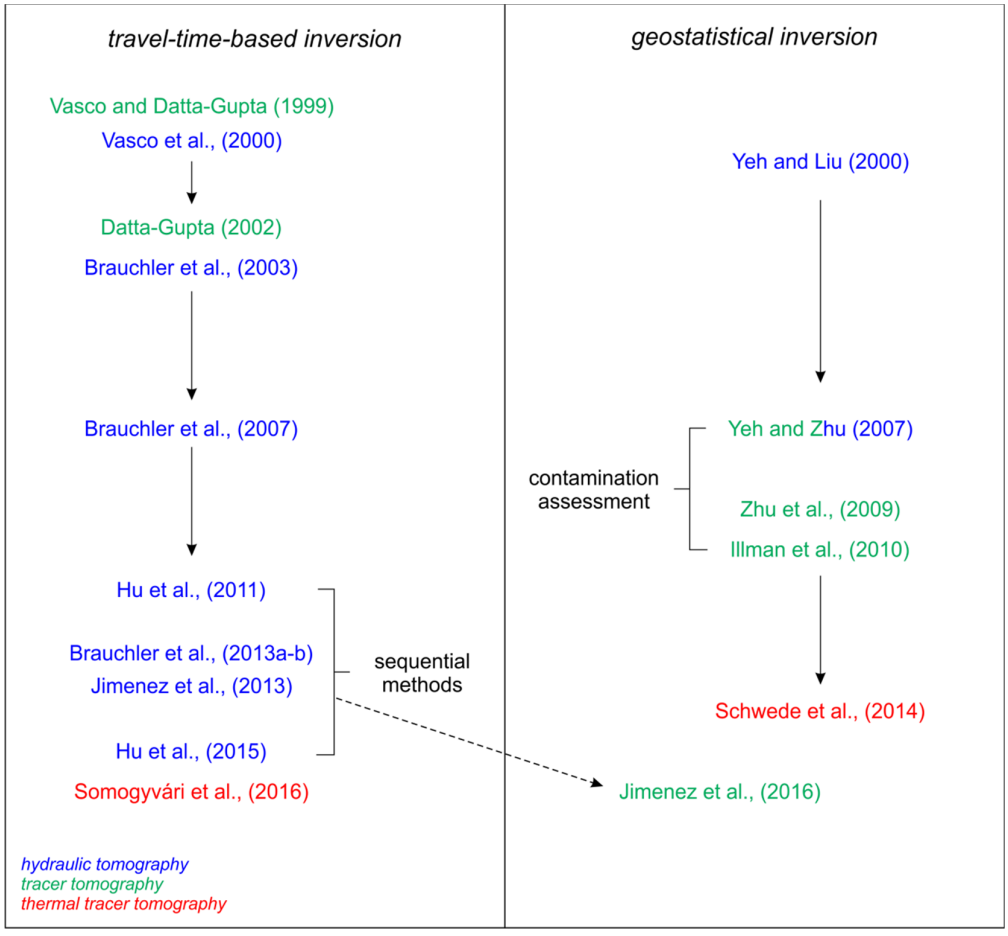

Figure 1-3. Evolution of deterministic inversion methods used for tracer tomography.

Travel-time-based inversion

Interpretation methods for tracer tomography could exploit the similarities to tomographic methods in other research fields. This requires not only a similar source-receiver setup, but also a similar mathematical formulation for the physical process of the tracer propagation. Vasco and Datta-Gupta (1999) proposed an asymptotic formalism to invert tracer tomography. According to their work, from the transport equation of a tracer the following expression can be derived for the tracer travel times:

$$t_t(x_r) = \int_{x_s}^{x_r} \frac{ds}{v_t(s)} \tag{1-4}$$

The travel time of a tracer (t_t) between the injection point (x_s) and the observation point (x_r) can be expressed as the line integral of the tracer velocities along the tracer trajectory (v_t). Assuming that the tracer propagation is advection-driven, the tracer velocity can be expressed as follows, from the Darcy equation:

$$t_t(x_r) = \int_{x_s}^{x_r} \frac{\phi(s)}{K(s)i(s)} ds \tag{1-5}$$

where ϕ is the porosity, K is the hydraulic conductivity and i is the hydraulic gradient. This type of line integral is known as the travel time equation or eikonal equation. Using a tomographic setup, the investigated domain is dissected by multiple transport pathways. Each tracer travel time contains information about the K along its pathway; thus a set of travel times contains information about the distribution of K in the domain.

The goal of tomographic inversion is to reconstruct the K distribution. First, the transport pathways are estimated by standard ray tracing techniques. These techniques use Fermat`s principle, i.e. the detected tracer is transported along the fastest possible pathway between the source and receiver. The transport trajectories calculated over velocity fields by ray tracing are then used in standard tomographic solvers as the forward model. For example, the SIRT (simultaneous iterative reconstruction technique) algorithm calibrates the velocities on a grid sequentially to fit the observed travel times with the ones simulated by ray tracing (Jackson and Tweeton, 1996).

The travel-time-based tomographic inversion concept has been used in several hydraulic tomography applications. Vasco et al., (2000) showed that the eikonal equation can be derived for hydraulic signals.

$$\sqrt{t_h(x_r)} = \frac{1}{\sqrt{6}} \int_{x_s}^{x_r} \frac{ds}{D(s)} \qquad (1\text{-}6)$$

The concept was further developed by Brauchler et al., (2003), using the travel times of Dirac and Heaviside hydraulic signals for hydraulic diffusivity calculation. As this equation contains diffusivity instead of hydraulic conductivity, further interpretation is required to obtain the *K* field.

Brauchler et al., (2007) included the attenuation of the hydraulic signals in the inversion as a sequential step to estimate the distribution of specific storage. *K* then can be calculated from diffusivity and specific storage. Other studies kept only the structural information from the travel time inversion and used an additional parameter calibration step on the identified structures (Hu et al., 2011; Jiménez et al., 2013). Hu et al., (2015) demonstrated that with travel-time-based inversion of pressure tomography it is possible to image the geometry and saturation of stored supercritical CO_2. Brauchler et al., (2013a) used the same method to interpret tracer tomography on a fractured lab sample.

Geostatistical inversion

Yeh and Liu (2000) presented a different inversion technique for hydraulic tomography, using an iterative geostatistical inversion, called the successive linear estimator (SLE). This sequential method first estimates a *K* field based on the available geostatistical data, which is then iteratively updated by a linear estimator based on the observations. This approach is capable of processing the large amount of data generated during tomographic experiments and to include additional measurements in the process, thus providing more reliable results.

The concept was further developed and applied for tracer tomography. For example, Yeh and Zhu (2007) combined partitioning tracer tomography with hydraulic tomography to investigate industrial contaminations. Their method involved the reconstruction of hydraulic heterogeneities and thus prior hydraulic information was essential to identify contaminated aquifer zones. Zhu et al., (2009) suggested a modification for the inversion procedure using temporal moments instead of discrete tracer concentration data to make it computationally more effective. They also showed that tomographic tracer data alone is enough to

characterize the hydraulic conductivity without involving additional hydraulic tests. Laboratory studies of Illman et al., (2010) showed that the abovementioned tomographic methods are capable of reconstructing the subsurface hydraulic properties in practice. A similar geostatistical inversion method was used by Schwede et al., (2014) to interpret synthetic thermal tracer tomography in 3-D.

The main drawbacks of the geostatistical inversion approach are the required high computational demand and the fact that the resulting hydraulic conductivity distribution is related to the statistical priors used. Geostatistical inversion yields very smooth hydraulic parameter fields, which is not ideal for characterizing highly heterogeneous porous media or fractured rocks.

1.4.2 Stochastic methods

Jiménez et al., (2016) presented a fundamentally different inversion method for tracer tomography. Their concept used pilot points to parametrize the aquifer, and applied a transdimensional stochastic inversion scheme to calibrate the model. Several studies utilized stochastic inversion methods to calibrate aquifer models described by pilot points (Illman, 2014; Jardani et al., 2013; Kowalsky et al., 2012; Yoon and McKenna, 2012). The main difference in the work of Jiménez et al., (2016) was the transdimensional inversion. While traditional inversion methods solve the inverse problems over a predefined set of parameters (Menke, 1984), transdimensional inversion varies the number of parameters during the solution process and solves the problem over an unknown number of parameters (Sambridge et al., 2012). Treating the number of parameters as unknown reduces constraints due to parametrization but also increases the complexity of the inverse problem.

The most popular transdimensional inversion method is the reversible jump Markov Chain Monte Carlo (rjMCMC) algorithm (Green, 1995). It has been widely used in different fields of geosciences, for example in geomorphology by (Fox et al., 2015), in seismic exploration (Dadi et al., 2015; Dettmer and Dosso, 2012; Malinverno and Leaney, 2005), in seismic tomography (Bodin and Sambridge, 2009) and in resolving porous flow (Mondal et al., 2010). The methodology is suitable for solving the inverse problem of imaging methods, where spatially variable model resolution is beneficial. For example, Bodin and Sambridge (2009) used Voronoi-cells to reproduce the seismic velocity field, while Jiménez et al., (2016) interpolated the hydraulic conductivity field from smart pilot points. The model parametrization in these studies is adapted to the distribution of the investigated physical

properties via the rjMCMC algorithm, providing a well-optimized and robust reconstruction of the parameter distribution.

Dorn et al., (2013) recommended using transdimensional inversion to calibrate discrete fracture models. Fracture networks are ideal subjects for this methodology, because the number of fractures in the model is unknown prior to the inversion, although they are a key part of the parametrization. Still, no rjMCMC method has been reported in the literature for fracture network calibration.

1.5 Objectives

The main goal of this PhD project is to develop a set of robust inversion methods suited to the interpretation of thermal tracer tomography experiments. Two different approaches are used: (i) deterministic, travel-time-based inversion in porous media; and (ii) stochastic, transdimensional inversion in fractured media.

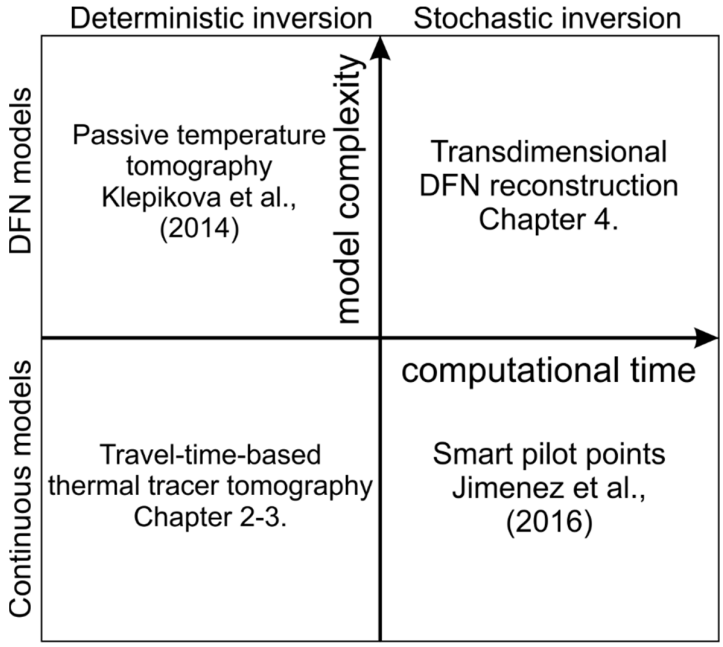

Figure 1-4. Aquifer characterization methods using temperature-based tomographic investigations with respect to the complexity of the aquifer model and the computational demands of the inversion method.

The context of this research is illustrated schematically in Figure 1-4, where the most common temperature related aquifer characterization methods are shown. In my view, the two main attributes of these methods are the complexity of the used aquifer model and the computational requirements of the inversion algorithm. The travel-time-based inversion

approach proposed for porous aquifers relies on continuous models, and a fast deterministic inversion scheme to calculate the hydraulic conductivity tomogram. For applications in hard rock aquifers, a stochastic inversion has been developed that calibrates discrete fracture models to the tomographic observations, allowing the reconstruction of the fracture network geometry.

In the following three chapters, the main findings of this PhD research project are presented. In Chapter 2, the travel-time-based thermal tracer tomography concept is introduced, as an analog of travel-time-based hydraulic tomography, to characterize porous aquifers. Using the early time diagnostics of continuous injection signals, the effects of diffusion- and buoyancy-driven flow are minimized. The concept is tested on a synthetic dataset with multiple different scenarios, 2-D and 3-D configurations, different injection temperatures and rates, and different geologic conditions.

The field validation of the concept is presented in Chapter 3, which is the first field application of thermal tracer tomography that resulted in a cross-well tomogram. A novel experimental design is presented, using cost-effective pulse injection signals. The results of the field experiment are validated by comparison with previous studies completed at the same site.

Chapter 4 focuses on fractured aquifers. A new inversion approach is presented to calibrate the geometry of discrete fracture models on tomographic data. By using the transdimensional rjMCMC algorithm, the inversion is capable of calibrating the geometry of a fracture network for an a priori unknown number of fractures. The inversion method is applied to the example of conservative tracer tomography, but it is suitable to interpret thermal tracer tomography after adjustments in the forward model. The method is validated using two synthetic examples, a hypothetical simple one-fracture aquifer and a fracture network mapped in the field.

2 Travel time based thermal tracer tomography

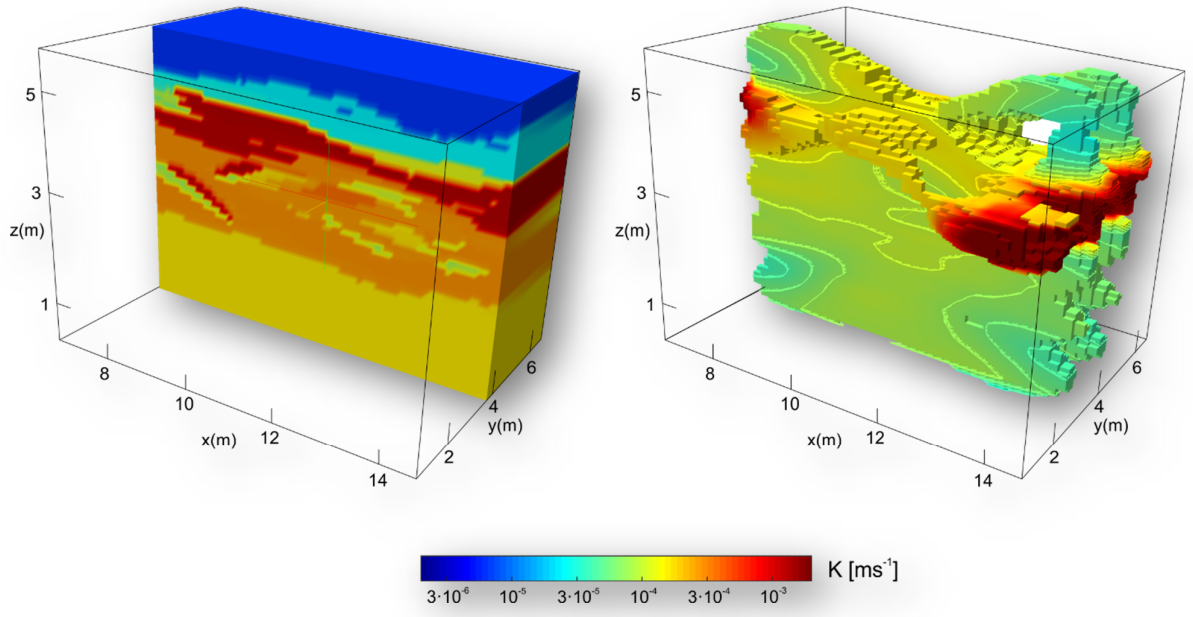

Published in Hydrology and Earth System Sciences

Somogyvári, Márk, Peter Bayer, and Ralf Brauchler. "Travel-time-based thermal tracer tomography." *Hydrology and Earth System Sciences* 20.5 (2016): 1885-1901.

Hydrol. Earth Syst. Sci., 20, 1885–1901, 2016
www.hydrol-earth-syst-sci.net/20/1885/2016/
doi:10.5194/hess-20-1885-2016

Abstract:

Active thermal tracer testing is a technique to get information about the flow and transport properties of an aquifer. In this paper we propose an innovative methodology, using active thermal tracers in a tomographical setup to reconstruct cross-well hydraulic conductivity profiles. This is facilitated by assuming that the propagation of the injected thermal tracer is mainly controlled by advection. To reduce the effects of density and viscosity changes and thermal diffusion, early time diagnostics are used and specific travel times of the tracer breakthrough curves are extracted. These travel times are inverted with an eikonal solver using the staggered grid method to reduce constraints from the pre-defined grid geometry and to improve the resolution. Finally, non-reliable pixels are removed from the derived hydraulic conductivity tomograms. The method is applied to successfully reconstruct cross-well profiles as well a 3-D block of a high resolution fluvio-aeolian aquifer analog dataset. Sensitivity analysis reveals a negligible role of the injection temperature, but more attention has to be drawn to other technical parameters such as the injection rate. This is investigated in more detail through model-based testing using diverse hydraulic and thermal conditions in order to delineate the feasible range of applications for the new tomographic approach.

2.1 Introduction

Tracers are commonly used to get an insight into the hydraulic properties of the subsurface on the aquifer scale and to identify dominant transport routes. Among the many tracers used for aquifer characterization, heat is frequently injected as a thermal tracer in boreholes or wells (Anderson, 2005; Hermans et al., 2015; Rau et al., 2014; Saar, 2011). From measured breakthrough curves (BTCs), aquifer heterogeneity and preferential flow paths are inferred (Bakker et al., 2015; Colombani et al., 2015; Klepikova et al., 2014; Leaf et al., 2012; Macfarlane et al., 2002; Vandenbohede et al., 2008; Wagner et al., 2014b; Wildemeersch et al., 2014).

Main attributes of ideal tracers are their good detectability, their lack of influence on the flow regime, conservativeness, and nontoxicity to the environment. Heat is an ideal choice because it is easily detectable by means of traditional temperature sensors, distributed temperature sensors (DTS) or with geophysical techniques (Hermans et al., 2014), and it can be monitored continuously in-situ. Typically, background variations are insignificant, and natural heating-cooling cycles have smaller frequencies than the investigated thermal signals. It is also ideal

because moderate changes in temperature do not harm the environment and thus commonly no regulative constraints are imposed. However, due to possible viscosity and buoyancy effects, and its relationship with hydraulic conductivity (K), variation in temperature may modify the flow regime. Ma and Zheng (2010) concluded from numerical simulations that no substantial density effects occur when heating groundwater up by 15˚C. This same critical value is given by Russo and Taddia (2010), based on the recommendations by Schincariol and Schwartz (1990) that buoyancy effects only appear at density differences higher than 0.8 kg m^{-3}. However, this calculation is only valid if the groundwater temperature is close to 0˚C. By setting a starting temperature of 10˚C (which is more realistic for a shallow aquifer in temperate climate), this critical density difference is already reached at a heating threshold of 8˚C. This value coincides with that by Ma et al., (2012), who refined their previous findings using field experiments and numerical sensitivity analysis. Essentially, despite several appealing properties, such a tight range for the temperature limits the viability of heat as a tracer. Viscosity and buoyancy effects may render a reliable interpretation of thermal tracer tests impossible. Alternatively, techniques have been developed that can handle broader ranges and are not prone to hydraulic effects of temperature variation. This is the focus of our study.

Our starting point is the fact that for detecting preferential flow paths full analysis of thermal transport behavior may not be necessary. If we focus on characteristic parameters such as travel times or moments of the BTCs, the signal-to-noise ratio may be acceptable for much broader temperature ranges. Travel times of traditional solute tracers are related to the hydraulic properties of aquifers, assuming that the main transport process is advection. This is the case given a sufficient ambient hydraulic or forced gradient during the experiment (Doro et al., 2015; Saar, 2011). One important difference of heat tracer transport over traditional tracers is that diffusion not only takes place in the pore fluid, but in the rock matrix as well. So while the tracer front of a solute tracer tends to be sharp, the thermal tracer front appears smoothed. This may make interpretation of BTCs more difficult.

Because thermal diffusion takes place, heat transport is affected not only by the hydraulic properties but by the thermal properties of the aquifer material as well. However, contrasts in thermal parameters are relatively small compared to contrasts in K, which typically spans orders of magnitude (Stauffer et al., 2013). Porosity can also be influential in heat transport, due to the high heat capacity contrast of water and rock components. Yet, natural variability

in porosity is commonly much smaller than that in K. Therefore variability observed in the transport of a thermal tracer is caused mainly by heterogeneity of K.

In previous studies on thermal tracer testing, diverse set-ups have been chosen that differ with respect to heating method, injection volumes, rates and temperatures, test duration, and well configurations (Wagner et al., 2014b). Mostly hot water is infiltrated in an injection well and BTCs are recorded in one or more downstream observation well (Ma et al., 2012; Macfarlane et al., 2002; Palmer et al., 1992; Read et al., 2013; Wagner et al., 2014b; Wildemeersch et al., 2014). Insight in aquifer heterogeneity is not well constrained by analysis of thermal signals introduced and measured over long screens. To obtain a better definition of the heterogeneity, observations in several wells or at different depth levels need to be compared. Ideally a tomographic setup is chosen, where multiple point injection (sources) and observation points (receivers) are used. By combined inversion of all signals, the spatial variations in K are reconstructed. So far, however, this concept is more established in geophysics, and for aquifer characterization in hydraulic tomography, which utilizes pressure signals from depth-dependent pumping tests or multi-level slug tests (Cardiff et al., 2009, 2012; Illman et al., 2010; Yeh and Zhu, 2007).

Klepikova et al., (2014) presented a passive thermal tracer tomography application for characterizing preferential flow paths in fractured media. Their method focused on modelling the fracture network with a sequential method which involves first identifying the location of fault zones on the temperature-depth profiles under ambient flow and pumping conditions. Next, an inversion of the temperature profiles is conducted to obtain borehole flow profiles, and the last step is to estimate the hydraulic properties from these flow profiles. This method provides cross-well connectivities. The work by Doro et al., (2015) is dedicated to the experimental design of cross-well forced gradient thermal tracer tomography. In their approach, a special multi-level injection system is necessary to induce the tracer into a horizontal layer. They also recommend limiting the temperature range to avoid buoyancy effects. Their proposed methodology to interpret the results is to use an inversion scheme developed by Schwede et al., (2014) for this specific experimental setup. This inversion method utilizes the temporal moment of measured BTCs and hydraulic head data together in a joint geostatistical inversion procedure (Illman et al., 2010; Yeh and Zhu, 2007; Zhu et al., 2009). This procedure is computationally demanding, and it assumes a multi-Gaussian distribution of hydraulic properties, which represents a strong restriction in comparison to the true conditions in the field.

In our work, we suggest a travel-time based inversion procedure, which does not require a priori structural or geostatistical assumptions and is computationally efficient. It is motivated by Vasco and Datta-Gupta (1999), who presented a numerical approach to reconstruct the hydraulic parameters of an aquifer using solute tracer injections in a tomographical setup. As a core element, the transport equation is transformed into an eikonal problem using an asymptotic approach for the tracer transport solution. Their approximation uses the similarity of tracer front propagation to seismic and electromagnetic waves, but with the restriction that the tracer front is abrupt. This approximation can be used for hydraulic signals as well (Vasco et al., 2000), and the travel time of the hydraulic signal can be related to the hydraulic diffusivity of the system. Brauchler et al., (2003) further developed a travel time based inversion for Dirac and Heaviside hydraulic sources, using the early time diagnostics of the signals. To improve spatial resolution, they applied staggered grids (Vesnaver and Böhm, 2000) during inversion. This inversion methodology was applied to several hydraulic laboratory and field experiments (Brauchler et al., 2007, 2011, 2013b; Hu et al., 2011; Jiménez et al., 2013). Brauchler et al., (2013a) also utilized travel-times in a tracer experiment on rock samples in the laboratory scale. Their work revealed that for those samples transport was dominated by the rock matrix, but hydraulic parameters were not estimated.

In this study, we present a new formulation for inversion of spatially distributed hydraulic conductivity using early tracer travel times. It follows the same principles as presented by Brauchler et al., (2003) for hydraulic tomography. Our objective is to obtain a versatile and efficient technique for thermal tracer tomography, which, by focusing on early times, minimizes the role of buoyancy and viscosity effects. In the following section, the new inversion procedure is introduced. It is then applied to a three-dimensional (3-D) high resolution aquifer analog of the Guarani aquifer in Brazil. We inspect the capability of the new approach to reconstruct 2-D and 3-D sections with heterogeneous K-distribution, and provide a sensitivity analysis of variable injection rates and temperature ranges. Finally, the findings of exhaustive testing with variable field conditions and technical design parameters are compiled to determine the application window of this new thermal tomography variant.

2.2 Tomographical inversion procedure

2.2.1 Travel time inversion

Under high Péclet number conditions, when it can be assumed that the thermal transport is dominated by advection, the propagation of an injected thermal plume can be used to gain information about the hydraulic properties of the investigated aquifer. Our goal is to calculate the hydraulic conductivity, *K*, of the aquifer by inverting the advective thermal tracer breakthrough times. (Vasco and Datta-Gupta, 1999) showed that the transport equation of a solute tracer can be formulated as an eikonal equation, which is utilized to calculate *K*. According to this work, a line integral can be written for tracer breakthrough times:

$$t_{st}(x_r) = \int_{x_s}^{x_r} \frac{ds}{v_{st}(s)} = \int_{x_s}^{x_r} \frac{\phi(s)}{K(s)i(s)} ds. \tag{2-1}$$

Here, $t_{st}(x_r)$ is the breakthrough time of the solute tracer at the receiver (x_r), x_s is the source location, v_{st} is the mean tracer velocity, ϕ is the aquifer porosity and i is the local hydraulic gradient. The line integral relates the tracer breakthrough time to the mean tracer velocity, and thus to the hydraulic conductivity along the transport trajectory. This equation can be used for a thermal tracer (tt) by including the thermal retardation factor, R:

$$t_{tt}(x_r) = \int_{x_s}^{x_r} \frac{ds}{v_{tt}(s)} = \int_{x_s}^{x_r} \frac{\phi(s)}{R\,K(s)i(s)} ds. \tag{2-2}$$

Thermal retardation depends on the porosity of the aquifer, ϕ; the heat capacity of aquifer matrix, C_m; and the heat capacity of water C_w:

$$R = \frac{C_m}{\phi\, C_w}. \tag{2-3}$$

Changes in these parameters are commonly small compared to changes in *K*, thus the thermal retardation can be approximated as a constant. For the same reason, ϕ and the hydraulic gradient, *i*, are also considered fixed. Values of ϕ and *C* can be approximated from prior data, while the hydraulic gradient between observation and injection is measured during the experiment. With these assumptions and the use of standard tomography algorithms, the *K* distribution can be reconstructed on a pre-defined grid.

In this study, a step-function injection temperature signal is used for the active thermal tracer test. In this case the traveling time of the thermal tracer is associated with the propagating thermal front. The tomographical concept requires multiple independent thermal tracer injections at different depths. Temperature BTCs are recorded at multiple observation points, for example at different levels in a downgradient observation well. As common practice for such setups, the number of sources and receivers is one of the important factors that defines the significance and resolution of the results.

2.2.2 Early time diagnostics

Compared to a conservative solute tracer, heat does not behave ideally. Diffusion is significant in aquifer matrix and pore fluid, while the viscosity and density of the groundwater are variable. Due to the highly diffusive behavior, the emerging thermal front cannot be considered as a sharp transition boundary. In order to obtain accurate results with the inversion, the complications from thermal diffusion need to be mitigated. Both diffusion and mechanical dispersion effects increase with travel time. Mitigation thus can be done by using an earlier characteristic time of the thermal front instead of the (peak of the first derivative) breakthrough time, thus using the fastest component of the heat transport - advection. The earlier characteristic time can then be corrected to the real breakthrough time using a conversion factor, as shown for hydraulic tomography by Brauchler et al., (2003) with a correction for the specific storage coefficient.

The propagation of a thermal front far from the source is described as a one-dimensional (1-D) advection-diffusion problem considering thermal retardation:

$$R\frac{\partial T}{\partial t} = D\ \frac{\partial^2 T}{\partial x^2} - u\frac{\partial T}{\partial x}, \tag{2-4}$$

where R is the thermal retardation factor, T is temperature, D is thermal diffusivity and u is groundwater velocity. The analytical solution to this problem is (Ogata and Banks, 1961):

$$T(x,t) = T_0\left(\frac{1}{2}erfc\left(\frac{Rx-ut}{2\sqrt{DRt}}\right)+\frac{1}{2}\exp\left(\frac{ux}{D}\right)erfc\left(\frac{Rx+ut}{2\sqrt{DRt}}\right)\right), \tag{2-5}$$

where T_0 is the initial temperature, and $erfc$ is the complementary error function. In this study, we use a step function injection signal as the thermal tracer and its breakthrough time is associated with the peak of the first derivative of the temperature (Vasco et al., 2000) and can be calculated analytically. During the breakthrough detection, instead of the temperature,

the first derivative, T', of the temperature is used as the observed signal and its breakthrough time (t_{peak}) is defined as:

$$T''(x, t_{peak}) = 0\,. \tag{2-6}$$

By substituting Eq. (2-5) into Eq. (2-6) the peak time can be expressed as:

$$t_{peak} = \frac{R\sqrt{9D^2 + u^2x^2} - 3DR}{u^2}\,. \tag{2-7}$$

Early time characteristic values can be described proportionally to the peak value:

$$T'^{(x,t)} = \alpha T'\big(x, t_{peak}\big), \tag{2-8}$$

which can be related to the relative peak time (τ_α) as:

$$\alpha = \frac{T'(x,t)}{T'(x,t_{peak})} = \frac{T'(x,\tau_\alpha t_{peak})}{T'(x,t_{peak})}. \tag{2-9}$$

By relating these two expressions, the time of proportional value can be used to calculate the timing of any value of the signal. Substituting the peak time solution into this expression yields:

$$\alpha = \frac{\exp\left(-\dfrac{(\tau_\alpha - 1)\big(u^2x^2 - 18D^2\tau_\alpha - \tau_\alpha u^2x^2 + 6D\tau_\alpha\sqrt{9D^2 + u^2x^2}\big)}{12D^2\tau_\alpha - 4D\tau_\alpha\sqrt{9D^2 + u^2x^2}}\right)}{\tau_\alpha{}^{\frac{3}{2}}} \tag{2-10}$$

where

$$\tau_\alpha = \frac{t}{t_{peak}} = \frac{1}{f_\alpha}. \tag{2-11}$$

f_α is the transformation factor that can be used to correct early time diagnostics back to real breakthrough time.

Although Eq. (2-10) has three additional parameters, velocity (u), distance (x) and dispersion coefficient (D), the function is not sensitive to these values because they are all at higher orders or multiplied with higher orders of velocity. So, by neglecting the terms with higher orders of velocity, they are cancelled out. After neglecting the second order terms of velocity, the expression can be simplified to

$$\alpha = \frac{\exp\left(\dfrac{6(\tau_\alpha - 1)}{4\tau_\alpha}\right)}{\tau_\alpha{}^{\frac{3}{2}}}\,. \tag{2-12}$$

This equation can be solved analytically for τ_α, although infinite numbers of transcendent solutions exist. To have an analytical solution for τ_α-values between 0 and 1 (times before the peak time), the -1st branch of the Lambert Omega function is applied. The final expression for the transformation factor reads:

$$f_\alpha = \frac{1}{\tau_\alpha} = -LambertW\left(-1, -\frac{\alpha^{\frac{2}{3}}}{e}\right). \quad (2\text{-}13)$$

Note that the presented solution is only valid if α and f_α are positive. The Lambert Omega function is the inverse function of $f(W) = We^W$ (Weisstein, 2002). Equation (2-13) corresponds to the transformation factor used in hydraulic tomography presented by Brauchler et al., (2003) and Hu et al., (2011). In order to apply the conversion, the temporal scale of the record must be adjusted to the time of the thermal front arrival. In practice, this time is when the first increase on the temperature derivative record can be observed.

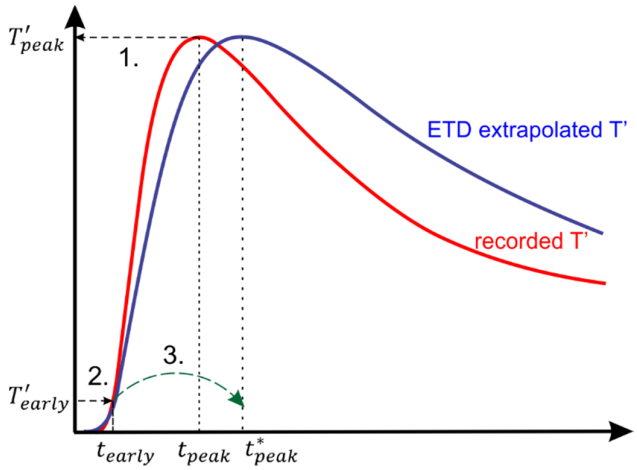

Figure 2-1. Three steps of applying early time diagnostics (ETD) on a thermal breakthrough curve (BTC). 1. Identify the peak T' value on the recorded BTC. 2. Find the early time value to the corresponding fraction of the signal. 3. Extrapolate the early time to the ideal peak time using the transformation factor, f_α.

The application of early time diagnostics is illustrated on Figure 2-1. We are mainly interested in advective transport. However, thermal diffusion may also be significant, smoothening and expanding recorded temperature BTCs, and thus affecting also its derivative. The identification of the peak time through the derivative T' is challenging due to the flatness of the curve at the maximum value of the peak. However, using the early time diagnostics (step 1), only the value of the peak must be known for Eq. (2-8). In step 2, the desired fraction of the peak value (α) and the associated time (τ_α t_{peak}) must be found on the

measured T' curve. Finally, in step 3, the time is corrected to a calculated peak time using the transformation factor according to Eq. (2-13). In this step, the temperature curve is extrapolated from the fraction time, and by this the effect of diffusion is taken into account. Note that the time zero of the correction is when the thermal front reaches the receiver. This time can practically be chosen when the earliest identifiable temperature change appears at a receiver. Step 3 allows the travel time to be related with the transport process, and to return a real and scaled *K* value instead of just information about the heterogeneity contrasts.

2.2.3 Staggered grids and null-space energy

To invert the tracer travel times the SIRT algorithm (simultaneous iterative reconstruction technique) is used to solve the eikonal problem, implemented in GeoTOM3D (Jackson and Tweeton, 1996). The algorithm calculates the transport trajectories between the sources and receivers and solves the line integral of Eq. (2-2) along the trajectories – in a curve based 1-D coordinate system. For solving the line integral, the solution domain is discretized to a grid. Initially a homogeneous velocity field is defined, and then the velocity values of the cells are updated iteratively to minimize the difference between the inverted and recorded travel times. The algorithm results in mean tracer velocities, and they are transformed into *K* using the relation of Eq. (2-2), where constant porosity and head gradient is used. In order to provide the uniqueness of the solution, an even-determined problem is needed and thus the number of grid cells should be kept close to the number of measurements (source-receiver combinations). The spatial distribution of the trajectories is never uniform over the domain, the result quality can differ in space, and the result can be non-unique (Aster et al., 2013; Menke, 1984).

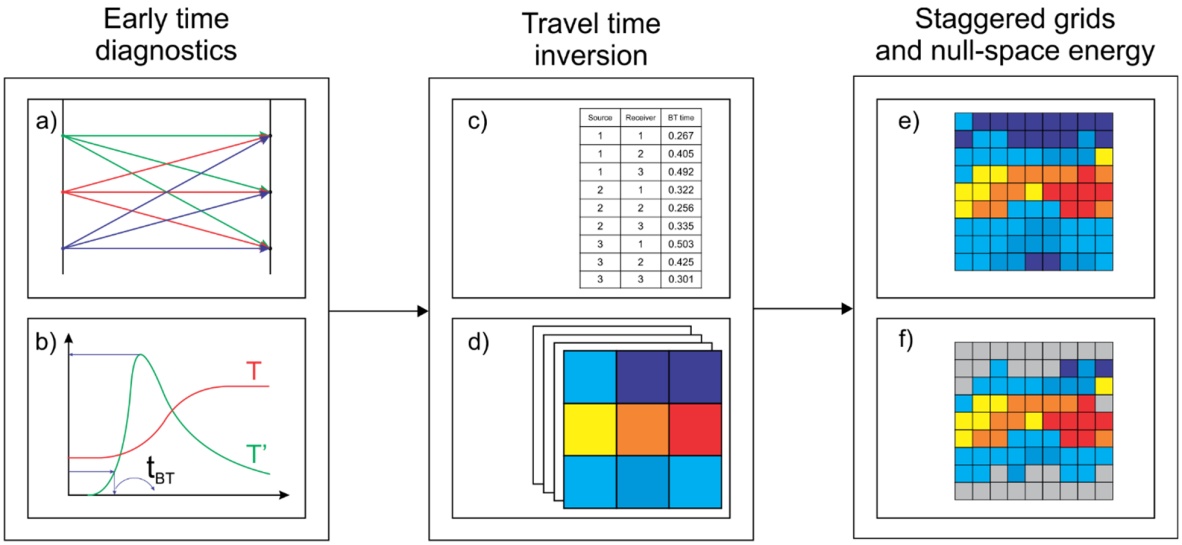

Figure 2-2. Major steps of inversion methodology: a) Conceptual setup of thermal tracer tomography, b) breakthrough time detection using the early arrival times, c) tomographical breakthrough time dataset, d) inverted tomograms applying the eikonal solver on different shifted grids, e) high-resolution tomogram after merging the staggered results together, and f) non-reliable pixels are masked after null-space energy calculation.

For discretization, instead of constructing a static regular grid, the staggered grid method (Vesnaver and Böhm, 2000) was used. Solving the problem on a regular grid would highly constrain the freedom of the solution to the geometry of the used grid and the source-receiver locations. By applying the staggered grid method this constrain can be overcome, with the benefit that the nominal spatial resolution is increased. Otherwise, for a good spatial resolution using one fine grid, a large number of sources and receivers would be required or regularization terms would have to be applied. Staggered grids were successfully employed for hydraulic tomography by Brauchler et al., (2003) and for solute tracer tomography by Brauchler et al., (2013a). In this staggered variant, the problem is solved on different vertically and horizontally shifted versions of a low-resolution regular grid. The inverted results are different for the shifted grids, which is exploited by arithmetically averaging these results to arrive at a final tomogram. The inversion will be stable because of the coarse grids, while the resolution of the averaged tomogram will be as small as the displacements. Although this means that the travel time inversion step will be performed multiple times for one tomogram, it is still computationally affordable due to the marginal computation demand of a single coarse grid resolution.

To characterize the reliability of the results, the null-space energy map is computed. This method has been applied for hydraulic tomography in several studies (Brauchler et al., 2013a,

2013b; Jiménez et al., 2013) and uses the distribution of the inverted transport paths over the inversion grid. The null space energy map is calculated from the singular value decomposition (SVD) of the tomographic matrix, which contains the length of each inverted transport path in each grid cell. Values of the null space energy map are between 0 and 1, thus higher values mean higher uncertainties. Based on the null-space energy map, non-reliable pixels can be deleted from the tomogram. The resulting full inversion procedure, starting with the tracer data and ending with the reliable part of the final *K*-tomogram is depicted in Figure 2-2.

2.3 Application case

2.3.1 Aquifer analog model

The presented methodology is developed and tested on the Descalvado aquifer analog (Höyng et al., 2014) that is implemented in a finite element heat transport model (Figure 2-3). This analog represents a 3-D high-resolution dataset obtained from mapping an outcrop of unconsolidated fluvio-aeolian sediments in Brazil. These sediments host parts of the Guarani aquifer system, one of the world's largest groundwater reservoirs. The analog is based on five vertical outcrop sections that are recorded during ongoing excavation and interpolated by multi-point geostatistics following the procedure by Comunian et al., (2011). The spatial extent of the analog is 28 m × 7 m × 5.8 m (x, y, z). Hydraulic conductivity, K, and porosity, ϕ, data was documented on sub-decimeter scale, in three parallel and two perpendicular profiles during excavation. Höyng et al., (2014) distinguish nine different hydrofacies (H1-9), which form the primary building blocks and which determine the structural heterogeneity of the characterized volume. In order to ease the interpretation of results, the focus is on major architectural elements which are the four zones that form the characteristic layers of the formation (Table 2-1). These can be easily distinguished visually by the dominant color in the selected color scale in Figure 2-3: the blue top low conductive zone, the red central conductive zone, the orange lower-central zone and the yellow bottom zone. In order to use this analog for thermal transport simulations, the original dataset (Höyng et al., 2014) is extended with estimated thermal properties (heat capacity, C, thermal conductivity, λ) assigned to the different hydrofacies units (“thermofacies”). These properties were calculated based on porosity and available lithological information (Bayer et al., 2015).

Table 2-1. Hydraulic conductivity, K, porosity, ϕ, thermal conductivity, λ, and bulk heat capacity, C, for the nine facies that build up the Descalvado analog. The four zones are introduced for discussion of results and listed here with the major facies components.

Zones	facies number (original code)	K [m s^{-1}][a]	ϕ[a]	λ [$Wm^{-1}s^{-1}$][b]	C [MJ $m^{-3}K^{-1}$][b]
Top low-conductivity	H1 (St,f)	$6.23 \cdot 10^{-6}$	0.24	3.19	2.49
	H2 (St,m2)	$2.49 \cdot 10^{-5}$	0.29	2.85	2.60
	H3 (St,m1)	$5.97 \cdot 10^{-5}$	0.29	2.85	2.60
Central conductive	H4 (Sh/Sp,m1)	$1.38 \cdot 10^{-3}$	0.33	2.61	2.69
Lower-central	H5 (SGt,c)	$2.96 \cdot 10^{-4}$	0.32	2.66	2.67
	H6 (SGt,m)	$9.44 \cdot 10^{-5}$	0.32	2.66	2.67
	H7 (Sh/Sp,m2)	$7.77 \cdot 10^{-5}$	0.29	2.61	2.69
Bottom	H8 (Sp,f)	$1.63 \cdot 10^{-4}$	0.25	3.12	2.51
	(clay)	$7.84 \cdot 10^{-8}$	0.29	1.90	3.00

[a] Höyng et al (2014), [b] Bayer et al. (2015)

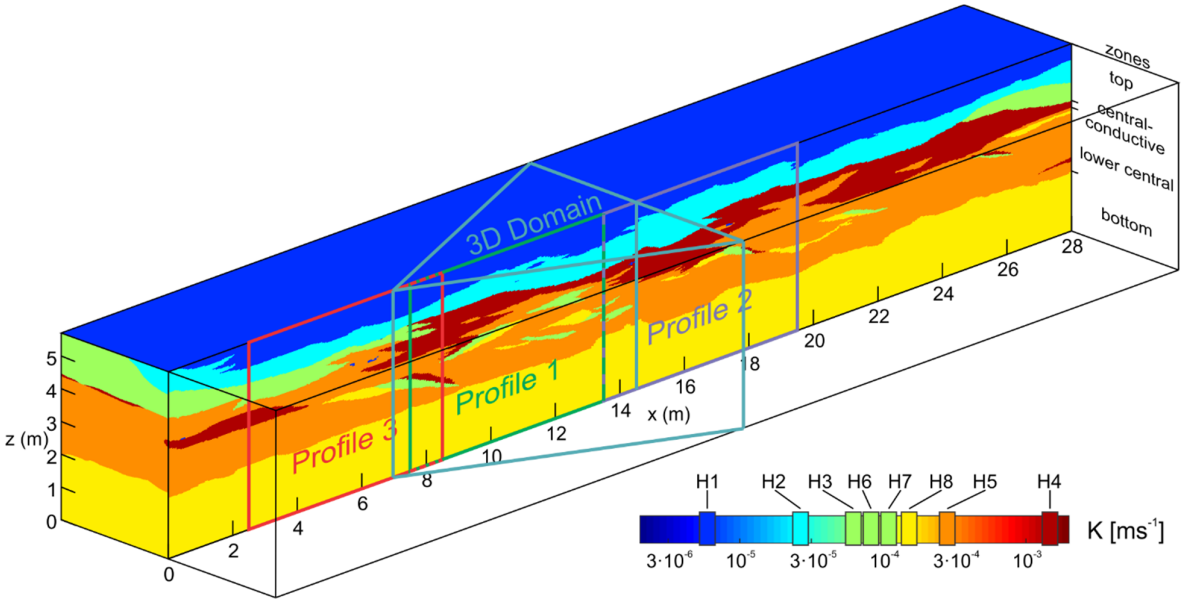

Figure 2-3. Vertical cross section through the center of the 3-D Descalvado analog dataset showing the distribution of hydraulic conductivity (K). H1-8 represent the hydrofacies units (ignoring clay intraclasts). The location of the three 2-D and one 3-D profile is marked with different colors.

The Descalvado aquifer is built up mainly by highly conductive sand and gravel with a layered structure. The average hydraulic conductivity value is approximately $K = 10^{-4}$ ms^{-1} and the largest difference between two adjacent hydrofacies is three orders of magnitude. Locally, low-K clay intraclasts exist that even induce higher variations. But, due to sizes of only a few centimeters and a marginal volumetric share, they are negligible for flow and thermal transport simulation. Thermal heterogeneity among the different facies units is controlled by differences in porosity, because the mineral composition does not substantially vary. When clay intraclasts are ignored, thermal conductivity spans from $\lambda = 2.6$ to 3.2 Wm^{-1}s^{-1}, and the volumetric heat capacity ranges between $C = 2.4$ and 2.6 MJ m^{-3}K^{-1}. The global thermal isotropic micro-dispersivity in the forward model is set to about the average grain size, $\beta = 0.1$ mm. In the inversion, the mean values were used (β is not used in the inversion because dispersion was neglected).

Flow and transport is simulated as coupled processes using the software FEFLOW (Diersch, 2014), and the SAMG algebraic multigrid solver (Thum and Stüben, 2012). The analog is embedded into a larger domain with extrapolated homogeneous layers, to minimize lateral boundary effects. The model mesh is generated with the Triangle algorithm (Shewchuk, 1996) and progressively refined towards the analog. Close to wells, the elements are refined to mm scale. The total extent of the model is 118 m × 117 m × 15.7 m consisting in a total of 1’664’626 triangle prism elements. In the center of the model, the resolution of the finite element mesh is similar to or finer than the resolution of the original aquifer analog dataset.

The aquifer is assumed to be confined. In order to simulate initial steady-state conditions with regional groundwater flow in the direction of the long axis, x, constant head boundary conditions are imposed at the perpendicular sides of the model and no-flow conditions at the other model faces. The constant head values are specified to impose an average hydraulic gradient according to Table 2-2, but for the inversion, the measured cross-well head difference was used. The initial temperature of the model is set to 10 ˚C. This value is also used as a boundary condition at the sides of the model, which yields isothermal initial conditions.

2.3.2 Experimental setup

We present reconstructions of K fields of 2-D and 3-D analog sections. These sections are called tomograms. 2-D profiles represent vertical cross-sections between an injection (source) and an observation (receiver) well, while data of three observation wells is utilized for 3-D

reconstruction. We specify a base case, which serves as our principal study case, and additionally inspect the performance of the methodology by varying the experimental design and profile. Note that independent of the dimensions of the reconstructed sections, the full 3-D analog model was always used to simulate the thermal tracer propagation and resulting travel times, considering buoyancy and viscosity effects.

Focus is set first on 2-D reconstruction. Three profiles in the central plane of the aquifer are selected (Figure 2-3). This central plane constitutes a mapped outcrop section with relatively high facies variability. It contains heterogeneous structures of different sizes and contrasts, and it is chosen for being sufficiently far away from the analog boundaries. The location of profile 1 is depicted in Figure 2-3. Figure 2-4a shows the relative locations of an upstream injection well and downstream observation well used for all three 2-D profiles. The distance between the wells is 5 m for an investigated area of 5 m x 6 m.

To examine further the role of aquifer heterogeneity, two additional profiles from the central plane of the analog are investigated. In both cases, the source-receiver geometries are kept the same (Figure 2-4a). Profile 2 shows a similar layered structure as profile 1, but with less small-scale heterogeneities. The central conductive zone is thicker, providing better connection between the two wells. In profile 3, the central conductive zone is discontinuous, creating a different hydrogeological situation, with weaker connection between the two wells.

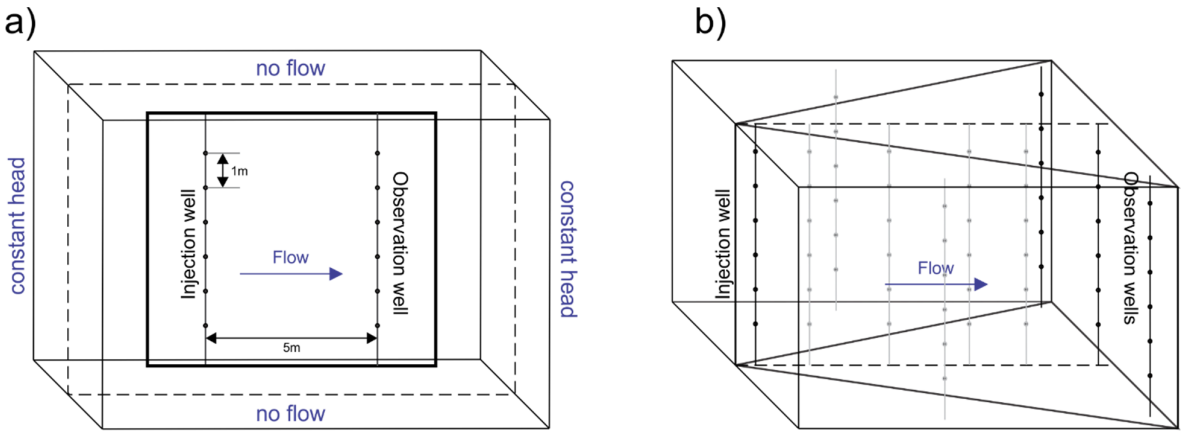

Figure 2-4. a) Simulated experimental configuration and numerical model boundary conditions. The tomographical setup consists of six sources in the injection well and six receivers in the observation well. b) Setup of the 3-D experiment with one injection and 3 observation wells. Additional wells used for validation are marked with grey color.

In the simulated setup, 6 sources and 6 receivers are employed (Figure 2-4a), resulting in a set of 36 source-receiver combinations. The sources are defined as point injections with constant injection rates during the entire simulation time. The used injection temperature

signal delineates a Heaviside step function, where the instantaneous change in temperature is arbitrarily set at 0.1 days after the start of simulation, which marks the beginning of the experiment. In order to record BTCs in all observation points even at very small injection rates and temperatures, extremely long simulation times are used (50 days). However, most of the breakthroughs occur during the first five days of the simulation.

The crucial technical design parameters for the experiments are the injection rate, Q, and the injection temperature (or temperature difference, ΔT, in comparison to ambient aquifer conditions). The base values of these two parameters are selected after preliminary field testing (Schweingruber et al., 2015) as $Q = 1$ ls^{-1}, and $\Delta T = 20$ ˚C. These parameter values and hydraulic model settings are varied in the ranges listed in Table 2-2 in the sensitivity analysis presented in Section 4.3.

Table 2-2. Parameterization of experimental setups, with base values and minimum-maximum ranges.

Parameter	Base case	Minimum	Maximum
Injection rate, Q [ls^{-1}]	1	10^{-3}	10
Injection temperature difference, ΔT [˚C]	20	5	80
Regional hydraulic gradient, i	0.01	10^{-3}	0.1
K range multiplier	1	0.01	100

In practice, the source of the injected water can be the investigated aquifer, but note that in this case heating has to be well controlled to keep the injection temperature constant. During a field experiment, the recorded data is always distorted by noise. With the commonly used temperature sensors, this noise is considered very small (Wagner et al., 2014b), but still the sensitivity of the temperature sensors is limited. To take this into account when simulating the receiver points, those where the temperature changes are smaller than 0.1˚C are ignored for the inversion. In addition, source-receiver combinations with geometric angles larger than 40˚ were not used, following the suggestion of Hu et al., (2011) for hydraulic tomography in layered aquifers. Thus 34 from 36 source-receiver combinations were used in the inversion.

For the 3-D reconstruction, an exemplary case is defined with 1 injection and 3 observation wells forming a triangular prism (Figure 2-4b) located close to profile 1. The base face is an isosceles triangle, and the observation wells are located along the baseline. The axis of this triangle is at the line where the 2-D profiles are located. The distance between the injection well and the central observation well is 6.5 m and the length of the triangle base is 3 m. The

configuration of the individual wells is the same, resulting 18 observation points, and 108 source-receiver combinations in total. The experiment was simulated using the base values from Table 2-2, employing the same Heaviside injection signals as in the 2-D cases.

2.4 Results and discussion

The following, results are structured into four major parts. The first part is the inspection of the inverted tomograms for the three 2-D and one 3-D analog profiles. The second part is the validation of the method using the result of the 3-D reconstruction. The third part is a sensitivity analysis of the inversion procedure with respect to experimental settings such as injection rate and temperature. The fourth part reveals the application window of travel-time based thermal tomography through rigorous testing with different sections, changing hydraulic conductivity contrasts and varying experimental parameters.

2.4.1 Reconstruction of hydraulic conductivity profiles

The left column of Figure 2-5 depicts the analog profiles, and these are contrasted with the inverted ones on the right. For better comparability, the original analogs are up-scaled (using the arithmetic mean of the values within a cell) to the same grid as used for the results with 0.125 m × 0.125 m cell size. Figure 2-5a represents the K distribution of the aquifer analog at profile 1. It is characterized by an overall layered structure, and it shows highest variability with small scale facies patches in the central part between z = 2 m and z = 4.5 m. Of major interest is the red central conductive zone (hydrofacies H4) at around z = 4 m with non-uniform thickness. In the field, it can cause flow focusing and promote preferential flow. This zone is even more pronounced in profile 2 (Figure 2-5c), but not continuous in profile 3, where only laterally high-conductive wedges can be found. In all profiles, the underlying lower central zone is dominated by the orange facies H5. With the embedded small-scale layered and cross-bedded elements, this zone will give insight in the competence of the inversion procedure to resolve local, decimeter-scale structures.

BTCs from 34 source-receiver combinations were used in one tomographic experiment. During staggering, the tomographic inversion is performed on 16 different spatially shifted coarse grids. The uniform cell size of these low resolution grids is 0.5 m × 0.5 m. In total, 30 iterations are done per inversion, and the inverted velocities are restricted within a range of physically possible tracer velocities. Note that the inversion algorithm allows to provide constrains in velocity and if they are not set appropriately, it can produce outlier pixels close

to the sources and receivers, where the flow is focused. Velocity limits (i.e. expected high and low values for K and i) can be calculated using prior information, and the method is not sensitive to small changes in their values. The 16 coarse tomograms are merged together into a fine staggered grid, with a resolution of 0.125 m x 0.125 m. The total computational time for reconstructing one profile was around 10 minutes on an office PC (Intel® Core™ i7-4770 CPU 3.40 GHz).

After calculation of null-space energy maps, a threshold of 85 % is found suitable to constrain the K-tomograms. In other words, only with null space energy of less than 85 % (or vice versa, with a reliability of at least 15 %) pixels are shown in the final reconstructed profile. As illustrated in Figure 2-5b, d, and f, this yields fringed edges in the K-tomograms, and some grayed gaps in the interior. Since the null space denotes local coverage of transport trajectories, there are some regions which are unsatisfactorily accessed. As expected, these are mainly close to the boundaries of the inspected profile and not in the reach of the source-receiver couples. By changing the arbitrary null space energy threshold, masking of areas of low reliability may be accentuated or mitigated. The most suitable value of the threshold, however, is based on expert knowledge and is set depending on the requirements of the specific case. Experience shows that modifying this value (by 5-10 %) has a minor influence on the visualized structures of major interest, because the null-space energy of the highly conductive zones tends be very small.

The reconstructed profiles in the right column of Figure 2-5 shed a first light on the capabilities of thermal tomography. First, we observe that for all profiles, the upper zone (in blue) cannot be reconstructed by the inversion. Typically a considerable fraction of it is masked in gray due to the limited contribution to heat transport, which is not surprising due to the low hydraulic conductivity of this zone. In contrast, the tomographic approach identifies the location of the highly-conductive upper central zone (in red) rather well. This zone delineates the fastest travel route between the wells for the heat tracer. Between the upper (blue) and central (red) zones is the strongest contrast in the profiles. This strong contrast shadows the top of the tomograms, because the transport is short-circuited through the high-K zone, resulting that it appears upshifted on the tomogram. When the contrast is smaller, such as in profile 3, this shadow effect is weaker, and it is possible to gain better insight into the low conductivity zone (Figure 2-5e-f).

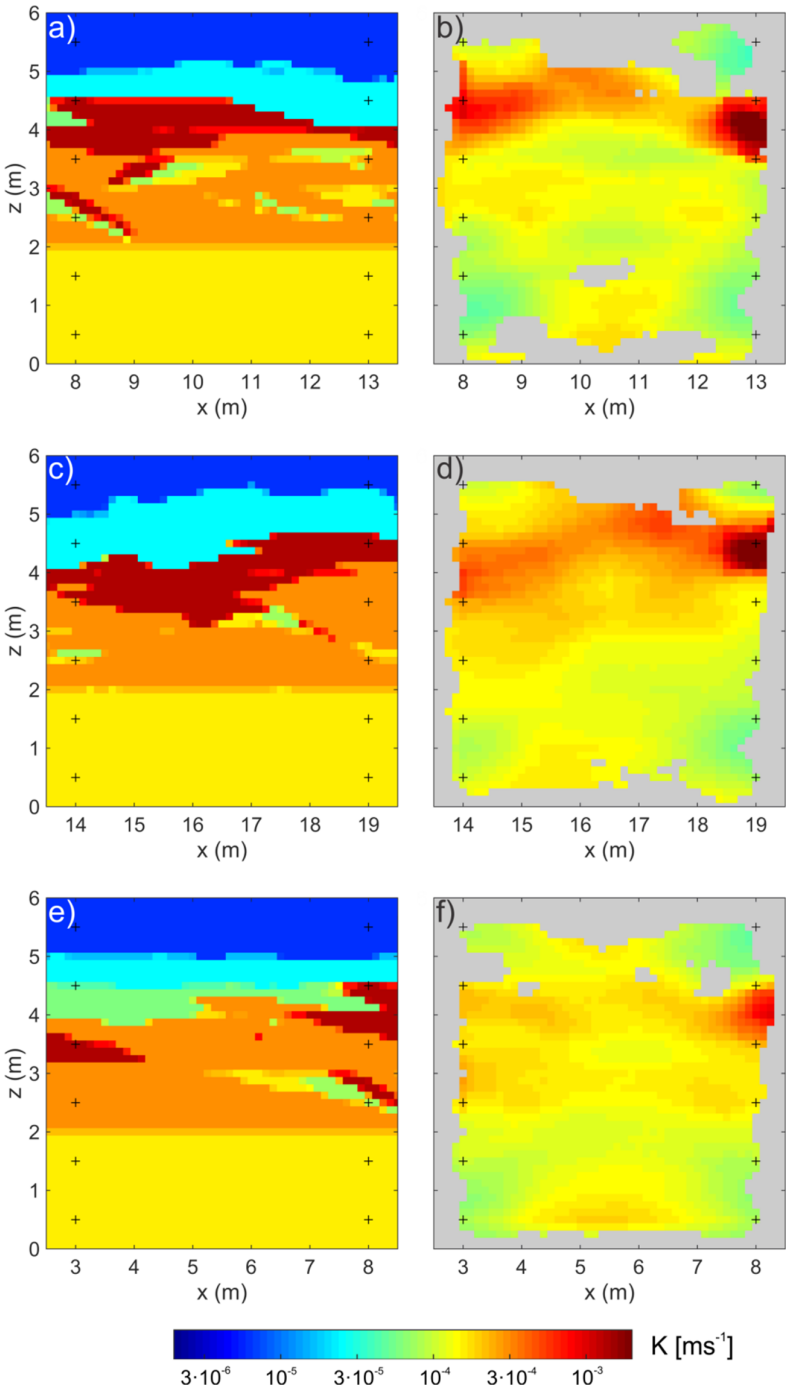

Figure 2-5. Hydraulic conductivity profiles (see Figure 2-3): a) profile 1 – aquifer analog; b) profile 1 – reconstructed tomogram; c) profile 2 – aquifer analog; d) profile 2 – reconstructed tomogram; e) profile 3 – aquifer analog; and f) profile 3 – reconstructed tomogram.

A striking feature is that the tomographic approach resolves the continuity of the highly-conductive upper central zone in profiles 1 and 2, and it detects the discontinuity in profile 3. Furthermore, the inverted value of hydraulic conductivity of this zone (K = 8×10^{-4} ms^{-1}) is comparable to the original model (K = 1.38×10^{-3} ms^{-1}). For the lower central zone, we obtain

a similarly good match with an inverted value of 1.6×10^{-4} ms^{-1} in comparison to the original value of 2.96×10^{-4} ms^{-1} for the dominant hydrofacies H5 (Table 1). This is remarkable, having in mind that related travel time-based techniques of hydraulic tomography have shown to be suited for structural reconstruction, but to a lesser extent for hydraulic parameter estimation (similar match values are found in Brauchler et al., 2007; Cardiff et al., 2013; Jiménez et al., 2013). In many of those studies, parameter values were obtained by ex-poste calibration with the full forward model (Hu et al., 2015, 2011; Jiménez et al., 2013).

The promising findings as depicted in Figure 2-5 support the applicability of travel-time-based tracer inversion for thermal tomography, even though thermal diffusion tends to blur advective travel times, which hinders a reliable inversion. However, by taking early arrival times of the recorded BTCs, this effect is minimized. Likewise, when preferential pathways exist, these will be detected by the first thermal breakthrough, which is least influenced by diffusion. As a result, travel-time based thermal tomography appears especially suited for locating and characterizing high-conductivity zones.

With the 36 source-receiver combinations, exact profile reconstruction is not possible, since the tomograms appear to be smoothed. Fine-scale differences in the form of the high-conductivity zone are not reproduced in the tomograms. This is the same for the small facies mosaics that originally occur in the mainly orange lower central zone. This zone seems mixed with the lower yellow zone, and the hydraulic conductivities of both zones are slightly underestimated. Despite the minor hydraulic contrast between both layers, however, the tomograms indicate locally a facies transition (especially in Figure 2-5f). This is not identified in the tomogram of profile 1 (Figure 2-5b). Here most small-scale structures exist in the lower central part above. These cannot be resolved, but they detract from the transport routes of the thermal tracer and thus induce noise in the reconstructions of the lower central and bottom layer.

Figure 2-6 shows the reconstruction of the selected 3-D section. The result is presented the same way as the 2-D profiles, using an upscaled version of the original analog for comparison. 3-D staggering is employed resulting in 64 coarse grids in total. This requires 64 individual inversions and thus a computational time that is drastically longer than in the 2-D cases. With 20 iterations per inversion, the total computational time on the same PC (Intel® Core™ i7-4770 CPU 3.40 GHz) was around 1 hour for 3-D inversion. The spatial resolution of the coarse grid is 0.5 m × 0.5 m × 0.5 m and of the staggered grid thus is 0.125 m × 0.125 m × 0.125 m.

To assess the reliability of the inverted result, the null-space energy map is calculated. For the 3-D application a limit of 95% of reliability is used to accept reconstructed voxels. Lower values would substantially reduce the reconstructed volume, since non-reliable voxels are not presented. Generally, the reliability and thus overall result quality of the 3-D analysis is worse than for the 2-D cases. This is due to the fact that the inverted transport paths cover less of the domain of interest.

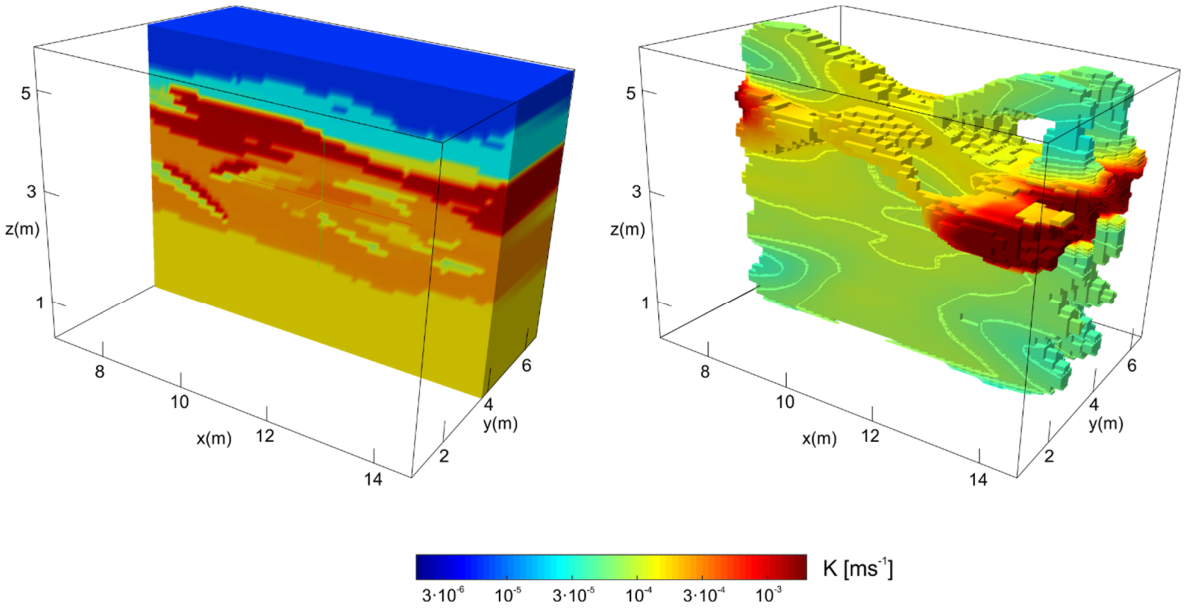

Figure 2-6. 3-D distribution of hydraulic conductivity (*K*): a) investigated subdomain of the upscaled aquifer analog b) reconstructed tomogram with additional contour lines and unsliced high-*K* zone.

Figure 2-6a depicts the upscaled analog model, sliced to half at the central plane where the injection well is located. The same way of presentation is used for the reconstruction in Figure 2-6b. To highlight the differences to the 2-D results, the inverted high-*K* zone is presented for the whole domain without slicing it to half. The central slice of the 3-D reconstruction is similar to profile 1, because the injection well located at the same location (Figure 2-5a) and the observation wells located only 1.5 m further away. However, by blanking unreliable voxels in the 3-D visualization it is difficult to compare the 2-D and 3-D reconstruction in Figures 2-5b and 6b. At first sight, the reconstructed features of the 3-D and the 2-D inversion are similar. A pixel-to pixel comparison using the central plane of the 3-D reconstruction shows that the difference to the reconstructed values of profile 1 is less than 30 %. This demonstrates that especially for systems with mainly horizontal structures such as the sedimentary aquifer here, results in 2-D are only slightly improved in a 3-D inversion. Comparing the full profile, the inverted *K* values are lower than at the 2-D cases, but still in

the same magnitudes as the original values of the aquifer analog (central conductive zone: 3×10^{-3} ms^{-1} inverted to 1.4×10^{-3} ms^{-1} original, middle zone: 1×10^{-4} ms^{-1} inverted to 3×10^{-4} ms^{-1} original).

In Figure 2-6b, the central conductive zone of the aquifer is localized mainly at the lateral boundaries close to the wells. Centrally, *K* values are underestimated and smooth channels appear between injection and observation wells, delineating the suspected main transport paths of the tracer. Similar as in the 2-D reconstructions, the central part of these channels is vertically upshifted. The top low-*K* zone is not reconstructed, but fragments of it appear in the results, marking the location of the contrast boundary on the bottom of this zone. The contrast between the two lower zones can be identified laterally but not centrally – same as in the 2-D profile. Although the 2-D nor the 3-D inversion were capable of reconstructing the top low-*K* zone, the distribution of the reconstructed transport trajectories can be used to identify these locations. Even if revealing more information about these zones is beyond the scope of this work, it would be an interesting aspect to examine in the future.

2.4.2 Validation

For validation, the reconstructed 3-D *K* field is implemented in a numerical model with the same settings as that used for the forward simulations with the original analog data. Here, homogeneous thermal properties are assumed. In total 9 observation wells with 6 observation points in each are used to validate the inverted result (Figure 2-4b). A full tomographic experiment is simulated with 6 independent warm water injections using the same configuration as the original simulated experiment. The recorded BTCs are compared with simulations with the aquifer analog dataset. The differences in the breakthrough times are used for the validation.

Considering the good reconstruction of the high-*K* zone, which is most relevant for the thermal transport, we can expect that at most of the observation points the difference would be small. This is exactly what Figure 2-7 shows, where the distribution of the differences is presented as histogram. Most of the values are close to zero showing a good validation of the result. There are two groups of outliers marked with yellow color. The negative outliers are associated with the observations in the top low-*K* zone where the inversion was not sufficient. Here the predicted heat transport is faster than in the aquifer analog. The second outlier group is related to the underestimated *K* of the lower central zone (Figure 2-3). The difference in the

breakthrough times becomes most significant at observation points that are furthest from the injection well.

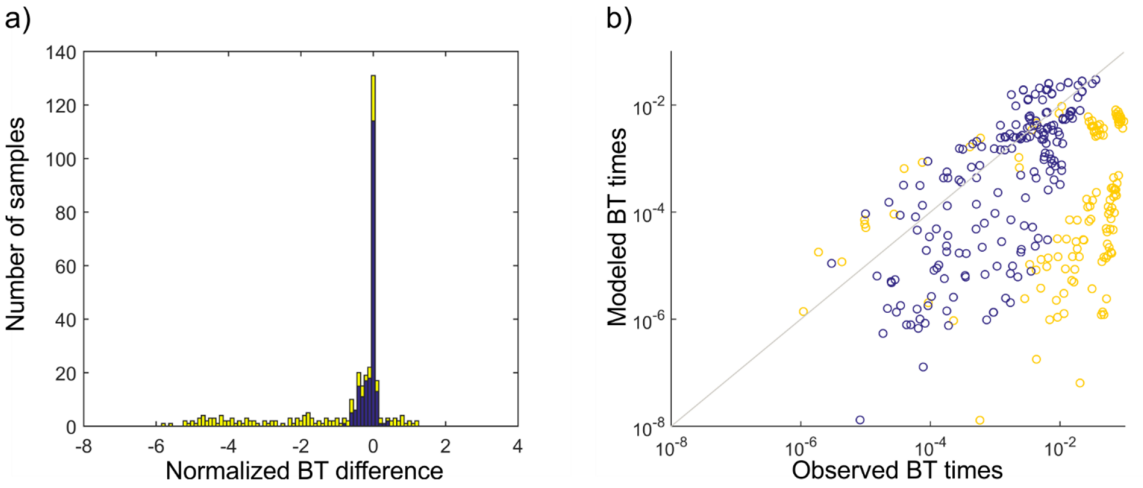

Figure 2-7. a) Histogram plot of absolute differences of breakthrough times between the inverted and the original model (192 samples normalized to the mean of the breakthrough times). Yellow color marks the known outliers, such as observation points in the top low-*K* zone and the far end of the domain. b) Scatter plot of observed and simulated breakthrough times.

2.4.3 Role of injection rate and temperature

The experimental setup may be crucial for the quality of the inversion results. For example, it is well known from related tomographic inversion studies that the feasible resolution depends on arrangement and the numbers of sources and receivers (Cardiff et al., 2013; Paradis et al., 2015). Here we focus on two technical design parameters, which are particularly crucial for thermal tomography when using heated water: the injection temperature and the injection rate. In the following sensitivity analysis, we question whether these need to be carefully tuned or not. Profile 1 is chosen for investigation depicted again in Figure 2-8a and 2-9a. Note that for forward simulation of travel times, always the full 3-D analog model is used.

We first inspect the role of the temperature of the injected water. In all of our models, the ambient groundwater temperature is considered uniform and 10 ˚C. Viscosity and density effects increase with the temperature difference, ΔT, in comparison to the ambient groundwater. These effects may distort the results of inversion, and thus a maximal difference of ΔT = 8-15 °C has been suggested for thermal tracer testing (Doro et al., 2015; Ma and Zheng, 2010; Russo, 2010). This severely constrains the applicability of heat as an active tracer, because it complicates interpretation of BTCs influenced by buoyancy forces. For our tomography, we examine a ΔT from 5˚C to 80˚C to cover the full range of technical possibilities. The injection rate is kept at Q = 1 ls^{-1}.

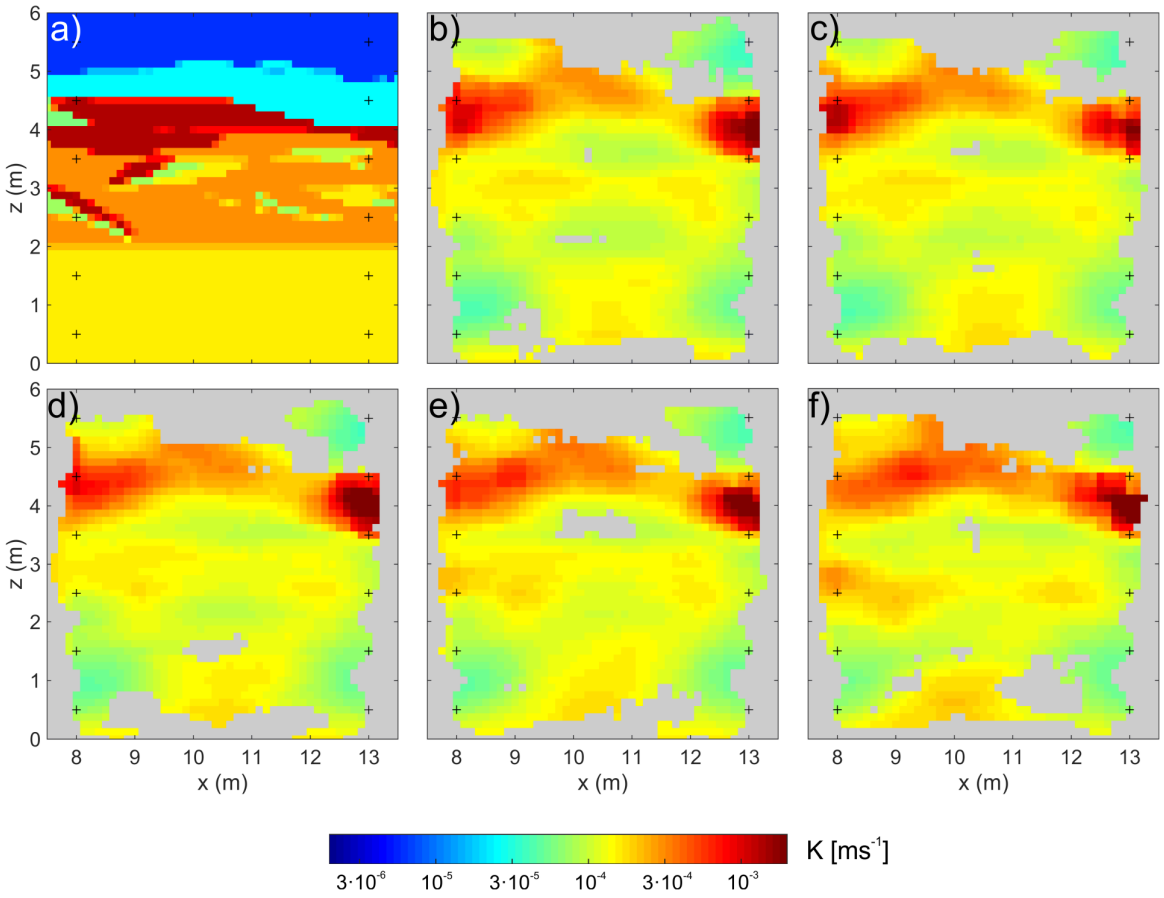

Figure 2-8. Hydraulic conductivity K reconstructions with different injection temperatures (ΔT). a) Original K profile, b) $\Delta T = 5$°C, c) $\Delta T = 10$ ˚C, d) $\Delta T = 20$ ˚C, e) $\Delta T = 40$ ˚C, f) $\Delta T = 80$ ˚C.

Figure 2-8 depicts the inverted K-tomograms for ΔT = 5, 10, 20, 40 and 80 °C. The results show that the inversion method is not very sensitive to ΔT. The tomograms slightly vary, but they all maintain the major features, and especially the central high conductive zone is identified similarly in all variations. Even with an extreme value of ΔT = 80 ˚C, no distortion appears. This is surprising because buoyancy effects are significant under such conditions. This is attributed to the use of early time diagnostics, which are mainly controlled by advective transport even if substantial thermal and density gradients prevail in the aquifer. The small differences in the K values can be explained by the changes in viscosity due to the heating. Being able to inject water with high temperature is considered advantageous, because this means that a strong signal is introduced, a high signal-to-noise ratio can be achieved, and a greater aquifer volume can be accessed. In practice, of course, maintaining a constant injection temperature at high temperatures can be a technical challenge, and requires more sizeable heating devices.

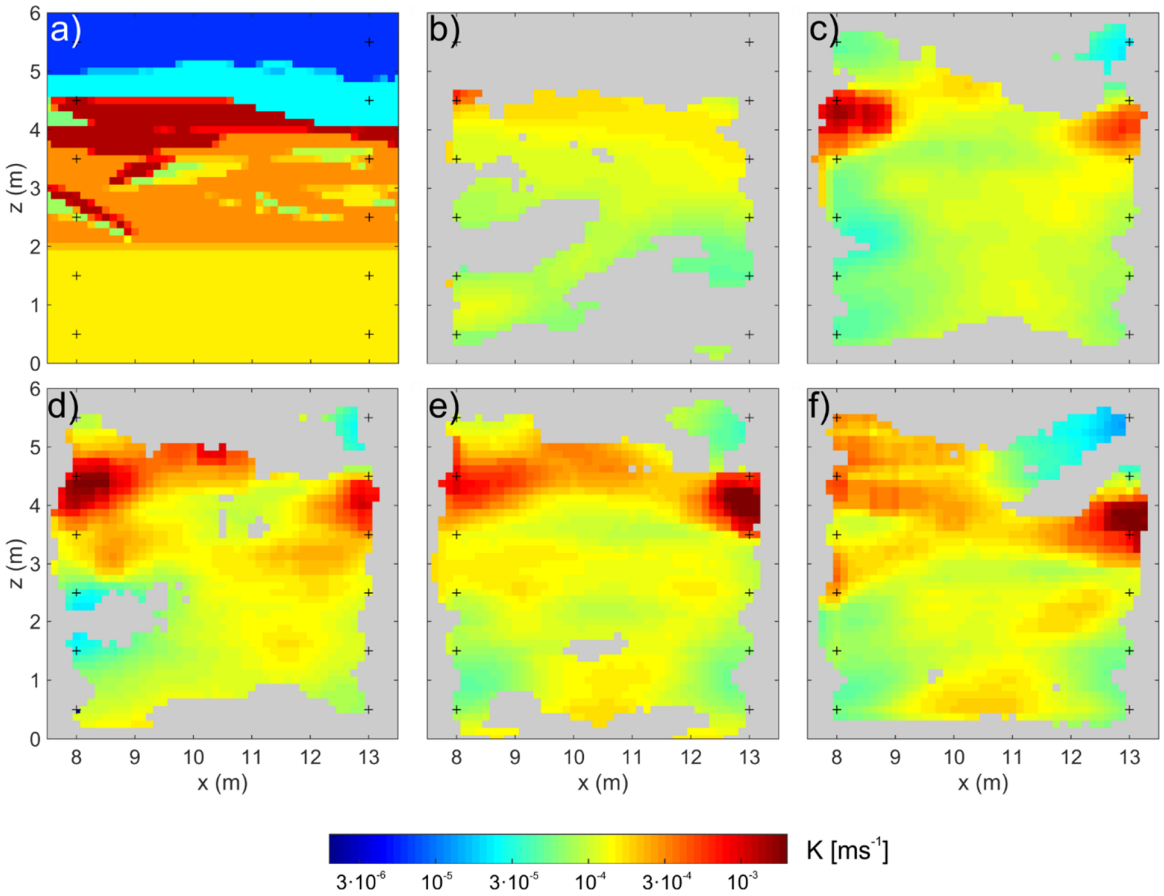

Figure 2-9. Hydraulic conductivity K reconstructions with different injection rates (Q). a) Original K profile 1, b) Q = 0.001 ls^{-1}, c) Q = 0.01 ls^{-1}, d) Q = 0.1 ls^{-1}, e) Q = 1 ls^{-1}, f) Q = 10 ls^{-1}.

The sensitivity of the injection rate, Q, is investigated on a range of four orders of magnitude, Q = 10^{-3}, 10^{-2}, 10^{-1}, 1 and 10 ls^{-1} (Figure 2-9). The injection temperature is fixed at ΔT = 20 °C. At small injection rates, the heat introduced to the aquifer is small; hence there is no detectable breakthrough at most of the observation points. As shown in Figure 2-9b, little insight is obtained with Q = 10^{-3} ls^{-1}, and the quality of the results is poor. Increasing the injection temperature can improve the quality of the result in this case.

By raising the injection rate, the reconstructed continuity of the central conductive zone improves (Figure 2-9c-e). For our particular case, this is attributed to the setup. Since the top two observation points are located in the upper low conductivity zone, this influences the reconstruction of the central high conductive zone.

In contrast, at the highest simulated injection rate of Q = 10 ls^{-1}, the derived tomogram is unsatisfactory close to the injection well (Figure 2-9f). This is caused by the highly distorted flow field. Our inversion procedure is based on the assumption that the hydraulic gradient

between the two wells is constant. This is not valid anymore, and the relation between inverted mean tracer velocity and hydraulic conductivity is not linear. This effect appears only at very high injection rates, in this case at Q = 10 ls^{-1}, which exceeds technical possibilities (with an injection temperature of ΔT = 20 °C this would mean 840 kW of thermal power for the experiment). The intensity of the effect of Q settings varies between the different zones. For instance, the lower part of the tomograms in Figure 2-9 is not affected.

2.4.4 Application window

The insight gained from variable injection rates and temperatures revealed that the presented tomographic inversion method is robust within a broad range, but has limitations. But what exactly are the limits? We tested a broad range of different scenarios to delineate a general application window, where the inversion method can be used to reconstruct the distribution of K in an aquifer. The parameters listed in Table 2-2, injection temperature, injection rate and ambient hydraulic gradient, were systematically varied within the given ranges. These ranges were rigorously set, and for reaching possible theoretical limits, some scenarios even exceeded the technically feasible range. Additionally, in the three profiles (Figure 2-3), the contrasts in the values of K were artificially modified. This was done by expanding or squeezing the original value range for a profile by a factor (range multiplier) between 0.1 and 100. As a result, the original structures of the analog were kept while the variance was changed.

Each inverted K-distribution was compared with the (scaled) analog profile, qualitatively and quantitatively. A first visual test showed whether major structures were reconstructed and the geometries are similar, especially focusing on the conductive zones (Figure 2-3). Only acceptable tomograms were kept for the subsequent quantitative analysis.

The quantification is based on an estimated connectivity time between the sources and the receivers. The connectivity time is calculated by converting the K-tomogram into a velocity field, using the Darcy equation. With this velocity field, the shortest travel route and time is calculated between all possible source-receiver combinations using the A* pathfinding algorithm (Hart et al., 1968). The root mean square (RMS) difference between the connectivity times on the original model and the inverted result is used to quantify result quality relatively to each other, and by this, define an optimal application window for the method.

For condensing the results into a normalized parameter space and plotting them in a 2-D coordinate system, two dimensionless parameters are selected: The thermal Péclet number (Pe_t) to characterize the hydraulic conditions of the subsurface and the effective injection power to describe the used technical parameters of the experiments. Pe_t is calculated separately for the four identified zones of the aquifer:

$$Pe_t = \frac{C_w q d}{\lambda} \tag{14}$$

where C_w is the heat capacity of the water, q is the Darcy velocity, λ is the thermal conductivity and d is the length scale, which is here set to unity thickness of the aquifer (d = 1 m). The used technical parameter effective injection power, P', is defined as:

$$P' = Q'\Delta T = \frac{Q}{qd}\Delta T \tag{15}$$

where the effective injection rate Q' represents a normalized rate related to prevailing groundwater flow velocity and calculated for the given length scale, d. Note that Pe_t and P' are not completely independent; using a higher injection rate can increase the Pe_t of a zone. Thus, the defined coordinate system is not orthogonal.

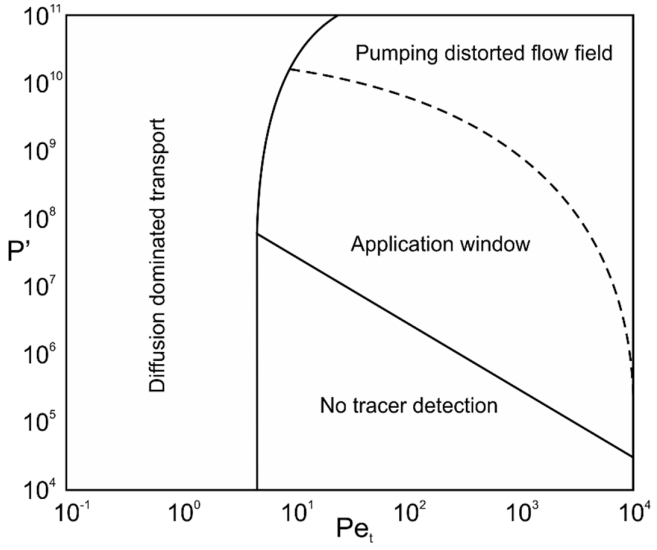

Figure 2-10. The proposed application window of the thermal tracer tomography – related to the injection parameters of the thermal tracer test - effective injection power (*P'*) - and the dominant transport process of the aquifer zone - thermal Péclet number (Pe_t). If Pe_t is below a critical value, the heat transport is diffusion-dominated, and no hydraulic information can be inverted from the tracer travel times. At low injection power, the temperature change at the observation points is below 0.1 ˚C and no detection is possible. At very high *P'* the high injection rate distorts the flow field and the results. The application window can help to find the ideal injection parameters based on the prior knowledge about the investigated aquifer.

After evaluating approximately one hundred different experimental scenarios, resulting in over 350 data points, the application window of the method is identified. In Figure 2-10 continuous lines mark strict boundaries between feasible and unfeasible regions (where beyond the line no reconstruction is possible), and dashed lines denote an approximate boundary where the result quality of tomograms start to decrease in the lateral direction (relative decrease in result quality).

If Pe_t is below a critical value, the inversion method is not able to provide any hydraulic information for the investigated zone because the assumption that the heat transport is advective is not valid anymore. In this region, the heat transport is governed by thermal diffusion, and no information on K can be extracted from the heat tracer data. These low K zones do not build on the resulted tomogram, but exist only as high null-space areas. A good example of this is the top low conductivity zone on Figure 8b-f, which is not reconstructed properly in any of the presented tomograms. Zones characterized by such low Pe_t are typically short-circuited via adjacent conductive zones. The critical Pe_t number rises non-linearly with the increase of P'. By raising Pe_t with higher injection rate, advection can be promoted in these zones. This provides some information for the tomogram, but the flow field is not short-circuited via an adjacent zone (Figure 2-7f), yielding a shadow-zone (top low-K zone).

At low P', the amplitude of the tracer breakthrough tends to be too small to be measured in enough observation points to successfully perform the K reconstruction. This strict limit for the application window is due to the assumed 0.1 ˚C limit for temperature measurement accuracy. It can be overcome by increasing the injection rate or temperature.

The result quality gradually declines towards high Pe_t and high P'. This is caused by the distortion of the flow field from high injection rates (see Figure 2-9f). Reconstructions, therefore, may still be acceptable beyond the given dashed boundary. Note that in practice, this region is infeasible, hence barely relevant. This is because it corresponds with an injection power of 500 kW - 1 MW, and thus this region is also technically infeasible or at least not favorable.

2.5 Conclusions

Early arrival times of tracer breakthrough curves (BTCs) are specifically suited for identifying highly conductive zones in heterogeneous aquifers. In our study we formulated a

procedure for combined inversion of multiple early arrival times measured during cross-well tracer testing. A tomographic set up with multi-level tracer injection and observation was implemented in a model with a 3-D high-resolution aquifer analog, and we examined the capability of the inversion procedure to reconstruct the heterogeneous distribution of hydraulic conductivity. Heat was selected as a tracer, which offers several advantages in comparison to many solute tracers, but its applicability is traditionally considered limited due to the higher diffusion and coupled thermal-hydraulic processes.

It is demonstrated that the tomographic interpretation of heat tracer signals is well suited for characterization of aquifer heterogeneity. By picking early arrival times, the impact of thermal diffusion, buoyancy, and viscosity variation is minimized and in this way, inversion becomes quasi insensitive to the temperature range. The presented application window of tested parameters of thermal tracer tomography is wide, and it covers three orders of magnitude for thermal Péclet numbers and five orders of magnitude for injection power. A key principle is that the transport in the aquifer is dominated by advection, and injection of hot water causes minor distortion. This can be controlled, for instance, by establishing a forced gradient between injection and observation point by operating an adjacent pumping well.

The travel-time based inversion is a fast and computationally efficient procedure, which delivers a tomogram in a few minutes with six sources and receivers. It is revealed that not only structures of mainly highly conductive zones could be reconstructed, but also the values of hydraulic conductivity were closely matched. This is appealing keeping in mind that the presented eikonal inversion is based on a rough approximation of groundwater flow and transport by a wave equation. Yet when close to strong contrast boundaries, the procedure is not able to reconstruct low conductivity zones due to short circuit-shadow effects. To reconstruct these hidden features, a further calibration step, or additional information would be required.

Acknowledgements

The aquifer analog data used in this paper (Bayer et al., 2015) is accessible from the Pangaea database under the link: doi.pangaea.de/10.1594/PANGAEA.844167. This work was supported by the Swiss National Science Foundation under grant number 200021_149128. We thank Rachael Colldeweih for language corrections and two anonymous reviewers for their constructive comments.

2.6 Appendix A. - Transforming the transport equation into eikonal equation

In the following, we present the mathematical procedure to transform the transport equation of a thermal tracer into the eikonal equation based on Vasco and Datta-Gupta (1999). First the solution of the transport equation is written as a series of wave functions. After neglecting the low frequency components, the transport equations is turned into the eikonal equation. Lastly, the travel time equation is presented as a solution to the eikonal problem.

The *transport equation* of heat reads as follows (Stauffer et al., 2013):

$$\frac{\partial T(\boldsymbol{x},t)}{\partial t} = \nabla[D(\boldsymbol{x})\nabla T(\boldsymbol{x},t)] - \frac{C_w}{C_m}\nabla\big(\boldsymbol{q}T(\boldsymbol{x},t)\big), \tag{A1}$$

where $T(\boldsymbol{x},t)$ is the evolution of temperature distribution, $D(\boldsymbol{x})$ is the thermal diffusivity tensor, C_w and C_m are the heat capacity of the water and the aquifer matrix, $\boldsymbol{q}$ is the Darcy velocity and $\phi(\boldsymbol{x})$ is the porosity distribution. Assuming that $D(\boldsymbol{x})$ is a single scalar value and separating the velocity to a direction ($\boldsymbol{u}$) and a magnitude ($a(\boldsymbol{x})$) term, the equation simplifies to:

$$R_t\frac{\partial T(\boldsymbol{x},t)}{\partial t} = D\nabla^2 T(\boldsymbol{x},t) - a(\boldsymbol{x})\boldsymbol{u}\cdot\nabla T(\boldsymbol{x},t), \tag{A2}$$

where R_t is the thermal retardation coefficient. The solution to this equation can be formulated as a series of wave equations (Fatemi et al., 1995). Using the complex wave functions as an asymptotic expansion, the solution becomes:

$$T(\boldsymbol{x},t) = e^{i\omega\sigma(\boldsymbol{x},t)}\sum_{n=0}^{\infty}\tau_n(\boldsymbol{x},t)(i\omega)^{-n}, \tag{A3}$$

where ω is the frequency and σ is the phase of the wave. Fast changes are represented in the initial terms of the series, and thus can be used ideally to describe tracer fronts. Keeping the first order terms and neglecting dispersion; after substitution Eq. (A2) simplifies to:

$$R_t\tau_0(\boldsymbol{x},t)\sigma_t(\boldsymbol{x},t) = -\tau_0(\boldsymbol{x},t)[a(\boldsymbol{x})\boldsymbol{u}\nabla\sigma(\boldsymbol{x},t)]. \tag{A4}$$

This assumption is weaken if the dispersion is stronger. The equation for the thermal front, where $\tau_0(\boldsymbol{x},t) = 1$ reads:

$$R_t\,\sigma_t(\boldsymbol{x},t) = -[a(\boldsymbol{x})\boldsymbol{u}\nabla\sigma(\boldsymbol{x},t)]. \tag{A5}$$

Taking absolute values:

$$|R_t\,\sigma_t(\boldsymbol{x},t)| = |a(\boldsymbol{x})cos(\theta)||\nabla\sigma(\boldsymbol{x},t)|, \tag{A6}$$

where θ is the angle between the flow direction and $\nabla\sigma(\boldsymbol{x},t)$. By introducing $s(\boldsymbol{x}) = |a(\boldsymbol{x})cos(\theta)|^{-1}$ the velocity vector perpendicular to the tracer front, the Eq. (A6) gives:

$$R_t\,s(\boldsymbol{x})|\sigma_t(\boldsymbol{x},t)| = |\nabla\sigma(\boldsymbol{x},t)|. \tag{A7}$$

Separating the temporal and spatial phase function the phase can be expressed as $\sigma(\boldsymbol{x},t) = \psi(\boldsymbol{x}) - t$ (Kline and Kay, 1965). After substitution and squaring Eq. (A7) transforms to:

$$|\nabla\psi(\boldsymbol{x})|^2 = s^2(\boldsymbol{x})R_t^2, \tag{A8}$$

where if we relate $s(\boldsymbol{x})$ to Darcy velocity:

$$s(\boldsymbol{x}) = \frac{\phi(\boldsymbol{x})}{R_t q} = \frac{\phi(\boldsymbol{x})}{(R_t K(\boldsymbol{x})|i(\boldsymbol{x})|)} \tag{A9}$$

if the temperature gradient is perpendicular to the tracer front ($cos(\theta) = 1$). Equation 8 is known as the *eikonal equation* (Nolet, 1987). Solution methodologies for eikonal problems are available from seismic or electromagnetic wave propagation applications. $\psi(\boldsymbol{x}) = t$ describes the thermal front and because its gradient is parallel to the local transport direction, we can relate it to the transport trajectories:

$$\frac{dx_i}{dr} = \lambda\frac{\partial\psi(\boldsymbol{x})}{\partial x_i}, \tag{A10}$$

where r is the distance along the trajectory and λ is a scaling factor. The value of λ can be chosen arbitrarily, and if we choose $\lambda = s(\boldsymbol{x})^{-1}$, Eq. (A10) returns the eikonal equation. With this substitution, Eq. (A10) reads:

$$\nabla\psi(\boldsymbol{x}) = s(\boldsymbol{x})\frac{d\boldsymbol{x}}{dr}. \tag{A11}$$

Because $d\psi(\boldsymbol{x})$ is equal to dt, after integration, the total travel time of the thermal front along the trajectory can be written as:

$$t_{total} = \int dt = \int s(\boldsymbol{x})dr = \int \frac{\phi(\boldsymbol{x})}{(R_t\,K(\boldsymbol{x})|i(\boldsymbol{x})|)}dr. \tag{A12}$$

This is the *travel time equation* for a thermal tracer.

3 Field validation of thermal tracer tomography for reconstruction of aquifer heterogeneity

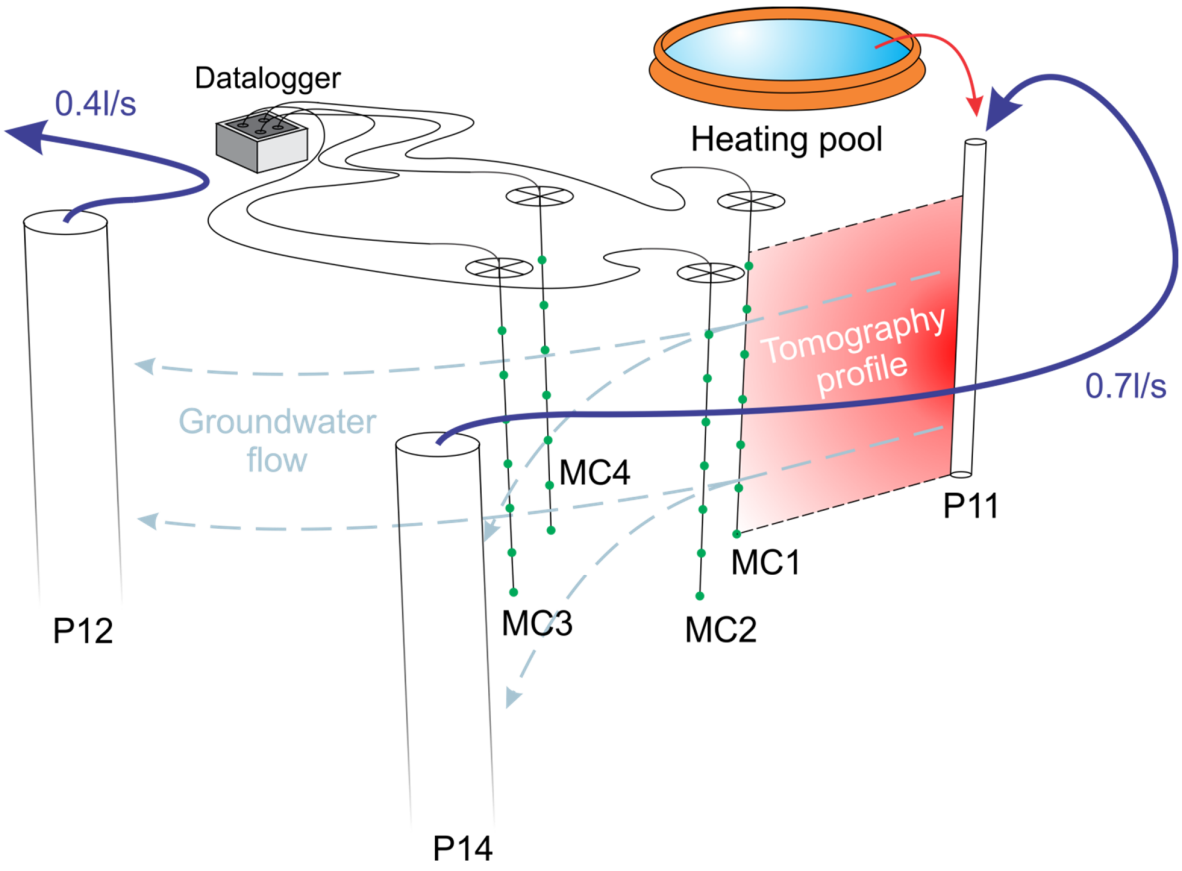

Manuscript submitted to Water Resources Research

Somogyvári, Márk and Peter Bayer. "Field validation of thermal tracer tomography for reconstruction of aquifer heterogeneity."

Abstract

In the summer of 2015, a series of thermal tracer tests were conducted at the Widen field site in northeast Switzerland to validate travel time-based thermal tracer tomography for reconstruction of aquifer heterogeneity. Repeated thermal tracer tests and distributed temperature observations were used to obtain a multi-source/multi-receiver tomographic experimental setup. After creating forced hydraulic gradient conditions, heated water was injected as a pulse temperature signal via a double packer system. With this solution, long temperature recovery periods were not required between the repeated injections at the expense of smaller observed temperatures. The recorded temperature breakthrough curves delivered a tomographic travel time dataset that was inverted assuming advection-dominated condition. The obtained hydraulic conductivity tomogram for a small aquifer profile is validated with the results of the findings from previous field investigations at the same site. The reconstructed profile confirms the presence of a thin sand layer with low-permeability, and reveals a previously unknown low-permeable zone close to the bottom of the aquifer. The inverted hydraulic conductivity values also correspond with those from previous tracer tests. Thus, the results of this study demonstrate the potential of thermal tracer tomography for resolving structures and transport characteristics of heterogeneous aquifers.

3.1 Introduction

Conventional single tracer tests in groundwater are integrative field investigation methods. They allow estimating average flow and transport properties of an aquifer volume (Yeh and Zhu, 2007). In contrast, geophysical imaging can capture subsurface heterogeneity by providing the distribution of electric conductivities, radar or seismic velocities. However, it is difficult to relate such geophysical parameters to hydraulic properties without additional hydraulic measurements (Linde et al., 2006). The rationale of tracer tomography is to combine tracer techniques with imaging methods. Tracers are injected in order to derive direct estimates of flow and transport parameters. Spatial heterogeneity of these parameters is resolved by applying multiple tracers in a tomographic set-up similar to geophysical measurements. Here, multiple different tracer injection points (sources) and multiple observation points (receivers) are used to capture the tracer breakthroughs at different locations and to delineate preferential pathways. Sources and receivers can be represented by different injection and observation wells, or, for vertical reconstruction of aquifer heterogeneity, they are situated at different levels in wells.

Hydraulic tomography is based on a similar principle by using the propagation of pressure signals generated by short-term pumping or slug tests (Butler et al., 1999). As these tests can be performed with similar instrumentation as for classic hydraulic testing, hydraulic tomography is well explored today (Berg and Illman, 2011; Brauchler et al., 2003, 2013b; Cardiff et al., 2009; Hu et al., 2015; Illman et al., 2009a; Vasco et al., 2000). Using tracers instead of hydraulic signals offers new opportunities, because tracer tests can identify directly preferential transport pathways, and they can be combined with hydraulic tomography in joint inversion procedures. Furthermore, the use of different types of tracers with different transport properties can reveal additional characteristics of the subsurface such as heterogeneity of matrix exchange surface or localization of non-aqueous phase liquids (Feehley et al., 2000; Illman et al., 2010; Wagner et al., 2014b; Yeh and Zhu, 2007; Zhu et al., 2009).

Inversion algorithms from seismic tomography can be directly used to interpret tracer tomography datasets (Vasco and Datta-Gupta, 1999). Tracer tomography is capable of characterizing porous (Jiménez et al., 2016) and fractured media (Brauchler et al., 2013a; Vasco and Finsterle, 2004). Datta-Gupta et al., (2002), Yeh and Zhu (2007), Zhu et al., (2009) and Illman et al., (2010) have demonstrated its suitability for identifying different liquid phases (such as dense non-aqueous phase liquids) in an aquifer. Field applications with multiple tracers are scarce, yet one has been presented by Jiménez et al., (2016) using different dye tracers and a pilot-point based inversion procedure to reconstruct an aquifer profile. This lack of field tests may be due to the demanding experimental design and instrumentation, the need for in-situ tracer monitoring or repeated multi-level sampling, and the time and cost for carrying out a full experiment. Therefore, tracers are more commonly applied to validate or complement other hydrogeological or hydrogeophysical field tests (Dorn et al., 2013; Jiménez et al., 2015; Sanchez-León et al., 2016; Sharmeen et al., 2012).

In recent years, heat as an actively injected tracer has raised increasing attention (Anderson, 2005; Rau et al., 2014; Saar, 2011). Irvine et al., (2013) pointed out that using heat over solute tracers provides better approximation of groundwater velocity at the expense of detecting heterogeneities. In comparison to the transport of solute tracers, conductive heat transport into the aquifer matrix can play a substantial role. This slows down the tracer transport (Shook, 2001) and the tracer signals are more attenuated since a large part of the injected energy is used to heat up the aquifer matrix. Due to the high diffusivity in comparison to solute tracers and the potential influence of background temperature

perturbations, heat is not considered an ideal tracer (Irvine et al., 2013; Xie et al., 2015; Xue et al., 1990). Aside from this, physical parameters such as hydraulic conductivity, *K*, are dependent on temperature. Water density and viscosity changes as temperature increases, and density driven flow is induced. Still, heat has some appealing features that make it favorable in many tracer applications, especially for tomography.

First, available temperature monitoring techniques can measure the evolution of temperature in-situ and real time, at high accuracy and at low cost. Multi-level observations are obtained by using multiple temperature sensors with fixed locations in the borehole or by using a distributed temperature measurements system (DTS). DTS systems use fiber optic cables for observations providing high spatial resolution (Bense et al., 2016). Temperature sensors are easier to use, cheaper and the better choices when point measurements are sufficient (Benz et al., 2015; Doro et al., 2015). Second, natural background temperature variations are often small, much smaller than changes induced by tracer tests. If necessary, background temperature trends can be filtered out using preliminary baseline measurements or frequency filtering. It is even possible to exploit the natural temperature differences inside the aquifer for investigations. This approach is especially suitable in fractured media where abrupt temperature changes can be caused by modifying the existing flow conditions. This technique has been used for fracture detection and characterization by Klepikova et al., (2014). Third, despite the strong influence of heat diffusion and density effects, thermal tracer testing in heterogeneous formations allows for the delineation of preferential pathways, where heat transport is dominated by advection (Djibrilla Saley et al., 2016; Irvine et al., 2013; Wagner et al., 2014b). In our earlier theoretical study Somogyvári et al., (2016), we have shown that by using a travel time based inversion technique, the influence of density changes, viscosity variations and diffusion effects are minimized and a wide application window for thermal tracer tomography is available.

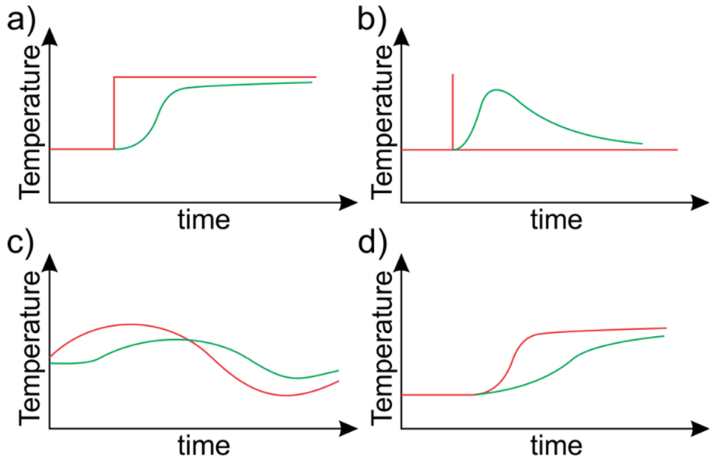

Figure 3-1. Different injected thermal tracer signals and observed responses. Red curves: injection signals, green curves: observed response signals. a) Heaviside signal with continuous thermal tracer injection, b) pulse injection, c) Injection of natural water with periodic temperature changes, d) in-situ conductive heat source.

Thermal tracer techniques can be categorized by the heat tracer source used. In the literature, four main source signal types are found, which create different response signals at an observation point (Figure 3-1). The most common source type is the step injection. Here the temperature at the injection point follows a Heaviside-signal shape (Figure 3-1a). This continuous thermal tracer injection can be realized by using a natural source with small temperature difference, for example water from another aquifer or an adjacent surface water body. Here, periodically changing temperature may be used for injection. In this case, the phase shift between the injected and observed signal can be investigated (Figure 3-1c) (Keys and Brown, 1978). A more common approach is to use an on-site heating device to produce warm water continuously (Cherubini et al., 2017; Colombani et al., 2015; Doro et al., 2015; Irvine et al., 2013; Molz et al., 1981; Palmer et al., 1992; Vandenbohede et al., 2011; Wildemeersch et al., 2014), because temperature changes can be self-defined and higher (Figure 3-1a). Although observations from step injection signals are easier to detect, their technical implementation with active heating devices is difficult. Maintaining a constant temperature injection signal for a long period requires a large amount of energy and reliable operation of the heating system. An alternative is heating up a small volume of water, which is then injected as a Dirac pulse signal (Djibrilla Saley et al., 2016; Wagner et al., 2014b) (Figure 3-1b). Pulse signals are standard in solute or particle tracer tests where a limited amount of tracer solution is available or needed. For thermal tracer tests, it is important that the injection volume and the temperature difference of the introduced water are sufficient to achieve detectable temperature changes in the observation well. Another option of generating

temperature anomalies is in-situ heating with a submersible heat source (e.g. heating cable) (Bakker et al., 2015; Coleman et al., 2015; Seibertz et al., 2016). Here, electrical energy is directly converted to heat in-situ with a conductive source (Figure 3-1d). No fluid injection is required for this variant if there is natural groundwater flow. However, the amount of energy introduced by heating is limited and the generated temperature signal will be relatively smooth, making it difficult for instance, to calculate tracer travel times.

Field applications of heat signals in tomographic arrangement are scarce. Doro et al., (2015) focused on the design issues of thermal tracer tomography, and reported a tomographic measurement campaign. However, no detailed aquifer characterization has been done using the collected data. Among the procedures available for tomographic inversion, geostatistical and travel-time methods have been suggested. The procedure by Schwede et al., (2014) assumes that the spatial distribution of log-K follows a random space function with known correlation. Also, the definition of mid-range clusters is recommended because the inversion is computationally intensive. Alternatively, computationally efficient travel-time based inversion has been suggested by Somogyvári et al., (2016). Travel-time based tomographic inversion methods exploit the similarities between the propagation of tracer fronts and seismic pressure waves (Brauchler et al., 2013a; Vasco and Datta-Gupta, 1999). Available solvers yield the distribution of the mean tracer velocities, which can then be converted to a K distribution. The potential and limitations of thermal tracer tomography were shown by means of two-dimensional (2-D) and three-dimensional (3-D) synthetic examples (Somogyvári et al., 2016).

The objective of this study is to further develop the travel-time based thermal tracer tomography concept presented in Somogyvári et al., (2016) and to validate it under field conditions. In the following, the theoretical background is provided first. Also, we present findings from preliminary field testing, which were used to prepare the setup of the full experiment. Based on this, a new thermal tracer tomography design is presented using pulse injections to minimize the temperature recovery times in the aquifer between sequential injections. The inversion methodology, originally developed for continuous thermal tracer injections, is adjusted to the use of pulse signals. We conclude with the results from field application and inverted K-profiles, which are compared to findings from earlier investigations at the site.

3.2 Methodology

3.2.1 Travel-time-based tomography

While heat diffusion obscures the contribution of advective transport in case of small flow velocities, it may be neglected in regimes with fast groundwater flow. Assuming that heat transport is dominated by advection, the properties of thermal transport can be related to the hydraulic properties of the aquifer. In this case, the travel times of thermal tracers can be directly linked to hydraulic conductivity, *K* (Somogyvári et al., 2016). The propagation of a thermal tracer front between two points can be described by modifying the original line integral formulation of Vasco and Datta-Gupta (1999) for tracer tomography by introducing the thermal retardation factor (R).

$$t_{tt}(x_r) = \int_{x_s}^{x_r} \frac{ds}{v_{tt}(s)} = \int_{x_s}^{x_r} \frac{\phi(s)}{R\,K(s)i(s)}\,ds \qquad (3\text{-}1)$$

Here, $t_{tt}(x_r)$ is the travel time of the thermal tracer at the receiver(x_r), x_s is the location of the heat source, ϕ is aquifer porosity and i is the local hydraulic gradient. Equation 3-1 is known as the travel time equation (or eikonal equation) of the thermal front between the source and receiver. The thermal retardation factor, *R*, describes the lag in the travel time of heat relative to a non-retarded solute. It depends on the aquifer porosity as well as on the heat capacities of the water and the aquifer matrix ($R = C_m/(\phi C_w)$). While the values of *K* of porous aquifers typically span orders of magnitude, variability in porosity, thermal retardation and hydraulic gradient are commonly much smaller. Thus the tracer travel time is most sensitive to an unknown distribution of *K*, and the other variables of Equation 3-1, ϕ, R and i are approximated by constant values. As these parameters span a small range of values, these approximations only introduce small errors into the results (Somogyvári et al., 2016).

The line integral of Equation 1 describes the relationship of the travel time to the velocity distribution along one transport trajectory. In a tomographic setup, multiple transport pathways dissect the aquifer. The velocity distribution of the investigated volume determines the tracer travel times. The set of travel time line integrals form the inverse problem. Inverting all the travel time equations together, this velocity distribution can be calculated. As the same formulation is used to describe the propagation of seismic signals or electromagnetic waves in geophysical tomography, standard inversion methods are available to estimate the velocity field. In this study, the SIRT algorithm is deployed to invert the travel

times of the heat tracer, implemented in the software GeoTOM3D (Jackson and Tweeton, 1996). The SIRT algorithm calculates the transport trajectories over a velocity grid and iteratively updates the values of the grid cells until the simulated and observed travel times match. As a result, the mean tracer velocity distribution (velocity tomogram) is obtained, which can then be converted to a *K*-field (*K*-tomogram) according to Equation 3-1. Instead of solving the problem over a regular grid, the staggered grid method is applied in this study (Vesnaver and Böhm, 2000) in line with related travel time based hydraulic tomography applications (Hu et al., 2015; Jiménez et al., 2013; Somogyvári et al., 2016). The inverse problem is solved over multiple coarse grids, shifted horizontally and vertically. This reduces the bias of the inversion caused by the relation of the source-receiver locations to the grid geometry. The final tomogram is computed as the average of all grids, with a final resolution equal to the used displacements. The main advantage of this method is that it provides higher resolution tomogram without compromising the stability of the inversion.

As the inversion only uses information from the transport pathways, the quality of the tomogram is variable in space. The reliability of the different parts of the tomogram is assessed by calculating the null-space energy map (Brauchler et al., 2013a, 2013b; Jiménez et al., 2013; Somogyvári et al., 2016). The null-space energy map is computed by singular value decomposition (SVD) of the tomographic matrix, which contains the length of each inverted transport trajectory in each grid cell. The null-space energy map values range between zero and one, whereas higher null-space means less reliable pixels. The null-space energy map is used to mask out non-reliable pixels from the result, especially zones which are not reached by the inverted tracer trajectories.

3.2.2 Breakthrough time calculation

The travel time-based thermal tracer tomography inversion presented in Somogyvári et al., (2016) uses continuous thermal tracer injections for source signals. It was shown that it is advantageous to use earlier diagnostic times of breakthroughs to reduce experimental times and distortions caused by thermal diffusion. The breakthrough times were assigned to the time when the first temporal derivative of the temperature peaked at the observation point. By this, the tomographic approach revealed to be especially suitable to reconstruct highly conductive zones in an aquifer, and applicable in a broad range of geological and technical conditions. This was synthetized in the form of an application window in our numerical study (Somogyvári et al., 2016).

For this study, pulse injection signals were chosen due to practical reasons and after preliminary field testing. This requires a different approach for breakthrough time calculation. When pulse injection is used, the travel time of the thermal tracer is the time when the temperature at the observation point peaks. Since heat is a relatively slow tracer (Shook, 2001), this time can be late – requiring long observation times, which may be prohibitive for tomographic setups with multiple sequential applications. The derivative of temperature peaks much earlier, and relating the derivative peak to the travel time could help to reduce the required experimental times. The corresponding procedure is developed in the following.

The thermal response of a thermal pulse (instantaneous heat injection) in an advective-diffusive and one-dimensional (1-D) environment can be analytically formulated as:

$$T(x,t) = \frac{{Q_{in}}^*}{4\pi Dt} \exp\left(-\frac{(x-ut)^2}{4Dt}\right) \tag{3-2}$$

This equation is modified following the available solution for solute tracers (Evans, 1983). This 1-D approximation is valid in the close vicinity of the observation point. ${Q_{in}}^* = \frac{Q_{in}}{V_u C}$ represents the heat source term, that is, the amount of heat injected over a unit volume V_u given the local heat capacity C. D is the thermal diffusivity. The first temporal derivative reads as:

$$\frac{dT(x,t)}{dt} = -\frac{{Q_{in}}^* \exp\left(-\frac{(x-ut)^2}{4Dt}\right)(u^2t^2 + 4Dt - x^2)}{16\pi Dt^2} \tag{3-3}$$

The thermal breakthrough time is defined as the time when the temperature peaks:

$$\frac{dT(x,t)}{dt} = 0 \tag{3-4}$$

while the "breakthrough time" of the derivative curve is:

$$\frac{d^2T(x,t)}{dt^2} = 0 \tag{3-5}$$

The second derivative of the temperature (Eq. 3-2) reads as

$$\frac{d^2T(x,t)}{dt^2} = \\ = \frac{{Q_{in}}^* \exp\left(-\frac{(x-ut)^2}{4Dt}\right)(32D^2t^2 + 8Du^2t^3 - 16Dtx^2 + u^4t^4 - 2u^2t^2x^2 + x^4)}{64\pi D^3t^5} \tag{3-6}$$

The analytical solutions of Eqs. 3-4 and 3-5 are complex, making it difficult to use in any further deduction. However, by neglecting the terms with higher order velocities (because groundwater flow is slow), the solutions can be simplified to

$$t(T' = 0) = \frac{x}{4D} \tag{3-7}$$

$$t(T'' = 0) = \frac{2x^2 - \sqrt{2}x^2}{8D} \tag{3-8}$$

Relating the breakthrough time to the peak time of the derivative with a transformation factor (α) is a technique used earlier for step signals in Somogyvári et al., (2016) and Brauchler et al., (2003). The transformation gives the relation between the breakthrough time, t_{BT} and the derivative time, t_{DT} :

$$t_{BT} = \alpha t_{DT} \tag{3-9}$$

Hence the travel time of the thermal tracer can be expressed as a fraction of the time of the derivative peak, with a transformation factor computed as

$$\alpha = \frac{t(T'' = 0)}{t(T' = 0)} = 1 - \frac{1}{\sqrt{2}} \tag{3-10}$$

Note that this expression is only valid with the strong assumption that the seepage velocity is small. Aside from this, $t = 0$ should be the time when the temperature starts to increase at the observation point similar to the early time diagnostics method in Somogyvári et al., (2016). The transformation procedure is illustrated in Figure 3-2a.

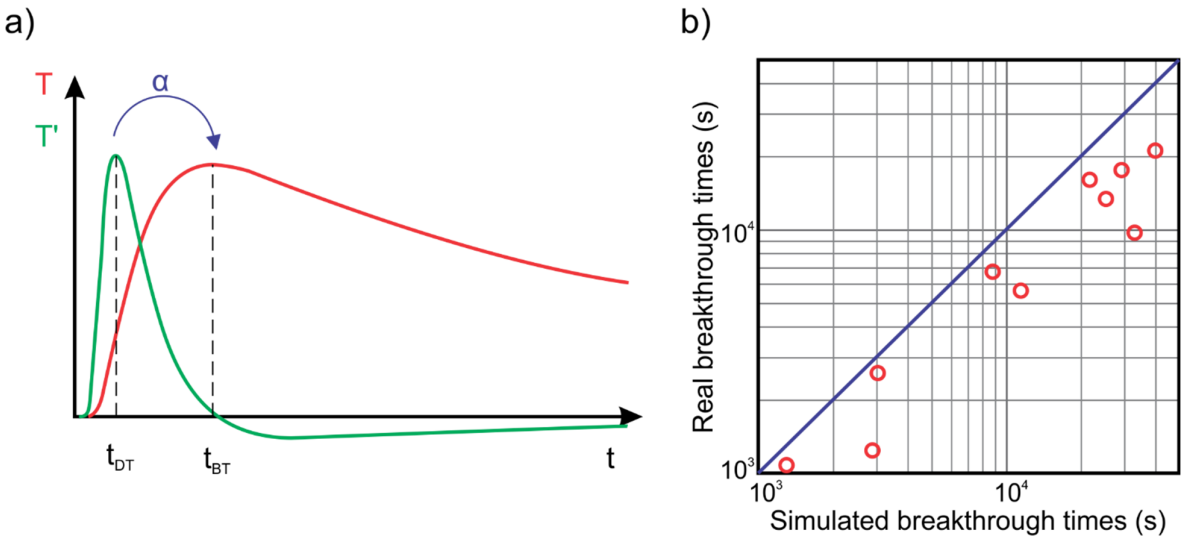

Figure 3-2. Breakthrough time calculation from temperature derivatives. a) Methodology of calculation. α is the transformation factor, t_{DT} is the peak time of the derivative temperature (T') and t_{BT} is the breakthrough time of the temperature (T). b) Comparison of the real breakthrough times versus the simulated ones using full recorded temperature breakthrough curves.

To validate this methodology, temperature breakthrough curves (BTCs) recorded in the subsequent field experiment are analyzed ex ante. The observed breakthrough times are compared with the simulated ones from the derivative peak (according to Eq. 9 and 10), as shown in Figure 3-2b. The derivative-based breakthrough times are always larger than the observed breakthrough times, which is problematic especially at smaller travel times. This limits the reliability of the inversion method. To overcome this, the derivative-based breakthrough times are only used to complement the dataset, when a thermal tracer test is terminated before the full BTC is captured. However, when the complete one was recorded, the measured peak breakthrough time was chosen. It is also possible that in the worst case, no temperature response is recorded at all, and thus no breakthrough time can be determined. However, this observation is also worthwhile, indicating limited connectivity between source and receiver or low-K zones in the aquifer. As travel time inversion formally only use breakthrough times as input parameters, such source-receiver combinations are included here by assigning virtual travel times. These virtual travel times are calculated assuming a straight transport trajectory between source and receiver and taking the lowest value of K estimated based on Eq. 3-1. The lowest K value is calculated from the largest registered travel time of the thermal tracer. With this extension of the dataset, a better reconstruction of the aquifer is expected, but with the added risk of wrong low-K values in the tomogram.

3.3 Field site and test design

3.3.1 Widen field site

The Widen field site is situated in the valley of the Thur river, in northeast Switzerland close to the city of Zurich (Figure 3-3). The field site was initiated in the summer of 2008. It has been investigated in several field campaigns (Coscia et al., 2011; Deuber et al., 2017; Doetsch et al., 2010; Jiménez et al., 2016) and used for education at ETH Zurich.

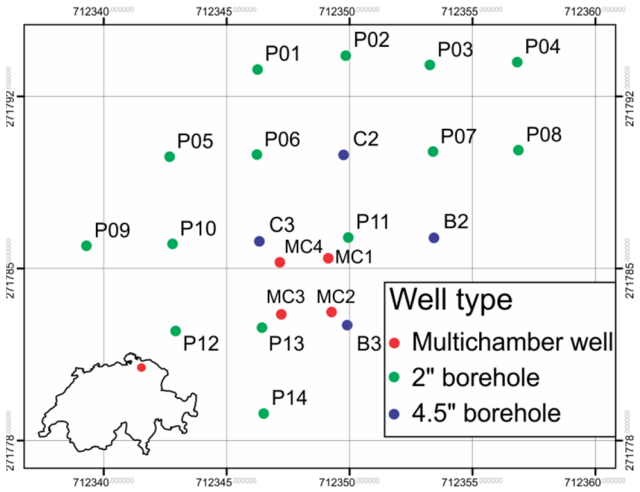

Figure 3-3. Well configuration at the Widen field site; the location in Switzerland is highlighted in the map at the lower left.

The site hosts a shallow aquifer dominated by the Thurtalschotter formation, a 7 m thick fluvial gravel layer (Figure 3-4). Below the aquifer bottom at around 10 m depth, low-permeable lacustrine sediments are found, while the aquifer is covered with around 3 m thick alluvial sand sediments. The depth of the aquifer bottom is variable within the field site as a consequence of fluvial erosion during deposition (e.g. between wells P11 and MC1). The aquifer is connected to the River Thur, and strong precipitation events cause changes in the water table. Normally, the water table is in the gravel formation yielding unconfined conditions. During flood events the aquifer becomes semi-confined as the groundwater reaches the overlying sand. The general groundwater flow direction is NE-SW, but deviations of up to 45° were experienced in different experiments revealing dynamic hydraulic conditions in the aquifer.

In the heterogeneous Thurtalschotter, sand lenses were found in core logs and by slug tests (Figure 3-4). Jiménez et al., (2016) identified the presence of a thin but extensive sand lens at 390 m level. The exact extent of this sand lens is unknown, but its presence was measured in

wells P11 and P13 by slug tests. Geophysical investigations (cross-well ERT) showed that the central zone of the aquifer body between 388 m and 390 m has higher electric resistivity than the formation above and below This suggests that the central zone of the Thurtalschotter formation has higher gravel content associated with higher *K*. Multi-level slug tests showed a wider zone of high-*K* between 387 m and 390 m, and another high-*K* zone above the 390 m low-*K* layer (Reist, 2013).

The Widen site hosts 22 investigation wells in total (Figure 3-3). 18 boreholes are aligned roughly as points of a rectangular grid (P01-P14, B2, B3, C2, C3). The boreholes penetrate down to the aquifer base and they are screened through the whole aquifer body. Four of the wells (MC1-MC4) are equipped with multichamber casings (Continuous Multichannel Tubing (CMT) (Einarson and Cherry, 2002)), which facilitate multilevel sampling. Each multichamber well has seven separate tubes inside, screened at seven different depth levels with 10 cm long screens. These wells were used for temperature measurements by installing sensors in each chamber.

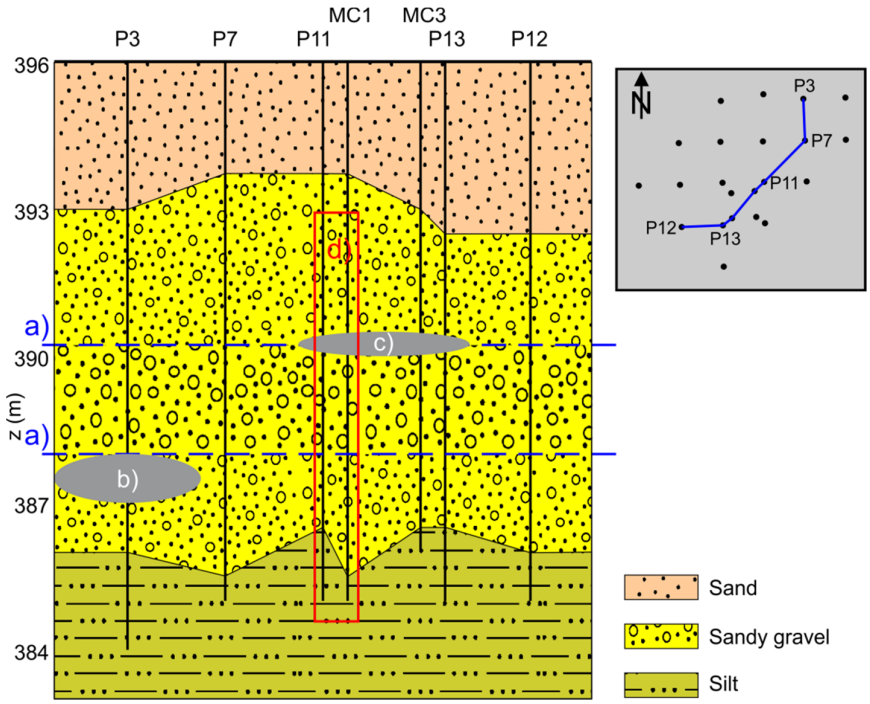

Figure 3-4. Summary of geological knowledge on the aquifer at the Widen site prior to the thermal tracer tomography experiment. a) Resistivity discontinuities in the aquifer bordering a high permeability layer, suggested by hydraulic tests and ERT measurements (Coscia et al., 2011; Doetsch et al., 2010; Reist, 2013). b) Sand lens known from core logs and slug tests (Reist, 2013). c) Sand layer (or lens) located by solute tracer tomography experiment (Jiménez et al., 2016). d) Trace map of reconstructed profile.

3.3.2 Preliminary testing

In the summer of 2014 a series of active thermal tracer tests were conducted at the Widen site, to test the continuous injection thermal tracer tomography design under field conditions (Schweingruber et al., 2015). A high performance diesel fueled water heater was used to produce 60°C water at a flowrate of 0.2 l/s. To minimize temperature variations, the heated water was mixed with cold water in a 120 l volume tank, finally providing a flow rate of 1 l/s at 30°C. We were able to operate this injection system for 60 hours, with variations less than 3°C in the injection temperatures. However, the experiment required constant operation of the heater, which was out of service several times. These short interruptions in the continuous injection caused significant distortions in the recorded BTCs. The heating also required a large amount of fuel to operate, making the experiment expensive. Doro et al., (2015) used a double packer system to vertically isolate the injection interval of the warm water. Additionally, above and below the injection interval, water at ambient temperature was injected. The additional injections focused the warm water to propagate horizontally in a similar way as laterologs focus the electric currents in borehole geophysics The setup we used was more simple. The warm water was injected in well P13 (Figure 3-3) via a double-packer system without any focusing of the heat plume as suggested by Doro et al., (2015). The injection is switched to cold injection with an estimated rate of 1 l/s after all warm water has been injected. To increase the hydraulic gradient, water extracted from well C2 was reinjected in well P14 with a rate of 3 l/s, generating forced gradient conditions. Temperature differences of over 10°C were observed in the closest observation borehole (MC3) at 1.5 m distance. Other boreholes have showed no or very weak responses, although sensors were capable to detect temperature changes below 0.05°C. This was the effect of the strong natural background flow, which was diverting the heat plume from the observation wells. Measurements after the injection experiment showed that close to the injection well the recovery back to the ambient temperature was very slow. This made it impossible to repeat the thermal tracer test on a subsequent day due to the disturbed initial thermal conditions in the aquifer.

Among the main findings of the preliminary test were that very small temperature changes are measureable in the low-noise subsurface environment. The high experimental costs, the huge risk of technical malfunctions and the long recovery time motivated us to consider an alternative heat injection procedure. This is explained in the following description of the full-scale tomographic experiment.

3.3.3 Experimental setup of thermal tracer tomography

With the experience from the preliminary testing campaign, the tomographic experiment conducted in the summer of 2015 was carefully aligned with the natural groundwater flow direction, and a pulse-type injection signal was employed. Pulse injection is advantageous, because less energy is required for heating than for continuous injection and the aquifer temperature can recover faster. These aspects are especially appealing for tomography, when multiple heat tracer tests are needed, but at the expense of less pronounced signals. Consequently, only a short profile of the aquifer is chosen for the test (P11-MC1, Figure 3-4). Figure 3-5 illustrates the experimental configuration. Two Grundfos JP Hydrojet surface pumps were used to maintain the forced gradient flow field in parallel with the ambient groundwater flow. The water extracted from well P12 at a rate of 0.4 l/s was discharged to the river, while the water extracted from P14 was reinjected to P11 at 0.7 l/s. Pumping was performed over the full well screen. The reinjection scheme represents a doublet-like setup, which adequately controlled the flow velocity and direction close to the heat injection well (P11). The pumps were started hours before the heat injection in order to reach quasi steady-state conditions. By injecting heat via a double packer system with a screen length of 20 cm, local point injection configuration was approximated.

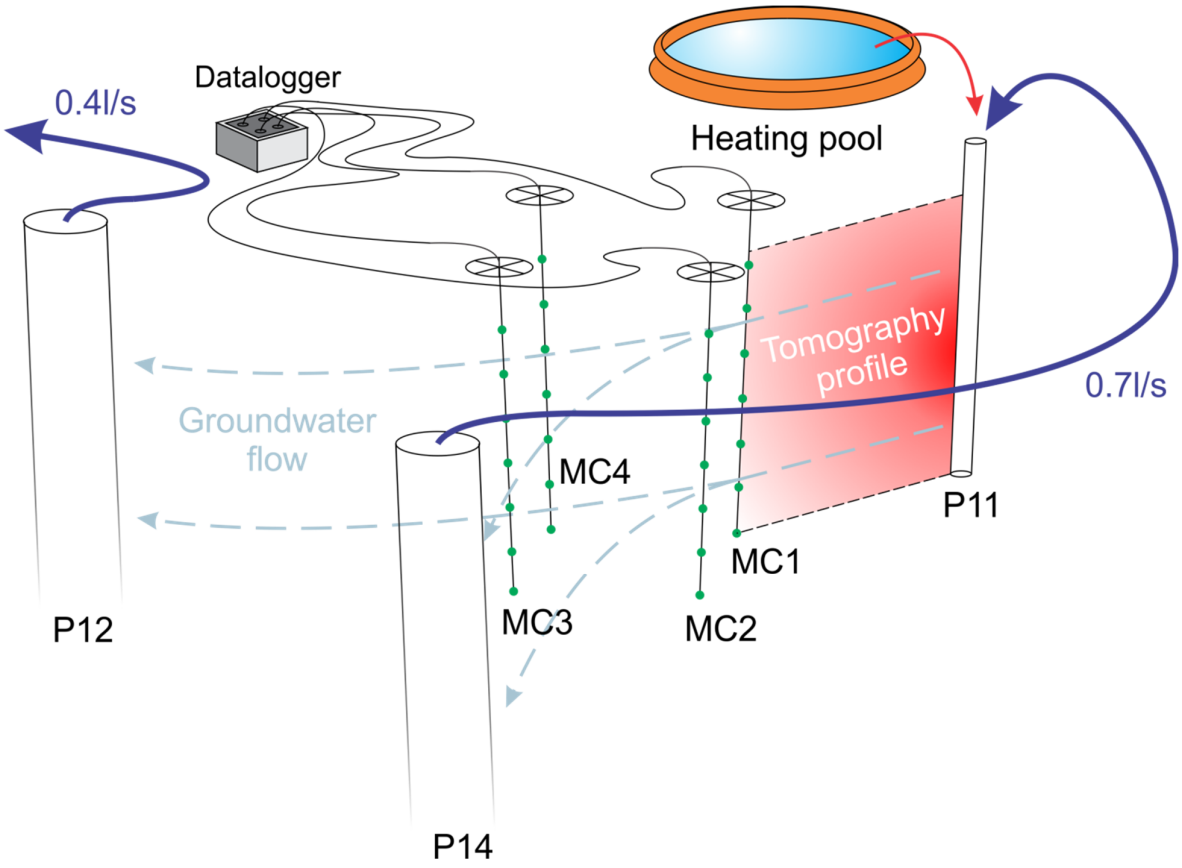

Figure 3-5. Experimental design of tomographic thermal tracer test: the water for injection is heated up by the sun in an inflatable swimming pool. The ambient groundwater flow is enhanced through a forced gradient setup. The temperature changes are monitored in four multichamber wells, with one meter vertical resolution.

To minimize the costs of the experiment, water which was taken from well P14 was warmed in three small inflatable swimming pools by direct sunlight (see also Wagner et al., (2014b)). During the sunny summer days of the experiment, 300 liters of water were heated up to 30°C in 3-4 hours from the ambient 15°C groundwater temperature. Before injection, the water was mixed in a fourth larger swimming pool, and directly injected to P11 over a period of approximately 10 minutes. Compared with the duration of hours for the full experiment, this short time interval was approximated as an instantaneous pulse injection. As the injection was performed without any pumping, the injection rate was reduced during warm water injection. This disturbed slightly the flow field for a short period, but it recovered immediately after switching back to cold injection. The tomographic experiment consisted four individual thermal tracer tests performed in four different injection interval. The different injection settings of all successive thermal tracer tests during the tomographic experiment are

summarized in Table 3-1. However, the given volumes of water were estimated and were not used for any further analysis.

Table 3-1. Details of the different thermal tracer injections of the main experiment.

	Start of experiment	Experiment duration (h)	Injection temperature (˚C)	Injection level (m)*
Injection 1	13.07.2015 16:06	6	30	389.075
Injection 2	14.07.2015 13:17	7	32	387.300
Injection 3	15.07.2015 13:01	3	32	390.075
Injection 4	15.07.2015 16:06	2	31	391.075

*Center of isolated interval.

Although the 15°C temperature difference at injection is over the 8°C limit of buoyancy driven flow given by Schincariol and Schwartz (1990), it is expected that the water cools down very quickly close to the injection point due to mixing and diffusion. The tomographic inversion is demonstrated to work at higher temperature differences with much higher injected volumes (Somogyvári et al., 2016). The latter theoretical study, however, focused on continuous heat injection, and thus the obtained findings cannot be transferred to the heat-pulse application of this work. The estimated thermal Peclét number of the high-K zones of the aquifer is in the range of Pe_t = 10 – 100, which denotes that the thermal transport is dominated by advection.

Campbell Scientific 108 temperature sensors with negative temperature coefficients were utilized for temperature measurements. The absolute accuracy of these sensors is smaller than 0.1°C, while temperature changes of 0.01°C were the smallest registered. Note that for travel-time based thermal tracer tomography the absolute accuracy of sensors is not crucial, as breakthrough times are calculated from relative temperature changes (see Figure 3-2a). In total, 28 temperature sensors were used, 26 installed in the multichamber wells (7-7 in MC1 and MC3, 6-6 in MC2 and MC4), and 2 additional ones monitored the air and the injection temperature. The temperature measurements were collected and recorded with a Campbell Scientific CR3000 datalogger, with 0.1 Hz sampling rate.

Four thermal tracer tests were conducted over three consecutive days to have minimal changes in the ambient hydraulic conditions. On the first two days, one thermal tracer test was executed per day and on the third day, two were performed. The overnight pauses were enough for complete thermal recovery of the aquifer. After the shorter pause of 3 hours

between the two injections on the last day, increased temperatures were measured, but the thermal breakthroughs could still be measured.

3.4 Results

3.4.1 Observations and data processing

The temperature observations of the four injection experiments delivered 104 BTCs in total. The BTCs are treated with a low-pass zero-phase filter (Oppenheim and Lim, 1981) to remove high frequency noise from the data. Such short time variations are related to instrument noise. A general feature of thermal tracer tests is that the recorded temperature curves can be well filtered. Natural background temperature trends have much lower frequencies, and disturbances from measurement noise have much higher frequencies than the tracer test signal.

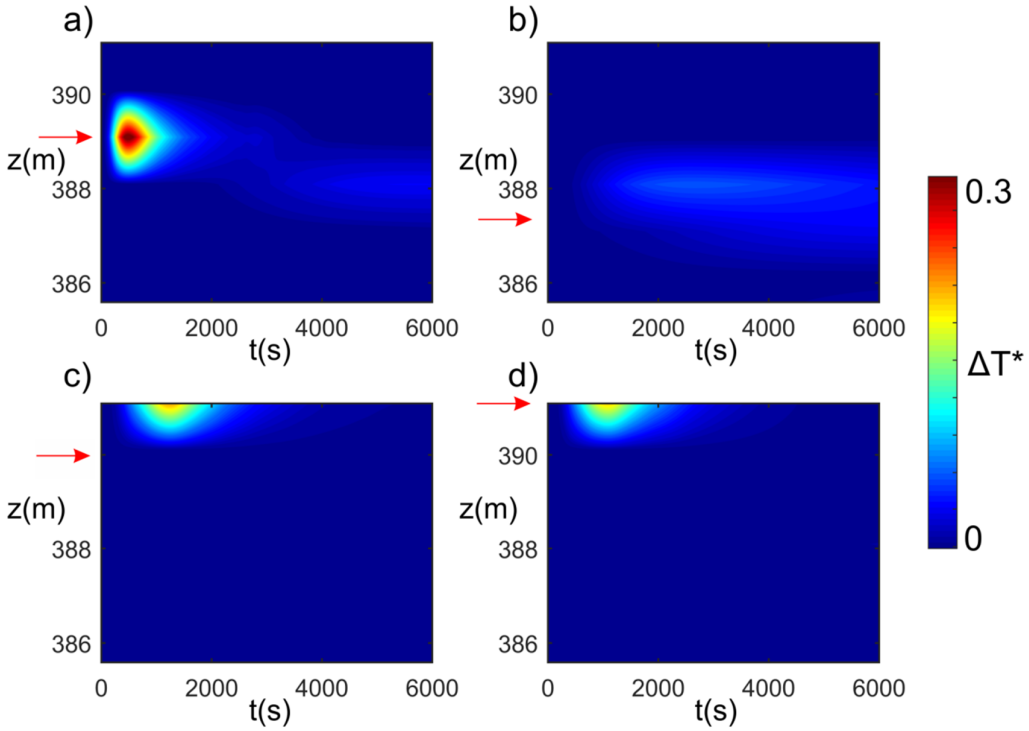

Figure 3-6. Normalized relative temperature changes ($\Delta T*$) observed in MC1 borehole after heat tracer injections in four different depths. The temperature differences are normalized by the average injection temperature (20˚C). The red arrows mark the depths of injections (sources).

Travel time based thermal tracer tomography does not use absolute temperature values for the inversion, but rather the travel times are calculated from the relative temperature changes.

These time-dependent changes are normalized by the injection temperature, ΔT^*, and shown in Figure 3-6 for the different injections observed in MC1. In Figure 3-6b and c, the observed temperature responses are not in the same depths as the injections. This is a first indication of inclined preferential flow paths in the Thurtalschotter.

Eleven BTCs were recorded during the tomographic experiment (supplementary figures S3-1-S3-3). Three additional travel times were calculated from temperature derivatives to complement the dataset (Eq. 3-9). For the 14 source-receiver combinations without any breakthrough, virtual travel times were estimated from the source receiver distance. Without these virtual travel times, the reconstruction of low-K aquifer zones would be limited. In total, 28 travel times were used as an input for the inversion. The collected BTCs are sufficient to reconstruct the 2-D profile between well P11 and MC1. Further information collected from the other multichamber wells could be used in additional experiments for a more extensive 3D reconstruction.

3.4.2 Parametrization of inversion procedure

An average hydraulic gradient of i = 0.005 dipping SW is calculated from head measurements of the four different tests. Further parameter values of the aquifer are taken from the literature and previous investigations at the site. The volumetric heat capacity of water is $C_w = 4.18 \times 10^6$ J/m^{3}K. The rock matrix is considered saturated gravel with a heat capacity of $C_m = 2.2 \times 10^6$ J/m^{3}K (Stauffer et al., 2013). An effective porosity value of ϕ = 0.25 is assigned (Reist, 2013).

The maximum allowed tracer velocity is constrained in the tomographic solver to keep the inverted tracer velocity values within a realistic range (Somogyvári et al., 2016). This is especially important for the edges of the inverse model, where due to data sparsity, the method could generate extreme values. The maximum allowed velocity of the inversion is set to 0.0023 m/s. This value is equivalent to $K = 5.5 \times 10^{-2}$ m/s (see Eq. 3-1), given the values for I, R and ϕ. To calculate virtual travel times, a value of $K = 6 \times 10^{-4}$ m/s is selected based on the largest detected travel times.

The cell size of the solution grids are defined as 1 m × 1 m. The optimal grid resolution for tomographic inversion has the same number of cells as the number of the inverted travel times (Vesnaver and Böhm, 2000). Here, 30 cells were fit to 28 BTCs. Inversion on higher resolution grids would lead to instable results due to the ill-posed inverse problem (Aster et al., 2013).

Four times staggering is used, shifted to both vertical and horizontal directions. Accordingly, the problem was solved on 16 different grids in total. The cell size of the final fine resolution grid is 0.25 m × 0.25 m. The required computational time on an office computer was less than 3 minutes for the complete tomographic inversion (Intel® Core™ i7-4770 CPU 4 × 3.40GHz).

3.4.3 Inversion results

The results of the inversion are presented in Figure 3-7. The reconstructed *K* values in the tomogram shown in Figure 3-7a are mostly above 10^{-3} m/s, with no pixel below 10^{-4} m/s. In the tomogram, a low-*K* layer embedded between two higher-*K* zones forms a layered sedimentary aquifer structure above 387 m. A sharp boundary at 390.5 m separates this low-*K* zone from the most permeable structure above. In contrast, the high permeability layer at 388 m shows smooth boundaries. It is not horizontal, but it shows a slight dip toward P11. A zone with very low *K* values is visible at the bottom right side of the profile below 387 m. Beneath this low-*K* zone a slight increase of *K* is found. This barely visible permeable structure provides the connection between the deepest injection and upper observation points, where breakthrough was detected (see Figure 3-6b). The bottom left side of the tomogram exhibits high *K* values. The thermal Péclet number even at the lowest inverted *K* values is still above 1, meaning that advection is the dominant transport process in every part of the aquifer.

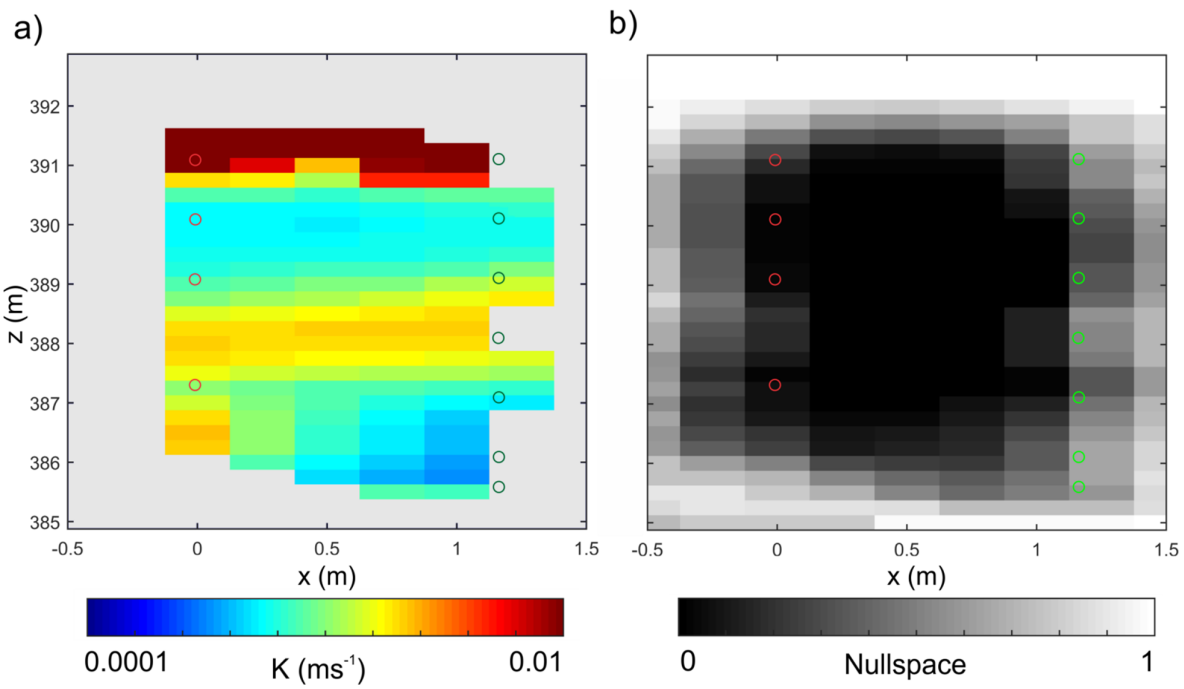

Figure 3-7. Results of the inversion a) Reconstructed hydraulic conductivity tomogram. Red circles are the point injections (sources) at P11, green circles are the sensor locations (receivers) at MC1. b) Null-space energy map.

Unreliable parts of the tomogram are masked out based on the null-space energy map. The null-space energy map in Figure 3-7b is calculated from the inverted transport pathways. Therefore, it reveals which parts of the profile were accessed by the thermal tracer. The low-*K* zone at 386 m for example exhibits a higher null-space compared to adjacent layers above and below, indicating that fewer transport pathways exist in this zone. Compared to other studies (Jiménez et al., 2013; Somogyvári et al., 2016), a null space energy value of 50% was selected as a threshold for reliable pixels. This value is much lower than previous studies (where e.g. 90% was suggested) because the inversion used fewer BTCs and coarser grid resolution. The reliability of the pixels changes gradually towards the edges of the tomogram. This makes it difficult to find a suitable null-space limit value compared to synthetic studies where this transition was sharper.

To validate the tomogram, first the reconstructed *K* values from well P11 are compared with multi-level slug test results from multiple wells nearby (Figure 3-8a). The slug tests were performed with 0.3 m spatial resolution over a screen length of 0.3 m (without overlapping intervals (Reist, 2013)). The derived profiles show similar vertical trends, but with different local features. While the slug test profiles show sudden changes between the tested intervals, the vertical changes in the tomogram are smooth. All profiles reach the minimum values

close to 390 m, but in the slug test profiles this low-*K* zone is narrower. An additional low-*K* peak is visible at 387 m in the tomogram profile, which cannot be correlated with local minimums of the slug test profile. The main difference between the slug tests and the tomogram is visible between 388 and 390 m, due to the large thickness of the low-K layer in the tomographic reconstruction.

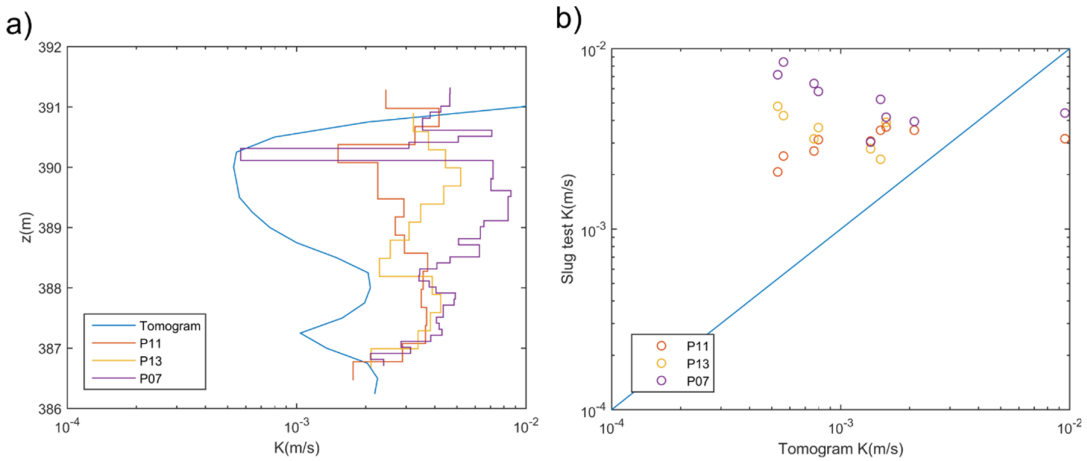

Figure 3-8. Validation of the reconstructed hydraulic conductivities, *K* a) Comparison of different hydraulic conductivity profiles. One profile is extracted from the *K* tomogram at the location of well P11 and compared with slug tests from wells P11, P13 and P07 (Jiménez et al., 2016; Reist, 2013). b) Scatterplot for the comparison of the *K* values of the tomogram and slug tests.

The inverted *K* values in the tomogram are lower than the values from the slug tests. This corresponds with the findings by Somogyvári et al., (2016), where thermal tracer based tomograms underestimated the *K* of the tested synthetic aquifers. This could be explained by the limitations of the assumption of purely advective heat transport. The *K* profile extracted from the tomogram changes over one order of magnitude. The range covered by the slug tests are significantly smaller. While thermal tracer tomography uses point sources and receivers and is only sensitive towards the flow direction, slug tests integrate *K* over the entire used screen length in 360°. This integrative behavior suppresses any large changes in the slug test profile, which apparently is better revealed by the thermal tracer tomography. Tomographic methods capture larger scale heterogeneities than localized slug tests (Vesselinov et al., 2001a, 2001b). The difference in the reconstructed *K* values is even more visible in the scatterplot shown in Figure 3-8b.

Compared to the findings of previous geophysical measurements (Coscia et al., 2011; Doetsch et al., 2010), the biggest difference is that the tomogram shows the highest *K* values above 390.5 m, while the ERT measurements suggested high *K* values between 387.5 and

390 m. The slug test result from P11 supports the result of the tomography (see Figure 3-8) since it shows the highest *K* values above 390 m as well. Note that this zone is very close to the water table level (391.8 m on the first day of the thermal tracer tomography campaign, similar for ERT measurements), which could cause artifacts in electric measurements for the ERT. The boundaries of both the thermal tracer tomography and the ERT reconstructions are close to this level, which could lead to less reliable results.

The tomogram of Figure 3-7 reveals a high-K layer in the center of the aquifer between 387.5 and 389 m which is in agreement with the geophysical results. Its inverted *K* value of 2×10^{-3} m/s is close to the 1.6×10^{-3} m/s value found by Jiménez et al., (2016) using joint inversion of solute tracer tomography and multi-level slug tests. So far, no hydraulic tomography experiment was performed at the same location. The same study suggested the presence of an extensive thin low-*K* sand layer at 390 m depth. This layer is also visible in the tomogram at the same depth, but is thicker. The cause of this difference may be that thermal tracer tomography tends to reduce high-*K* and increase low-*K* zones (Somogyvári et al., 2016). The inversion by Jiménez et al., (2016) was also performed jointly with slug tests, and the slug test profile indicated a very thin sand layer at 390 m (see Figure 3-8).

The inverted *K* values for the sand layer (around 4×10^{-4} m/s) in Figure 3-7 are close to the values found by Jiménez et al., (2016) for the same feature (3×10^{-4} m/s). The final *K* values of the tomogram are scaled by the used hydraulic gradient, porosity and heat capacity values, and any changes in these parameters would result in changes of the final result. However these changes are always small, because these parameters do not span orders of magnitudes and they are linear multipliers in the *K* calculation (see Eq. 3-1).

Although it was not known prior to the experiment, further indications of the deep low-*K* zone at 386 m have been found by the recent tracer tomography study of Deuber et al., (2017). In their experiment a low-*K* zone was reconstructed in an adjacent profile (between MC1 and MC3) at a similar depth. The low-*K* zone can be explained by the presence of a sand lens, similar to the one known from well P3. This sand lens is very close to the aquifer bottom, but the tomogram shows that a thin conductive channel separates them. The bottom boundary identified in the tomogram matches with the aquifer bottom geometry known from core logs. Here, the null-space energy values show an abrupt increase, as no transport pathway penetrates the low-*K* aquifer bed. Therefore this basal formation was not reconstructed.

3.5 Conclusions

Motivated by the promising results with synthetic cases, the presented work examined the suitability of travel-time based thermal tracer tomography in a field case. However, field experiments with multiple injections of heat can be technically demanding and time-consuming. Hence, a core issue was the development of a fast, simple and cost-effective test design, which would facilitate the first inversion of a thermal tracer tomogram in the field. As a test site, a heterogeneous alluvial aquifer was chosen, which was already investigated previously in field campaigns. By focusing on a small, 7 m deep cross section between two boreholes around 1.20 m apart, short-term and multi-level warm water injections in the one borehole were sufficient to detect different thermal breakthroughs in the downstream observation borehole. This saved time, equipment and heating devices, which would be required for more extensive continuous injections. Nevertheless, this also required modifications to the available travel-time based inversion procedure, which was originally developed for long-term injection. The new formulation is suitable for pulse injections and it also offers a way to approximate thermal breakthrough time from temperature-time derivatives. The approximation underestimates the real breakthrough time due to thermal diffusion. Thus it is only suggested here for estimating late breakthroughs, which are utilized to complement measured breakthroughs, ultimately obtaining a more complete dataset for tomographic inversion.

The chosen thermal pulse signals were employed sequentially over three days between the multi-level sources and receivers and the recorded signals in the downgradient observation borehole indicated major connections. In the experiment, forced gradient conditions were applied to establish a controlled flow regime with advection-dominated transport. This allowed a travel-time based tomographic inversion of the tracer breakthroughs to reconstruct hydraulic aquifer heterogeneity. A premise for applying this procedure is that further physical parameters that influence heat transport in porous media can be pre-determined or neglected. In that case, only the spatial K distribution governs the propagation of the thermal pulse in the aquifer.

The inverted tomogram was compared to findings from previous investigations at the field site and showed that similar features were captured by thermal tracer tomography. In particular, a known central low-K layer and the steep aquifer bed were successfully reconstructed on the tomogram. In addition, the magnitudes of inverted K values are

consistent with those from earlier hydraulic field investigations. A low conductivity zone in the tomogram at the bottom part of the aquifer is interpreted as a sand lens or local sandy zone, which is a common feature of the gravel hosting the aquifer. This is also validated by a recent field investigation with colloid tracers.

The presented thermal tracer tomography design provides a cost-effective alternative to using other tracers, like solute tracers for instance. Although the experimental times are longer because of the slower propagation of thermal signals, the recorded temperature breakthrough curves can be obtained real-time with highly sensitive sensors or DTS. The observed temperature breakthrough curves exhibit low noise and are thus ideal for travel time detection. For investigation of greater aquifer volumes, the thermal signals need to be adjusted, either by longer injection times or by higher temperature. Here, the challenge would be finding the balance between the amount of heat per injection and the temperature recovery time of the aquifer.

Thermal tracer tomography can be performed in par with hydraulic tomography experiments. The joint inversion of these two test types, could potentially increase the quality of reconstruction without significantly increasing the experimental costs.

Acknowledgements

This study was supported by the Swiss National Science Foundation under grant number 200021_149128. The field experiments at the Widen site has been conducted as part of the RECORD Catchment project. We thank Berrak Firat and Mischa Schweingruber for the help in conducting the field campaigns, and Rachael Colldeweih for language corrections.

Supplementary Information

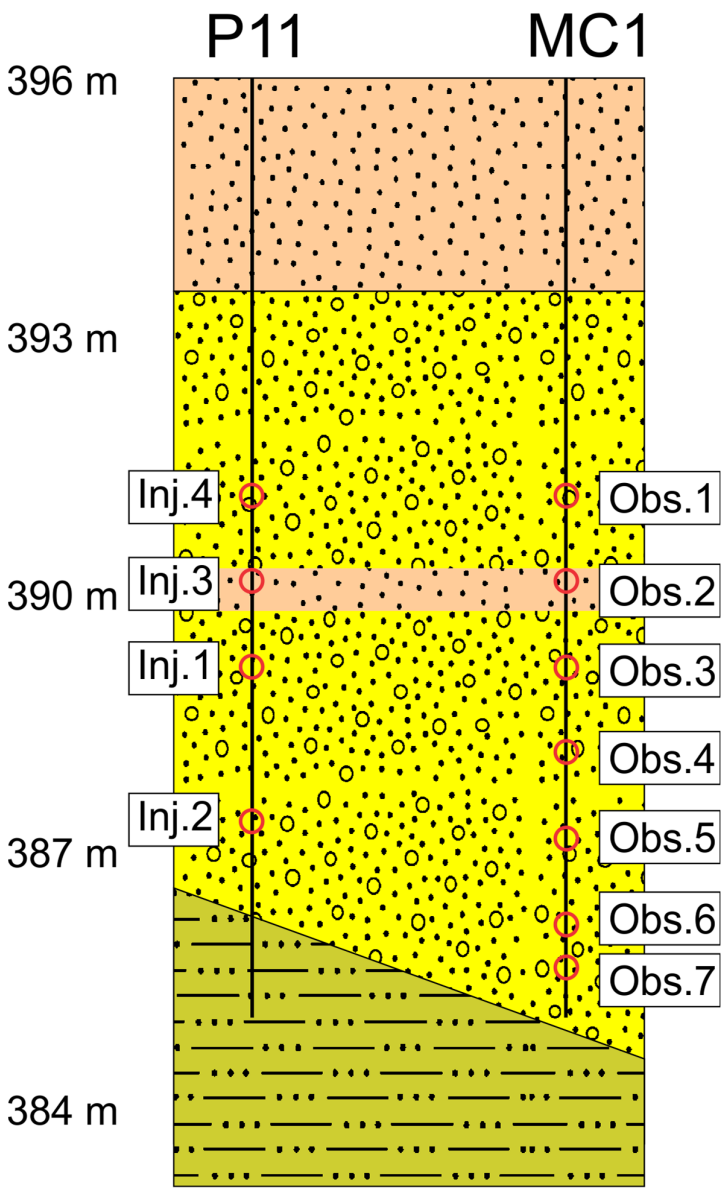

Figure S3-1. The location of injection and observation points.

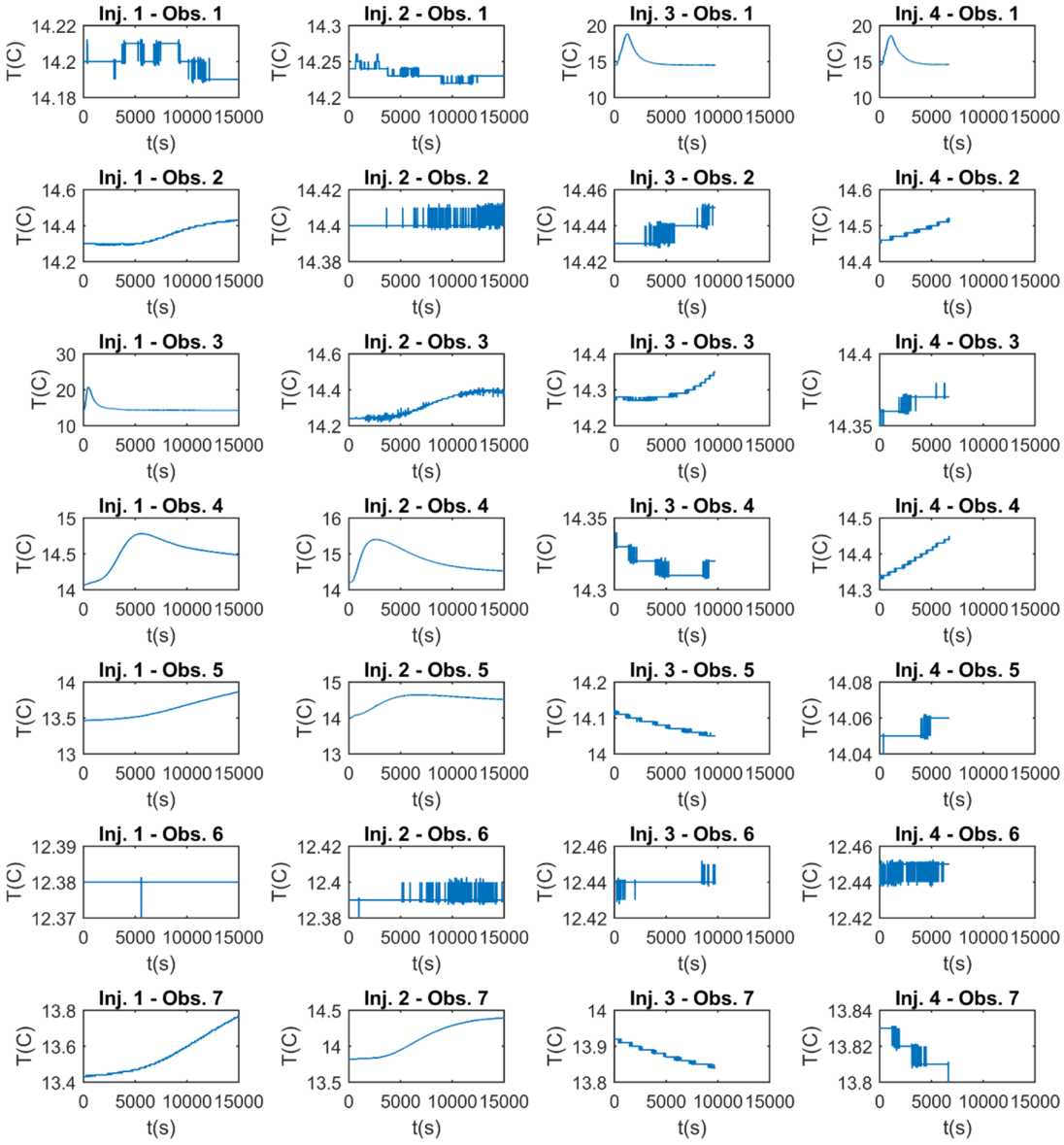

Figure S3-2. Recorded raw temperature curves of the thermal tracer tomography.

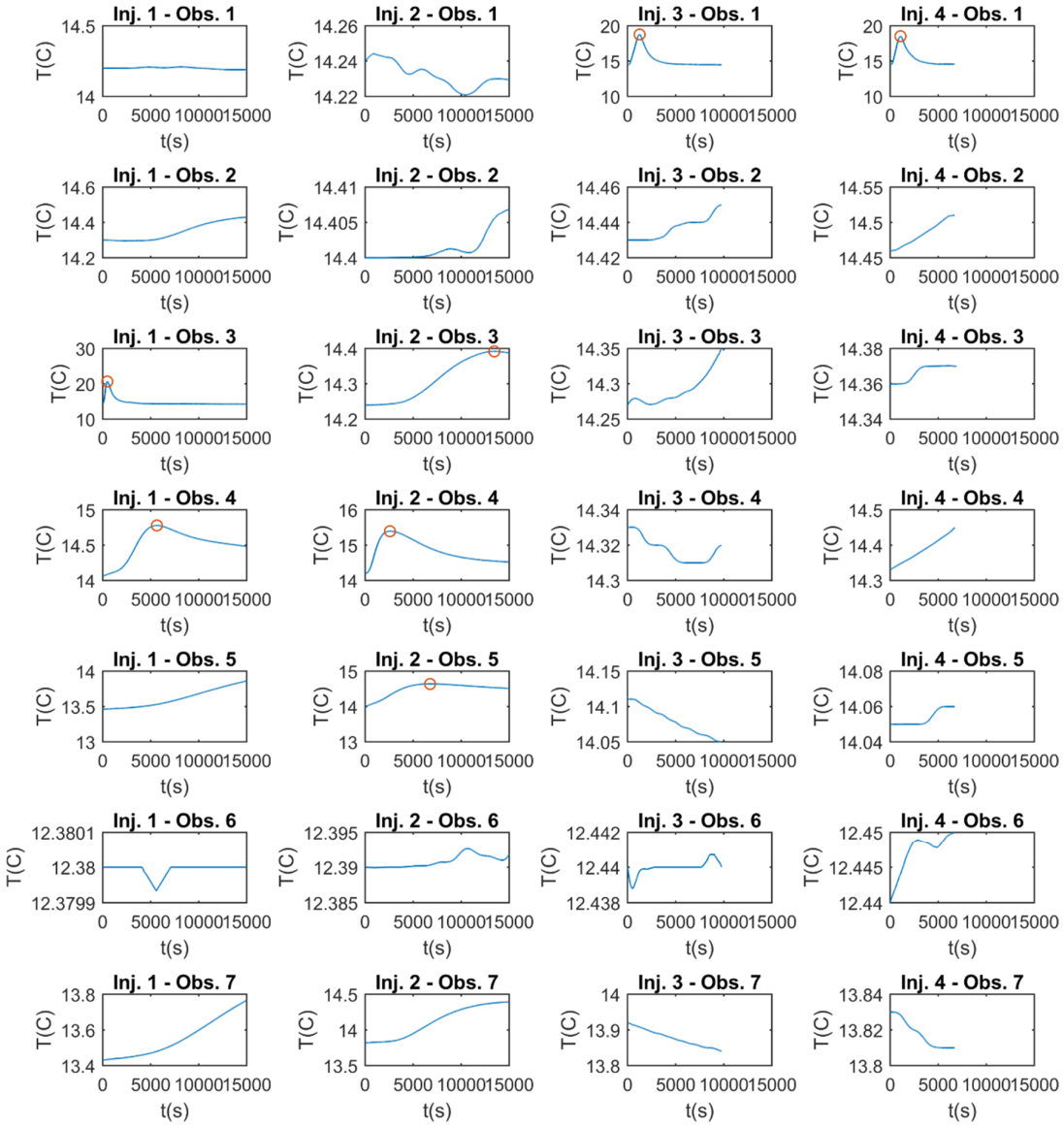

Figure S3-3. Temperature breakthrough curves after filtering. Red circles mark the detected breakthrough times.

4 Synthetic fracture network characterization with transdimensional inversion

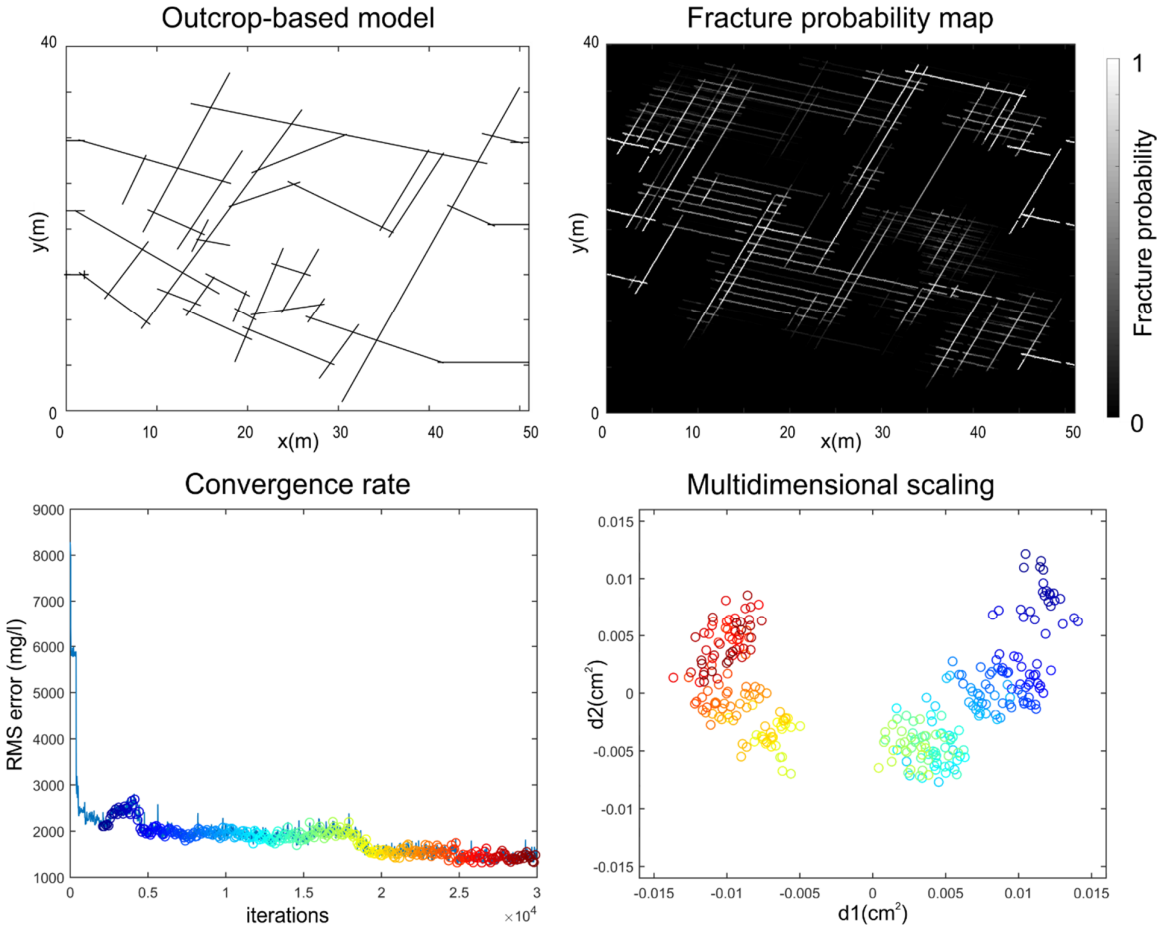

Manuscript submitted to Water Resources Research

Somogyvári, Márk, Mohammadreza Jalali, Santis Jiménez Parras and Peter Bayer. "Synthetic fracture network characterization with transdimensional inversion."

Abstract

Fracture network geometry is crucial for transport in hard rock aquifers, but it can only be approximated in models. While fracture orientation, spacing and intensity can be obtained from borehole logs, core images and outcrops, the characterization of in-situ fracture network geometry requires the interpretation of spatially distributed hydraulic and transport experiments. In this study we present a novel concept using a transdimensional inversion method (reversible jump Markov Chain Monte Carlo, rjMCMC) to invert a two-dimensional cross-well discrete fracture network (DFN) geometry from tracer tomography experiments. The conservative tracer transport is modelled via a fast finite difference model neglecting matrix diffusion. The proposed DFN inversion method iteratively evolves DFN variants by geometry updates to fit the observed tomographic data evaluated by the Metropolis-Hastings-Green acceptance criteria. A main feature is the varying dimensions of the inverse problem, which allows for the calibration of fracture geometries and numbers. This delivers an ensemble of thousands of DFN realizations that can be utilized for probabilistic identification of fractures in the aquifer. In the presented hypothetical and outcrop-based case studies, cross-sections between boreholes are investigated. The procedure successfully identifies major transport pathways in the investigated domain and explores equally probable DFN realizations, which are analyzed in fracture probability maps and by multidimensional scaling.

4.1 Introduction

Simulation of flow and transport in fractured rocks means dealing with highly structured systems with significant permeability contrasts, pronounced preferential flow paths, and characteristic anisotropies in the hydraulic parameters. Realistic reconstruction of fracture networks in numerical models is a challenge, which is commonly restricted by the limited amount of data and insufficient insight from field measurements (Berkowitz, 2002; Illman, 2014; Neuman, 2005). To get around these restrictions, concepts with reduced model complexity or with focus on relevant features such as a few prominent fractures are applied. Through these, estimation of model parameters can be simplified, and inversion problems are better posed.

Continuum models, for example, approximate the fractured rock as a smoothened and highly heterogeneous porous medium (equivalent continuum models (Illman and Neuman, 2003;

Sahimi, 2011) and stochastic continuum models (Day-Lewis et al., 2000; Hao et al., 2008; Illman et al., 2009b; Vesselinov et al., 2001a, 2001c; Zha et al., 2015)) and are able to delineate the main flow channels in an aquifer. These models are mostly limited to fracture networks which have a high fracture density (Long et al., 1982), and where flow channeling plays an important role (Sahimi, 2011). They cannot directly incorporate crucial structural information such as statistics on main fracture orientations or intensity. However, smoothening of discrete fractures allows for the use of established geostatistical space-filling methods, which are convenient for computationally efficient model inversion (Franssen and Gómez-Hernández, 2002; Illman et al., 2015; Schöniger et al., 2012; Yeh et al., 1996). Together with the use of data sets obtained from spatially distributed field measurements, well-constrained flow and transport models can be derived.

Spatially distributed measurements are fundamental to invasive tomographic tests such as hydraulic, pneumatic and tracer tomography (Hu et al., 2015; Illman et al., 2009b; Martinez-Landa and Carrera, 2006; Paradis et al., 2015; Zhou et al., 2016). Here, pressure or tracer signals are recorded between different sources and receivers (e.g. multiple well screens) and the data is inverted to image the spatial heterogeneity in the subsurface. Illman (2014) reviewed the state-of-the art in hydraulic and pneumatic tomography in fractured rock, with successful applications to synthetic models (Hao et al., 2008; Ni and Yeh, 2008; Zha et al., 2016), laboratory (Sharmeen et al., 2012), and field cases (Brauchler et al., 2003; Castagna et al., 2011; Franssen and Gómez-Hernández, 2002; Illman et al., 2009b; Meier et al., 2001; Ni and Yeh, 2008; Vesselinov et al., 2001a, 2001c, Zha et al., 2015, 2016). All of these applications utilize continuum models, which are calibrated based on volume-averaging multi-Gaussian geostatistical models, or utilizing smoothing regularization (Brauchler et al., 2003). Shortcomings are not only the limited realism of the models, but also continuum assumptions may yield unsatisfactory calibration of the hydraulic parameters, such as described in the work of Sharmeen et al., (2012). Here, hydraulic conductivity of the rock matrix was overestimated, which is considered a consequence of treating the fractured rock as a single continuum, or in other words, a result of underestimating the conductivity of fractures.

Discrete fracture networks (DFN) are realistic mappings of fracture geometries based on the field observation via a stochastic representation of fracture properties. Individual fracture geometry and fracture network connectivity are amongst the key parameters for such a realistic representation (Dorn et al., 2013; Frampton and Cvetkovic, 2010; Hestir et al., 1998,

2001; Jang et al., 2008; Li et al., 2014; Niven and Deutsch, 2012). DFN models could model flow and transport in fractured media, although the strong reliance on the cubic law makes these simulations very sensitive to aperture estimations (Neuman, 1988, 2005). Still, DFN models could better represent the fractured media than continuum models if the number of fractures is small. As a basis for DFN construction, statistical information of the fractured rock (such as fracture intensity) can be used, which is hard to exploit in continuum models. In field cases, however, this requires implementing highly parameterized fracture networks, which are difficult to adjust to hydraulic measurements. The biggest challenge of calibrating DFNs is the high number of parameters that would be required for individual tuning of each fracture. This is complicated by the expected non-convexity of the inverse problem, by insufficient data for unique model calibration, and by the need for flexible automatic network implementation in the numerical model during iterative calibration. For example, any change in the number of fractures within a DFN during the inversion process results in a change in the number of model parameters, making it impossible to use traditional optimization techniques.

Available automated calibration procedures could commonly reduce the dimension and complexity of inverse problems. For instance, Datta-Gupta et al., (1995) and Mauldon et al., (1993) simulate the fracture network via partially connected conductors with equal or variable apertures, aligned to a predefined lattice as a finite element approximation of the fractured system. Other concepts keep the number of fractures fixed while adjusting their hydraulic properties (Le Borgne et al., 2007; Dorn et al., 2013; Le Goc et al., 2010; Klepikova et al., 2014), activating-deactivating fractures (Hestir et al., 1998; Niven and Deutsch, 2012), or solving the problem over the statistical parameters of the DFN but not on the exact geometries (Jang et al., 2008). Dorn et al., (2013) suggested that using variable dimension DFN inversion would be a good choice to improve the capabilities of the existing DFN-based inversion techniques.

In this study we follow the suggestion by Dorn et al., (2013) and propose a new methodology that uses transdimensional Bayesian inversion (Green, 1995) to reconstruct the geometry of DFN models. This enables us to not only adjust the fracture geometries but also the number of fractures during the inversion procedure. Fracture network geometry is amongst the challenging properties to determine between boreholes. As prior information, statistical data available for fractured rocks is utilized. By processing data from tomographic measurements, most probable fracture locations and connectivities are identified.

4.2 Methodology

4.2.1 Simulation of tracer tomography

Tomographical methods use penetrating signals to obtain information of closed volumes by means of a multi-sources/multi-receivers setup. These set-ups deliver experimental data which, when inverted together, can be utilized to visualize subsurface structures. Tracer tests use injected substances (solutes or particles) or heat to map the pathways of transport in unknown aquifer systems. Conservative tracers do not decay or react with the flowing fluid or with the rock matrix. For tracer tomography, multi-level tracer injection is used (which is obtained by repeated tracer tests or by using multiple tracers at the same time) and the breakthrough curves are recorded at multiple depth points in downgradient wells (receivers) (Illman et al., 2010; Jiménez et al., 2016; Somogyvári et al., 2016). In fractured media, local injection can be achieved by using packer systems to isolate specific fractures. The new inversion procedure here is developed relying on virtual tomographic experiments simulated with given DFNs. Such a reference DFN serves as the "truth", which needs to be reconstructed by the inversion procedure. We focus on 2-D models of vertical DFN profiles investigated by tomographic cross-well testing. After simulating conservative tracer injections in one well, the breakthrough curves at the other well represent the observations that are used for calibration.

For forward simulation of the experiments, a fast and robust hydraulic model has been developed to simulate the pressure and tracer propagation inside the fracture network. This model is based on an implicit finite difference approach and has the capability to solve for both steady state and transient conditions. For simulating the tracer experiments, the steady state solutions are used. Only the fracture network in the domain is discretized and it is assumed that the matrix is impermeable and does not react with the tracer. Tracer diffusion between the fractures and the surrounding rock matrix is neglected (Neretnieks, 1980). These assumptions are approximate, but appropriate for formations such as crystalline rock. By simulating a vertical cross section between two wells, the thickness of fractures is assumed to be unity (perpendicular to the 2-D DFN plane) and fracture aperture and length control the storativity of each fracture element. Fracture conductivity for each element is calculated using the cubic law, assuming each fracture segment consists of two parallel plates (fracture walls).

Initially, the mass conservation equation for a control volume without any chemical reaction is solved until a steady state condition is satisfied. A constant pressure gradient is applied between the injection and monitoring boreholes and the pressure propagation is calculated using an implicit finite difference method (backward time, centered space method "BTCS"). The 2-D assumption requires the use of pressure boundary conditions, which is considered appropriate in low permeability rocks. The fracture's flow rate is related to the fracture pressure gradient via Darcy's law. The output of this simulation is the pressure and velocity field in the discrete fracture network.

The advection-dispersion equation is then solved for the fracture network as a result of the tracer injection at the source interval. In this case, an implicit and upwind finite difference method is implemented in order to overcome the instabilities introduced by the central differencing scheme after tracer injection initiation as well as at the tracer front. Two reasons can be mentioned for the observed instabilities in the transient advection-dispersion problems: advection dominated flow (i.e. high Peclet number) and sharp gradients during small time steps as a result of transient solution. Brooks and Hughes (1982) showed that these instabilities could be overcome using the upwind solution of the differential equations. The forward model will then estimate the concentration field in the fracture network and the tracer breakthrough curves (BTCs) for selected monitoring points in the observation well.

4.2.2 Principles of transdimensional inversion

While traditional inversion methods solve inverse problems over a predefined set of parameters (Menke, 1984), transdimensional inversion techniques vary the number of parameters during the inversion process and solve the problem over an a priori unknown number of parameters (Sambridge et al., 2012). Dealing with an unknown number of parameters increases the complexity of the inverse model. However, this may be compensated by lowering the number of model constraints, and by replacing several independent inverse model runs with different fixed problem dimensions by one transdimensional run. Green (1995) proposed a Bayesian concept of sampling from the posterior probability distribution of a transdimensional inverse problem. This reversible jump Markov Chain Monte Carlo (rjMCMC) method (also known as Metropolis-Hastings-Green (MHG) algorithm) has become the most popular inference method to handle this problem and has also made its way to geosciences. The method has shown to be effective on tomographic problems where the inverse model is defined as a spatial distribution of parameters. Bodin

and Sambridge (2009) have proposed an rjMCMC application for seismic tomography and Jiménez et al., (2016) utilized the concept to invert tracer tomography experiments in porous media with pilot points. Mondal et al., (2010) used rjMCMC to resolve porous flow in heterogeneous media and Mardia et al., (2007) employed the method for fractured rock modelling based on the structural data from borehole intersections. Mardia et al., (2007) reveals the suitability of rjMCMC as a flexible plane fitting algorithm to orient fractures in space, assuming that prior knowledge on fracture properties or borehole data is available. Fractures in a DFN model are usually oriented with given statistical properties, and rjMCMC is a probabilistic sampling procedure especially suited for handling parameter distributions. Their approach, however, does not consider calibration to observations from tomographic experiments. In fact, hydraulic and tracer tomographic measurements provide additional insight and thus have the potential to better reconstruct those fractures relevant for flow and transport. Tomographic experiments for DFN calibration will be considered here.

A Bayesian approach requires that all information is handled as random variables, in the form of probability density functions (PDF). The goal of Bayesian inference is to map the posterior probability distribution of the problem (Gelman et al., 2004). The posterior probability is determined by the available prior information and the likelihood of the observation data. Using Bayes' theorem, the posterior probability can be written as:

$$P(\theta|\xi) = \frac{P(\xi|\theta)P(\theta)}{P(\xi)} \qquad (4\text{-}1)$$

where $P(\theta|\xi)$ is the posterior probability distribution, the probability of a model parameter set (θ) given the observation data (ξ). $P(\xi|\theta)$ is the likelihood function of the observation data, or the probability of observation data (ξ) given the model parameters (θ). $P(\theta)$ is the available prior information of the model parameters before observations are made. $P(\xi)$ is the PDF of the observations. This term is independent from the model parameters, so it can be considered constant throughout the modeling. When the posterior of a problem cannot be expressed in an analytical form, a purpose-built sampling algorithm can be used, such as the rjMCMC method. This perturbs the model parameters and can also vary their number (the dimensionality of the problem).

4.2.3 DFN inversion procedure

Figure 4-1 depicts the DFN inversion procedure. In this study, the examined model parameters are the geometrical properties of the fractures; i.e. their locations and lengths. For

this initial inverse modelling effort the physical properties of the fractures such as apertures are considered constant and uniform for each fracture set. Our studied reference DFNs are built up by two fracture sets with different inclination angles and apertures, as fractured rocks are often dominated by two fracture sets (Valley, 2007; Ziegler et al., 2015).

The fracture length distribution (FLD) is one of the key statistical properties. In natural rocks, smaller fractures are more frequent than larger ones. A common approximation for this trend on a field scale is to use a power law (Torabi and Berg, 2011). In models, truncated FLDs are used. As very short fracture segments are less relevant for flow and transport, they are excluded in our work (see Figure 4-2b). Fracture intensity is calculated as the total length of fractures over the investigated area (La Pointe, 1988). Additionally, a technical parameter, the discretization length, is defined. It represents the resolution of the forward model, and thus determines the scale of geometric manipulations. Accordingly, in our approach, the DFN models are built up from straight fracture segments, with lengths taken from a discretized FLD. The interconnections between the fractures are also spaced according to the predefined discretization length.

The inversion procedure (Figure 4-1) is initiated by randomly generating a DFN realization, *r*, based on given statistical properties. It is implemented in a forward model and evaluated by comparison to the observations. In each subsequent iteration, a new DFN realization is proposed by sequentially updating the geometry of the previous one. The rjMCMC algorithm is reversible by definition (Green, 1995). Reversibility means that the algorithm runs with the same rules backward as forward. This is considered when defining the following three geometry updates: fracture addition, fracture deletion and fracture shift.

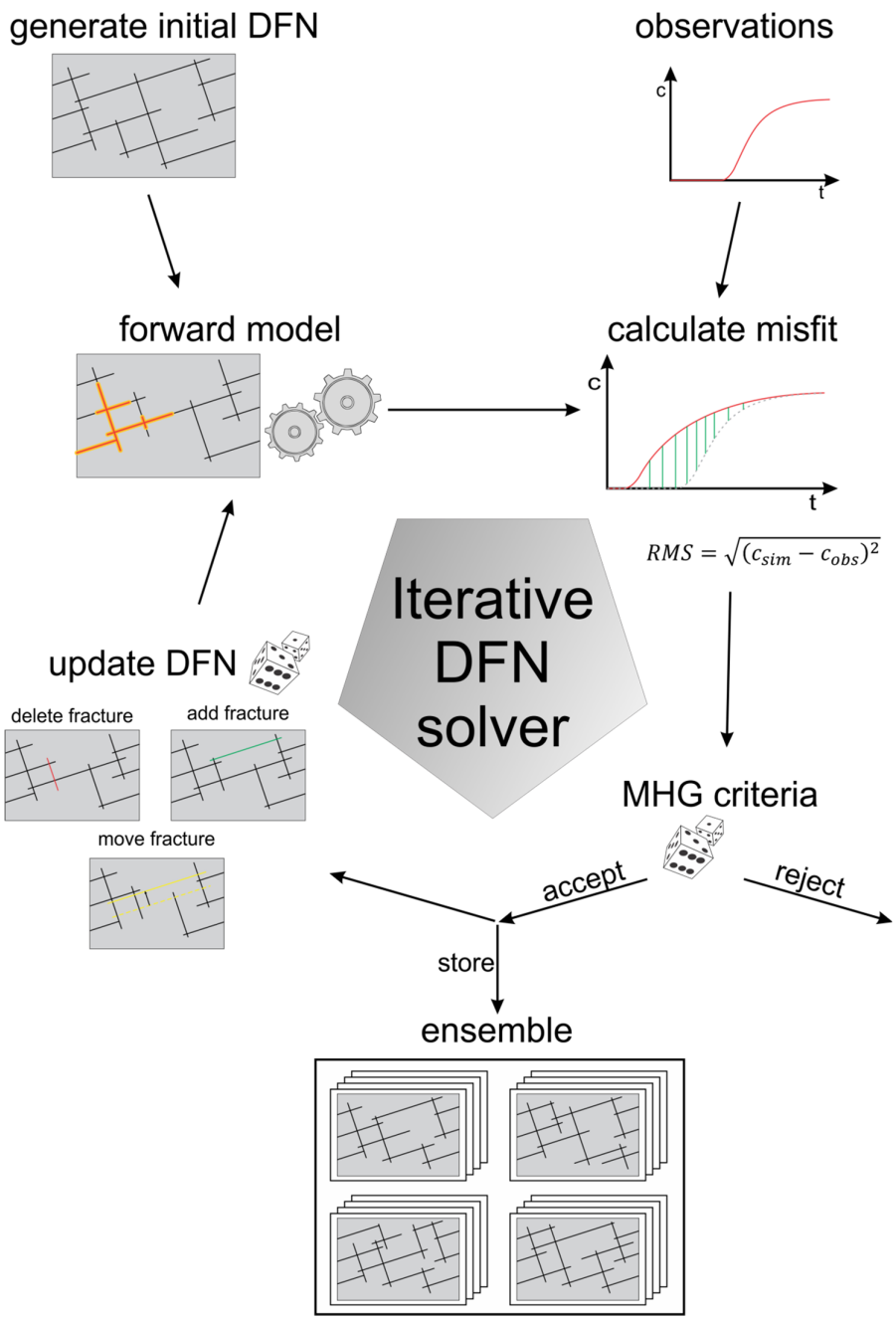

Figure 4-1. Overview of the DFN reconstruction algorithm. The reconstruction starts from a random generated initial solution and the input of the method is the experiment data. The steps of the iterative DFN solver are the following: update DFN model, simulate tomography, calculate misfit, accept or reject the updated DFN. The accepted DFN realizations are stored in an ensemble, which serve as the output of the algorithm.

Fracture addition is the so-called birth move of the rjMCMC algorithm, where the dimensionality of the problem is extended and one new fracture is added to the DFN. There are several rules concerning this update. For example, the position of the new fracture is drawn randomly, but not over the whole domain, as the added fracture is always connected to

the DFNs. This is important to maintain the reversibility of the algorithm. The length of the added fracture is drawn from a prior fracture length distribution (FLD). This FLD is recalculated after each update to guide the actual FLD toward the initially defined FLD. This recalculation is needed, because the fracture deletion update does not obey any FLD rule. Since it draws from the initially defined FLD, it would yield a distorted FLD. The addition update has three substeps (Figure 4-2a-c):

- First, the fracture set and the insertion point are randomly selected (Figure 4-2a). The predefined discretization length divides each fracture into equal length segments and each segment end represents an insertion point. To avoid fracture overlaps, a fracture can only be added to an insertion point, which is on a fracture from the other fracture set.
- Second, the length of the inserted fracture is determined (Figure 4-2b). Each insertion point has a maximum insertable fracture length to avoid overlaps. This is reflected by drawing the fracture length from a truncated FLD.
- The third step is to find the position of the intersection between the new fracture and the insertion point (Figure 4-2c). The possible positions are constrained by the length of the fracture and also other fractures above and below the inserted fracture from the same set.

Fracture deletion is the so-called death move of the rjMCMC algorithm, when the problem dimensionality is reduced. Before random deletion, the fractures that can be deleted are identified (Figure 4-2d).

- A fracture cannot be deleted if its deletion would disconnect the sources and receivers of the tomographic experiment in the model, as the forward model can only be executed if all sources and receivers are connected.
- A fracture cannot be deleted if it is not intersecting with any other fractures. Otherwise the reversibility of the algorithm would be violated, as the deleted fracture could not be added back again. An irreversible update could not be evaluated by the rjMCMC algorithm.
- The fractures connecting the source and receiver points to the rest of the DFN are permanent. They cannot be deleted or shifted shifted in order to keep the fracture

network connected. The properties of these fractures are considered to be known from borehole measurements prior the tomographic experiment.

Fracture shift is the third possible update. A deletable fracture is shifted along one of its intersecting fractures until the closest free insertion points. The technical implementation of this update is the combination of the earlier two: first deletion and then the insertion of the fracture at another position.

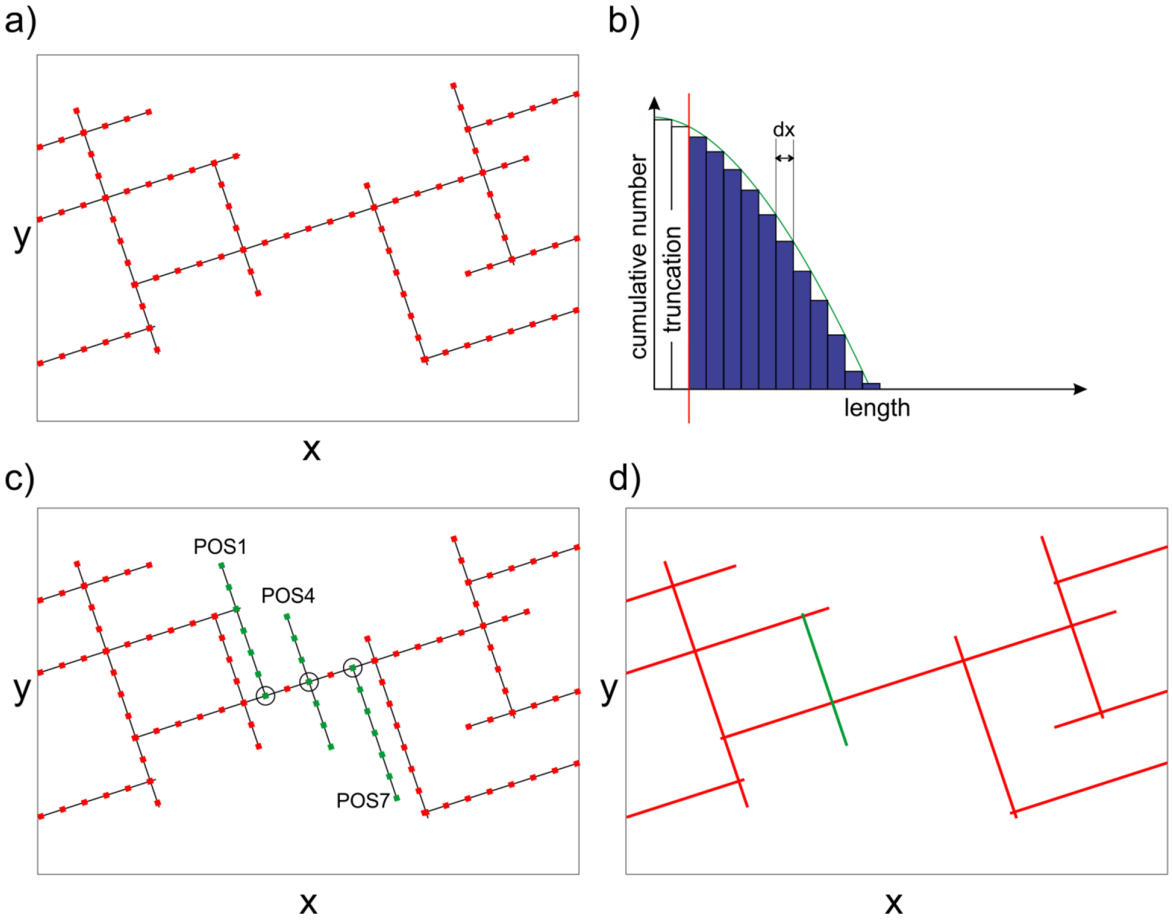

Figure 4-2. Different update steps of DFN reconstruction. a) Fracture addition: identify possible insertion points. b) Fracture addition: draw fracture length from the discretized fracture length distribution (dx: discretization length). c) Fracture addition: draw the position of the insertion point on the inserted fracture. d) Fracture deletion: identify deletable fractures (red: non-deletable, green: deletable).

The type of update is randomly selected according to initially defined probabilities. These probabilities do not have to be constant, but they can change from iteration to iteration. If the fracture intensity reaches a minimum limit, the fracture deletion update is disabled. If it reaches a maximum limit, the fracture addition update is disabled. These limits assure that the

fracture intensities of the solutions stay close to the pre-defined value. After an update, the tomographic experiment is simulated with the proposed new DFN realization, *r*'.

The misfit between the simulations and the observations is calculated to characterize the "goodness" of a DFN realization. Different misfits can be used regarding the type of the experiments and the data quality. In this study, the misfit is oriented at the root mean squared (RMS) error between the simulated and the observed measurements for the same source-receiver combination. It is also possible to use moments or breakthrough times for comparison instead of the full curve in this step. This could be advantageous when the quality of the breakthrough curves is poor or the flow field is altered by the used tracer (e.g. density effects (Somogyvári et al., 2016)).

The rjMCMC evaluates the proposed DFN realization using the Metropolis Hastings Green (MHG) acceptance criterion (Green, 1995). The MHG criterion, $\alpha(r'|r)$, combines the evolution of the misfit with the statistical properties of the proposed update:

$$\alpha(r'|r) = \min[1, prior\ ratio \times likelihood\ ratio \times proposal\ ratio \times Jacobian] \tag{4-2}$$

$$\alpha(r|r') = \min\left[1, \frac{p(r')}{p(r)} \times \frac{p(\xi|r')}{p(\xi|r)} \times \frac{q(r|r')}{q(r'|r)} \times |J|\right] \tag{4-3}$$

where r is the i-th realization, r' is the updated realization (proposal), $p(r)$ is the PDF of the prior, $p(\xi|r)$ is the likelihood function, $q(r'|r)$ is the proposal probability and J is the Jacobian.

The MHG criterion makes it possible to compare realizations with different numbers of parameters by not only comparing the likelihoods, but also the reversible updates. The likelihood function of a simulated measurement quantifies the probability of the observations given a realization of parameters. Since the noise of the measurements typically follows a normal distribution, the likelihood function reads as a Gaussian function:

$$p(\xi|r) = \frac{1}{\sqrt{4\pi\sigma^2}} \exp\left(-\frac{\left(\xi - \xi(r)\right)^2}{2\sigma^2}\right) \tag{4-4}$$

which is equivalent to using a RMS misfit (Aster et al., 2013). The variance of the simulated data noise (σ^2) defines the acceptance rate of the rjMCMC algorithm. The variance of the likelihood function is set as the noise of the observations (Gelman et al., 2004; Geyer, 2011).

The proposal ratio is the ratio between the probability of the reverse step ($q(r|r')$) and the forward step ($q(r'|r)$). The updates have to be reversible; otherwise the reverse step probability cannot be calculated. The proposal ratio makes it possible to compare realizations with different parametrization, by defining the transient step probabilities between them.

Each proposal probability is built up from the probabilities of the substeps of the used update (see Figure 4-2). For fracture addition, the proposal probability can be expressed as:

$$P(addition) = P\left(insertion_{point}\right) \times P(length|points) \times P\left(position \,\middle|\, length \,\&\, points\right) \tag{4-5}$$

$$P(addition) = \frac{1}{count(points)} \times FLD_{truncated} \times \frac{1}{possible\ positions} \tag{4-6}$$

First, the probability of selecting one insertion point is calculated from the total number of possible insertion points. Then the probability of the drawn injection length is calculated from the FLD and truncated to the fracture length limits at the given insertion points. Finally, the probability of the fracture positioning is calculated as well (also limited by the DFN). The reverse update of the fracture addition is the fracture deletion:

$$P(deletion) = \frac{1}{count\left(deleteable_{fractures}\right)} \tag{4-7}$$

The probability of fracture deletion is calculated from the number of deletable fractures in the realization. In the case of a fracture shift, the proposal ratio is 1. Regarding the prior ratio of the MHG criterion, only non-informative priors are used for the updates in this study (e.g. FLD). These priors are considered within the proposal ratio calculation and thus the prior ratio is always one (Aster et al., 2013).

For the evaluation of the MHG ratio (α), a random number β is drawn from a uniform distribution between 0 and 1. The proposal is accepted if $\beta \leq \alpha$ and rejected if $\beta > \alpha$. Accepted realizations are stored, and together serve as the result ensemble. The new iteration is started with the last accepted DFN realization. Rejected realizations are discarded.

4.2.4 Implementation

The used initial DFN solution is generated randomly based on the given statistical parameters (FLD, spacing, fracture intensity) and it needs to connect sources and receivers. In order to reach this, a very dense DFN is generated by repeated additions until the domain is

completely filled with fractures (when no free insertion points exist). From this point, randomly selected fractures are chosen and deleted when the two wells remain connected. This is continued until the desired fracture intensity value is reached. To maintain a homogeneous distribution of fractures over the whole domain, the fracture intensity is calculated over smaller subareas by dividing the domain into quadrants and further if needed. This homogeneity is important, because prior the calibration we consider the given value of fracture intensity valid over the whole investigated domain. The obtained realization is the initial solution for the inversion procedure (Figure 4-1).

The convergence rate of the algorithm depends on the chosen variance value of the likelihood function. If this value was set too low, the process does not converge. In this case, the algorithm does not accept any update when the misfit would increase. This would trap the algorithm in the first reached local minimum of the inverse problem (Aster et al., 2013). The optimal value of likelihood variance is case specific; a good choice is to use the variance value of the measurements, which is a common solution for conventional Markov chain applications (Gelman et al., 2004).

The rjMCMC algorithm requires a great number of iterations in order to map the posterior of the inverse problem properly. The convergence of Markov chains can be divided into two phases. The first phase is when the misfit is rapidly converging to zero (or to a minimal value). This is called the burn in phase (Geyer, 2011). The accepted realizations of this phase are not stored because they are strongly dependent on the used initial DFN realization. In the second phase, the misfits of the accepted realizations converge with small fluctuations around a stable value. Ideally, samples from this second phase serve as equally probable solutions to the inverse problem. The sequentially produced realizations have small differences because every accepted iteration has been created by one update. To properly map the posterior probability of the inverse problem with these small steps, a large number of samples is required (typically over 10,000 accepted realizations).

The computational time of each iteration is dominated by the computational time for the forward model. Clearly, consideration of further processes such as matrix diffusion would increase the computational burden. Even if our forward model is fast and allows flexible adjustment of fracture geometries, alternative implementations such as mesh-free fracture models appear well suited (Noetinger et al., 2016). The calculation speed of the forward model used here correlates with the number of fractures. Forward models with a large number of fractures would reduce the computational efficiency. This is modulated by

truncation of the FLD, and thus by avoiding small hydraulically inactive fractures. The other time consuming process is to identify which fracture can be deleted without splitting the connection between the source-receiver points. This requires repeated connection tests after deleting one by one all the fractures within the DFN. We improved this process by parallelizing it to multiple threads (according to the used CPU architecture).

4.3 Test cases

Two example cases are investigated with the presented DFN inversion. The fracture network of the first case is a hypothetical variant with simple geometry. The second synthetic geometry is created based on an outcrop field data. With both fracture networks, tracer tomography experiments are simulated and the fracture network geometry in the vertical cross-section between source and receiver well is reconstructed.

4.3.1 Simple hypothetical case

In this case, two wells on the left and right model boundaries are connected by one main fracture (Figure 4-3a). It belongs to the first of two fracture sets, with inclinations of 10° and 110°, and apertures of 3 and 2 mm, respectively. In each of the wells, three source- or receiver-points are connected to the aquifer via fixed fractures that belong to the same set as the main fracture of the model. Keeping these fractures fixed assumes that they have been localized and described through preliminary borehole geophysical investigation. An initially uniform pressure of 200 kPa is applied to the model domain. In order to duplicate the recorded data, each well serves for injection and observation. An injection pressure of 300 kPa is assigned to the injection interval of the one well, and the pressure of the other production well is set to 100 kPa. The simulation of tracer transport starts only after the steady state flow field is established. Tracer concentrations in the fractures are initially zero. Continuous tracer injection is started at time t = 0 using a 20 mg/l solution of an ideal conservative tracer. The tracer injection is maintained until the end of the experiment. The end of the experiment is set where complete breakthroughs are detected in every observation point (except where no breakthrough occurred). The used experimental time was 200 s and concentrations were measured every 10 s. Here, 10 % Gaussian noise is added to the simulated observations to represent measurement noise. The dispersion coefficient for the tracer is D = 0.6 m^2s^{-1}. Every injection is simulated as an independent experiment, starting from a tracer-free state. In practice, however, this could be performed as a multi-tracer

experiment with simultaneous injections of different types of tracers (e.g. Jiménez et al., (2016)).

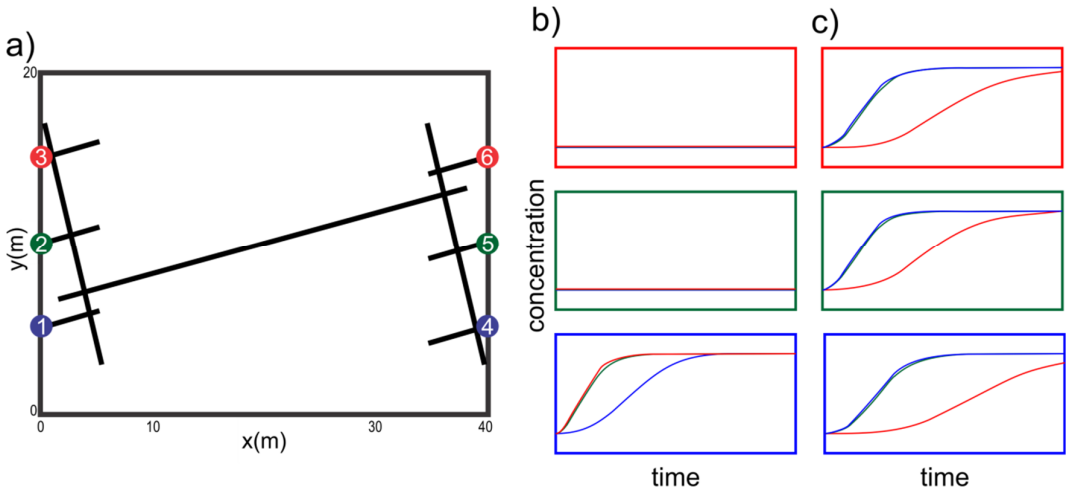

Figure 4-3. a) Synthetic fracture network model. Injection and observation points are marked as numbered and colored dots. b) Tracer breakthrough curves (normalized by injection rate) for tomography to the right direction (left well: injections, right well: observations). The color of the frame matches with the injection point color, while the color of the curves matches with the observation point color. c) Tracer breakthrough curves of the opposing experiment.

4.3.2 Outcrop-based case

In addition to the simple hypothetical case, flow and transport in a mapped fracture network is simulated. It stems from the Tschingelmad outcrop from the upper Aar valley in the Grimsel region of the Central Alps, Switzerland (for detailed geological description of the fractured rocks in the area see Ziegler et al., (2013) and Ziegler et al., (2014)) (Figure 4-4a). The fractured system is hosted in the granite rocks of the central Aar Massif. A 50 m x 50 m outcrop surface area is selected, where the identified fractures form two loosely connected zones. Two fracture sets are identified based on the distribution of their inclinations, and different apertures of 1.5 and 0.5 mm are assigned according to typical values reported from the Grimsel region (Bossart and Mazurek, 1991). The FLD of the fracture network roughly follows the expected power law (Torabi and Berg, 2011), which is truncated and fractures smaller than 1 m are ignored in the model (Figure 4-4c). Equivalent to the hypothetical case, three sources and three receiver points are used, located at the right and left edge of the domain at known fracture ends. The same initial and boundary conditions are used as in the previous case, but the experiment is only performed in one direction without swapping the injection and observation well, which is considered to be a more realistic scenario (Djibrilla Saley et al., 2016; Doro et al., 2015; Jiménez et al., 2016). The experimental time was set to

2000 s and the concentrations were measured every 20 s. Given the longer time of the experiment, much more data points are collected than in the hypothetical case.

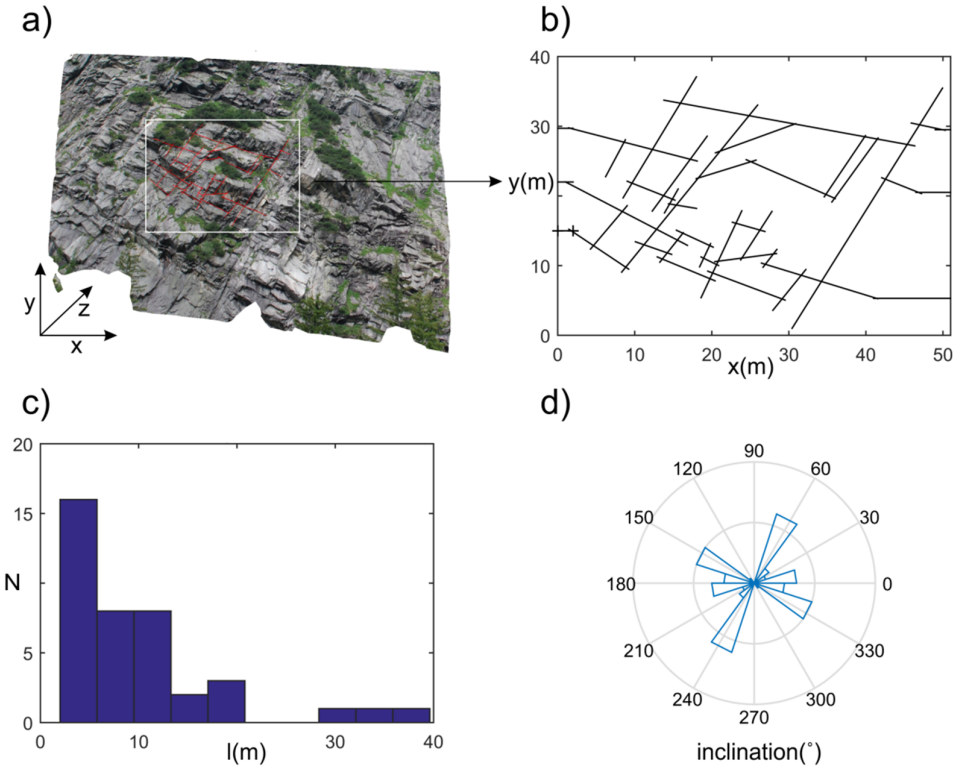

Figure 4-4. Outcrop-based model a) 3-D surface model of the Tschingelmad outcrop, b) identified 2-D DFN geometry, c) fracture length distribution of DFN (N: cumulative number, l: fracture length), d) fracture angle distribution of DFN.

4.4 Result processing

4.4.1 Ensemble size

The termination criteria of transdimensional Markov chain algorithms is an open question because convergence diagnostic techniques used in conventional MCMC simulations are not applicable for transdimensional cases (Bodin and Sambridge, 2009). Our solution to overcome this problem is based on the suggestions of Gelman et al., (2004). They check the distribution of the parameter vector in the ensemble and if it is not converged to a common distribution, they continue the inversion until the length of the Markov chain is doubled. Our approach is conceptually similar, but without the possibility to examine parameter distributions, we investigated if the result (fracture probability map and multidimensional

scaling) shows any major changes (changes in the dominant transport pathways) if the chain length is extended (double the size of the ensemble). If the two results are similar, this means that the posterior of the inverse problem is already sampled by the first part of the sequence and latter sequence parts are just sampling from the same realizations again. If the two results are different, the inversion is continued and the same conditions are checked with a longer sequence.

DFN realizations from the beginning of the chain are considered part of the burn-in phase. The endpoint of the burn-in phase is identified after the visual inspection of the evolution of the misfits, where the values are converged (Jiménez et al., 2016). To minimize the influence from the burn-in phase, the length of the discarded sequence is doubled.

The DFN inversion produces a large number (more than 10,000) of DFN realizations, which is called ensemble. Instead of a complete presentation of all of the realizations, we concentrate on the statistical information from the ensemble. In the realizations, each fracture is represented by three inverted parameters (two coordinates and the length), the models contain hundreds of fractures, and the number of fractures can vary. Therefore, individual analysis of inverted parameters is not done here, but two different ways to visualize the full ensemble results are suggested in the following.

4.4.2 Fracture probability map

The most straightforward way of result visualization is to plot exemplary DFN realizations from the ensemble. This can be misleading, since many fractures in the realizations are not used for tracer transport, and they appear as relics without influence on the inversion. The fractures where transport takes place are the hydraulically active fractures, and the inversion process is only sensitive to their positions, but not to those of the rest. The active fractures of a DFN realization are those where changes in the tracer concentration is measureable during the simulation. In order to visualize the results of an ensemble of realizations, a map showing the probability of hydraulically active fractures is chosen. This fracture probability map is generated by stacking many DFN realizations together, ideally all results from the ensemble. However, due to the large ensemble size and huge number of parameters, with many similar realizations, a subset is used to represent the mapped posterior distribution. This sample is generated by keeping only every k-th realization of the ensemble, which is known as sequence thinning (Gelman et al., 2004). Local probabilities are calculated after rasterizing

each realization and computing the frequency with which a fracture is found in each pixel in the ensemble.

4.4.3 Multidimensional scaling

Instead of local fracture probabilities, a clustering technique is used to discriminate among characteristic DFN geometries identified in the results ensemble. This is accomplished by multidimensional scaling (MDS), which visualizes similarities and differences among DFN realizations by projecting their relative distances into a Euclidian space (Borg and Groenen, 2005). For this, the DFN realizations are rasterized similarly as for calculation of fracture probability maps. Then these rasterized realizations are compared to each other in pairs, cell-by-cell, to calculate the relative differences among them. We call these differences realization distances. All the calculated DFN realization distances are stored in one distance matrix, where matrix element (i,j) is the distance between the i-th and the j-th realization. The distance matrix stores the relation between all the investigated DFN realizations.

As the distances among the realizations are relative measurements rather than absolute indicators of fracture geometry, they can only be visualized directly in a multidimensional space. The MDS method is designed to project these multidimensional point clouds into an N-dimensional space, with minimal distortion on the distances between the points (Caers et al., 2010). We use the classical MDS technique to project the distance matrix to a 2-D Euclidian plane. The distance matrix does not contain any absolute location of the samples, just their relative position to each other. Thus, the axes of the MDS projected point cloud does not contain any relevant information, and the projection only shows the relations among the different realizations. The point cloud can be used for clustering in order to identify representative DFN realizations within the ensemble with significant differences. Alternatively, to choose a representative realization, fracture probability maps can also visualize the subset of realizations within a cluster.

4.5 Results

4.5.1 Hypothetical case

Figure 4-3b-c shows the tracer breakthrough curves (BTCs) simulated with the forward model of the simple hypothetical DFN depicted in Figure 4-3a. The assigned noise is not shown in the figures. The differences in the BTCs reflect the assumed anisotropy of the DFN,

with smaller apertures of the high inclination fractures. The two upper injections from the left side did not produce any breakthroughs at the observation points. Observations where no breakthrough occurs frequently appear in the results of tomographic tracer tests, but they are often ignored in the inversion (Brauchler et al., 2013a; Somogyvári et al., 2016; Vasco and Datta-Gupta, 1999). If no breakthrough is observed within the simulated time, it is concluded that there is no (relevant) advective pathway leading from one point to the other. However, such findings are just as valuable as when tracer concentrations are measured and hence are also considered for misfit calculation here. The other four injections show very similar breakthrough behavior, with more spreading of those associated with longer travel times.

The used control parameters for the inversion procedure are summed up in Table 4-1a. Note that the configuration of the inversion procedure does not allow for the exact reconstruction of the original DFN geometry. This geometry shown in Figure 4-3a is considered the hydraulically active part of a greater fracture network, which is expected to have a higher fracture intensity (0.7) with several inactive fractures that cannot be identified. Also, a different FLD is used for the inversion which is chosen according to the scale of the experiment (Torabi and Berg, 2011). The used FLD follows a normal distribution with zero mean and variance of 25 m^2. The discretization length of the DFNs is selected as 0.5 m. This level of discretization is capable of representing a DFN with the chosen parameters (FLD, fracture intensity), while keeping the simulation time of a tomographic experiment within a few seconds. The collected ensemble size was 30,000 realizations and the calculation took 48 hours on an office PC (Intel® Core™ i7-6700k 4 x 4.0 GHz). An additional crosscheck with a doubled rjMCMC chain length (60,000) gave similar results, meaning that the smaller size is sufficiently large according to the given termination criteria.

Table 4-1. Parameters of the inverse modelling

	a) Simple model		**b) Field-based model**	
Fracture set	**Set 1**	**Set 2**	**Set 1**	**Set 2**
Fracture inclination (°)	10	110	-12	58.9
Fracture aperture (mm)	0.3	0.2	0.15	0.1
Discretization length (m)	0.5		0.5	
Fracture intensity	0.7		0.4	
FLD – variance (m^2)	25		72.25	
Likelihood variance	1.5		1.5	
P_{add} /P_{del} / P_{shift}	0.4 / 0.4 / 0.2		0.4 / 0.4 / 0.2	

The first few hundred accepted realizations in the sequence show a rapid decrease in the misfit (Figure 4-5a). This phase is the burn-in period where the realizations are still influenced by the used initial solution. This decrease stops after the first 1,000 iterations. To completely eliminate the influence of this initial phase, the ensemble was built after the 2,000th accepted realization. The evolution of the misfits of the individual breakthrough curves (BTC) is presented in Figure 4-5b, normalized by the injection concentration of the tracer. The burn-in period serves as the adjustment of the concentration curves with very high initial misfits. After the initial period, misfits stabilize and fluctuate around small values. Often when there is an increase in RMS error at one BTC, this is compensated by a decrease at another.

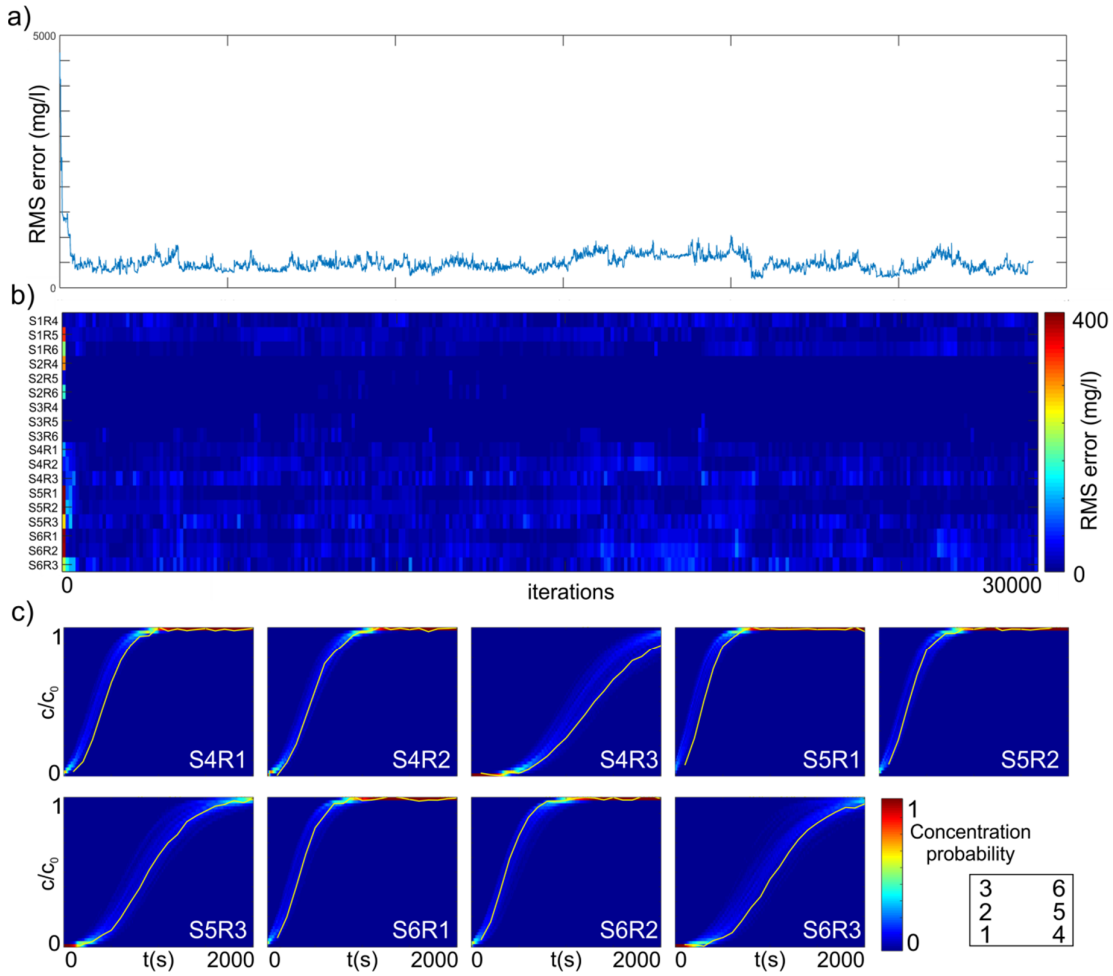

Figure 4-5. Inversion quality assessment. a) RMS error of the accepted realizations through the Markov chain sequence. b) Evolution of the misfits on the simulated breakthrough curves. c) Fit quality of breakthrough curves of the second half of the experiment (reverse direction) in the whole ensemble (breakthrough probability maps). "S#" represents the source number, "R#" denotes the observation point (receiver) number, according to the source receiver configuration shown in the bottom right corner.

For further result analysis, the Markov chain is thinned to 300 realizations. The quality of the individual fits on the BTCs is presented in Figure 4-5c. This figure serves as a first visual validation of the inversion results. “S#” represents the source number in the figures and “R#” denotes the observation points, according to the source receiver configuration shown in the bottom right corner. These breakthrough probability maps are generated similarly to the fracture probability map; rasterized BTCs are stacked together pixel-by-pixel. Fast BTCs show very good fits, while slower ones are slightly offset. Source-receiver combinations where no breakthrough was observed show perfect fits (see supplementary figure S4-1). This is because realizations where this is not reproduced, provide very high misfits and they get rejected immediately.

Figure 4-6 depicts the fracture probability map created from the result ensemble. The geometry of the hydraulically active fractures can be read from the high probability locations of the fracture probability map. As the most striking feature, the location of the main connecting fracture can be determined from the map: a high probability stripe connects the two wells. The most probable endpoints of this channel are located at the same locations relative to the sources and receivers as in the original model. The probability of the fractures connecting the source and receiver points with the aquifer is always 100% because they are kept fixed and not subject to inversion. The location of the two high-inclination fractures that connect these source-receiver fractures vertically is also visible in Figure 4-6 with high probability values. An additional low inclination fracture is proposed on the left side of the map between the upper two injection (or detection) points. The inversion is less sensitive to this area, probably because the two injection points nearby produced no breakthroughs. A large number of falsely identified fractures exist in the central area of the profile. Most of these fractures belong to the high-inclination fracture set 2. As this fracture set is less relevant for cross-well transport, it is more likely that some of such fractures freeze in and remain in many result realizations without any impact on the inversion. The additional low-inclination low-probability fractures provide alternative pathways to the transport in different realizations, results in equivalent BTCs. In order to run the inversion properly, higher fracture intensity was chosen than the synthetic reference, this is why many additional fractures exist within the individual DFN realizations. Most of these fractures are hydraulically inactive, and may disappear due to the updates (thus have small probability in the fracture probability map). However they cannot be discarded during the inversion, as they provide possibilities for fracture addition and can become active in later iterations.

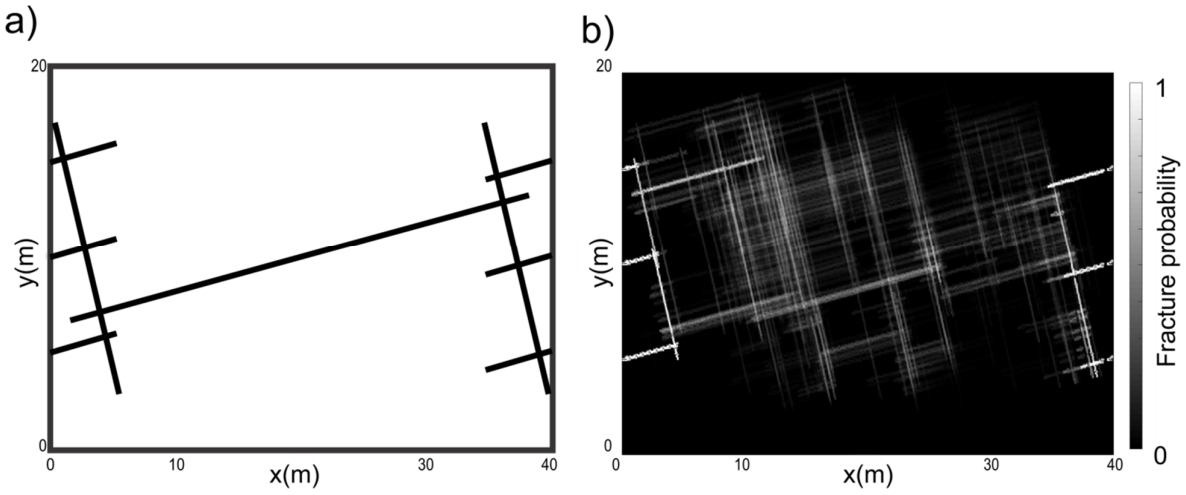

Figure 4-6. Inversion results of the synthetic scenario. a) Synthetic fracture network model b) Inverted fracture probability map generated from 300 DFN realizations.

To separate the main DFN realization types within the ensemble, MDS is applied (Figure 4-7). The projection of the point cloud shows a nearly symmetric shape. Note that the circular shape is the result of the projection that tries to minimize distortions in the sample distances and has no further significance here. We highlighted four different clusters of the MDS map (Figure 4-7a), originating from different phases of the inversion process (Figure 4-7b). Figure 4-7c shows the differences between the clusters by presenting the hydraulically active fractures from example realizations. The evolution of the different (but equally probable) DFN realizations can be seen by going through the clusters. The example of the first cluster is the most focused fracture network, with one choke-point on the right. This choke point remains in the second cluster, but the network to the left of it gets more spread. This spread continues in the next two clusters, reaching the right side of the domain as well. Yet in the fourth cluster, the fracture density in the center gets lower, making it somewhat more similar to the first cluster.

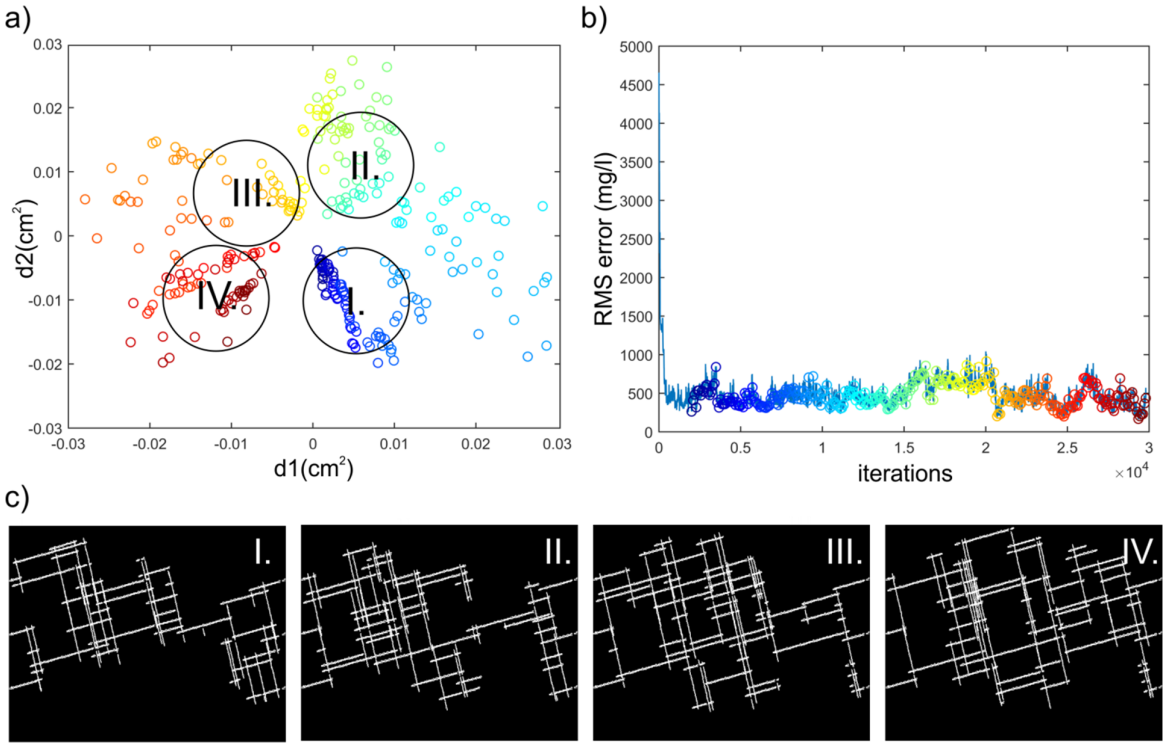

Figure 4-7. Ensemble visualization using MDS mapping (synthetic case) with the 300 selected realizations after sequence thinning. d1 and d2 are the virtual dimensions of the MDS projection. a) MDS map and identified clusters b) Convergence of the inversion with selected realizations c) DFN examples from the identified clusters.

In Figure 4-7a, the colors of the points show that each cluster is built up from consecutive realizations. Ideally, after a large number of iterations, DFN realizations from the same clusters would not only contain samples from the same stage of convergence. This is because after many iterations, the points would start to mix on the MDS map as the inversion explores solutions again that have been reached earlier in the chain. Although the latest realizations started to become similar to the first ones in our sequence, further analysis of the longer (doubled) sequence showed that in fact no mixing had started to develop yet.

It is interesting to compare the example realizations (Figure 4-7c) of the clusters to the final fracture probability map (Figure 4-7a). It is obvious that these realizations contain information of the final result, but none of them is capable of representing the original fracture network alone. No big difference in the BTCs of the different clusters is visible, since the fit of the BTCs show minimal variance throughout the full ensemble (see Figure 4-5c). The variations in the misfit values are mainly caused by the slowest breakthrough curves, which are most affected by the differences between them, while the quickest transport routes are constant.

Changes in the geometry which modify the fastest transport pathways would alter multiple breakthroughs at the same time. This type of changes drives the burn-in period of the rjMCMC sequence, where the general transport pattern is adjusted to the observations. In the converged phase of the algorithm, these updates are rare, as they only get accepted if they do not make a very large increase in the misfits. This explains why the fracture probability map shows only one main transport pathway and not multiple different ones.

Due to the highly discretized behavior, the risk of the algorithm to become trapped in a local minimum is higher than in rjMCMC studies developed to interpret continuous problems (e.g. Bodin and Sambridge, 2009; Jiménez et al., 2016). The discrete geometry strongly limits the freedom of updates since, as always, a limited number of possible updates is available. Using higher likelihood variance, the inversion can escape from most of the local minimums, but posteriors with highly bi- or multimodal behavior could require multiple model runs for complete sampling. In the presented scenarios, the inversion always converged to similar solutions, independent from the initial realization.

4.5.2 Outcrop based case

In the following, we present the results for the more complex outcrop-based fracture network (Figure 4-4). The statistical properties of the outcrop (Figure 4-4b-d) are taken to configure the search procedure (Table 4-1b). The fracture intensity of the middle part of the outcrop is used for the inversion (0.4). A truncated normal distribution is determined to approximate the FLD of the network, with the smallest allowed fracture size of 1 m. With 0 m mean and 72.25 m^2 variance, this approximates the distribution of the smaller fractures in the investigated fracture network well. Very long fractures are only expected to be drawn as outliers from the used FLD. Thus, very long fractures of the outcrop should be mainly built up by shorter segments in the generated DFN realizations. The discretization length of the DFNs is 0.5 m. The inclinations of the fracture sets in the inverse model are defined after inspecting the fracture inclination distribution of the outcrop shown on Figure 4-4d, where two dominant fracture inclinations exist. The two used inclinations are -12˚ and 59˚, respectively. Note that due to this restriction, as well as due to the approximate settings for fracture intensity and FLD, the investigated DFN geometry can only be approximated by the inversion and not exactly reproduced.

Again, similar to the hypothetical case, 30,000 realizations were collected for the ensemble and 2,000 realizations were discarded as burn-in phase (Figure 4-8a). The converged RMS

error values are higher than in the hypothetical case, because the experimental times were longer and the BTCs consisted of (five times) more data points. As a consequence, the misfit values of the individual BTCs are higher for this case (Figures 4-8b,c). At early breakthroughs (e.g. S1R4 or S2R4), the reconstructed breakthroughs are late. In comparison, latter breakthroughs show good fits except of S1R5. This one is the latest among all the BTCs, and it also shows the weakest fit (200s late) with the largest variance. The used misfit criterion is most sensitive to the elongated BTCs, where the increase in concentration spans through the whole time interval (e.g. S1R6, S2R5). Thus, elongated BTCs are the main drivers of the inversion procedure. For example, comparing S2R6 to S3R5, the fit of S3R5 is better (Figure 4-8c) but the misfits are in the same range (Figure 4-8b).

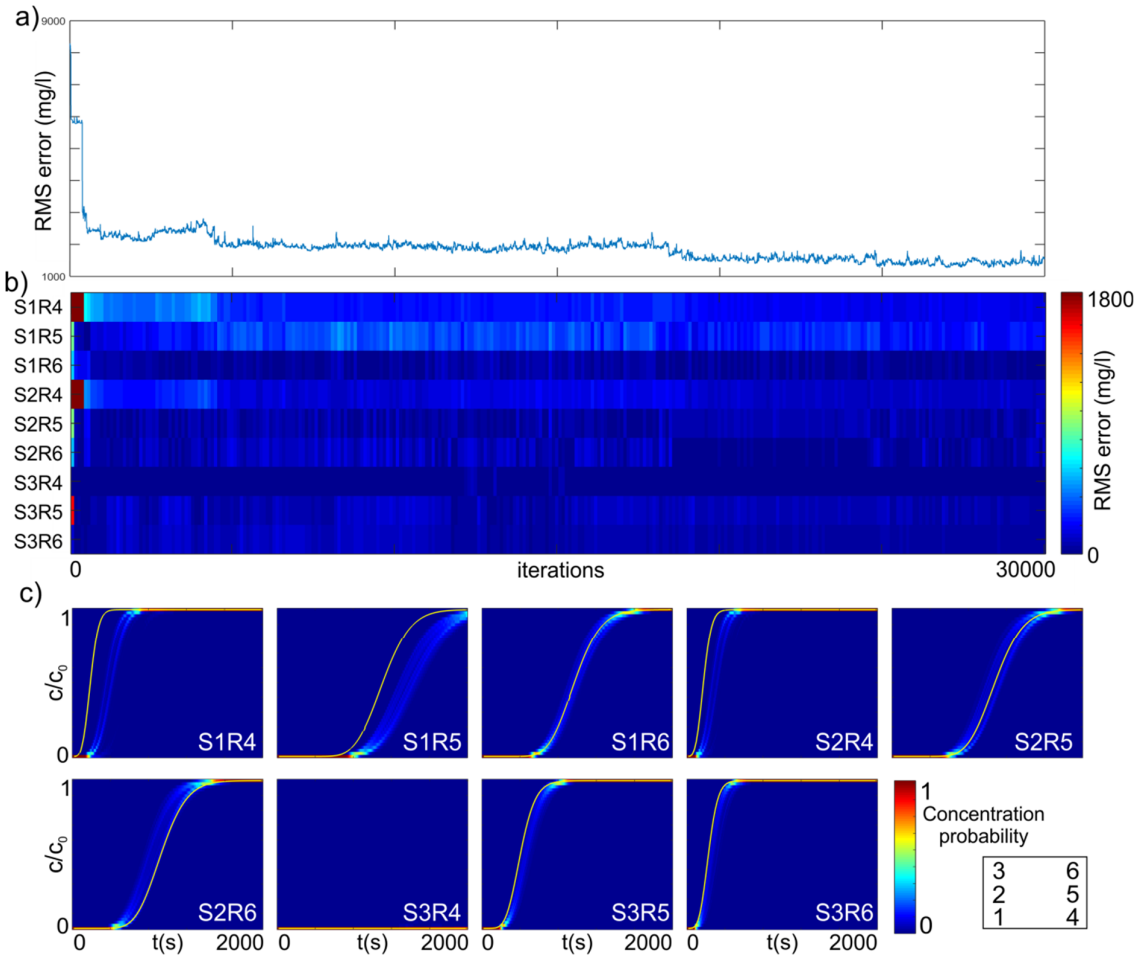

Figure 4-8. Inversion quality assessment of the outcrop based scenario. a) RMS error of the accepted realizations through the Markov chain sequence. b) Evolution of the misfits on the simulated BTCs. c) Fit quality of breakthrough curves in the whole ensemble (breakthrough probability maps). "S#" represents the source number, "R#" denotes the observation point (receiver) number, according to the source receiver configuration shown in the bottom right corner.

The DFN results of the inversion are shown by Figure 4-9. A main feature of the original fracture network is that it is split into two loosely connected fractured areas, an upper and a lower one. This is visible also in the fracture probability map (Figure 4-9b). Some non-fractured areas of the domain are well reproduced and the strongly fractured area in the bottom left quarter of the original domain is recognizable in the fracture probability map. Overall, the main transport pathways are easy to identify from Figure 4-9b, but the individual fractures often appear multiplied. A closer look reveals that fracture set 2 consists of multiple doubled fractures, while fracture set 1 has multiple quadrupled fractures. This is the effect of discretization and limited sensitivity of slightly shifted fractures that cause minor change in the BTCs. In studies using continuous models, the same effect appears as the smoothness of the final result (Bodin and Sambridge, 2009; Jiménez et al., 2016).

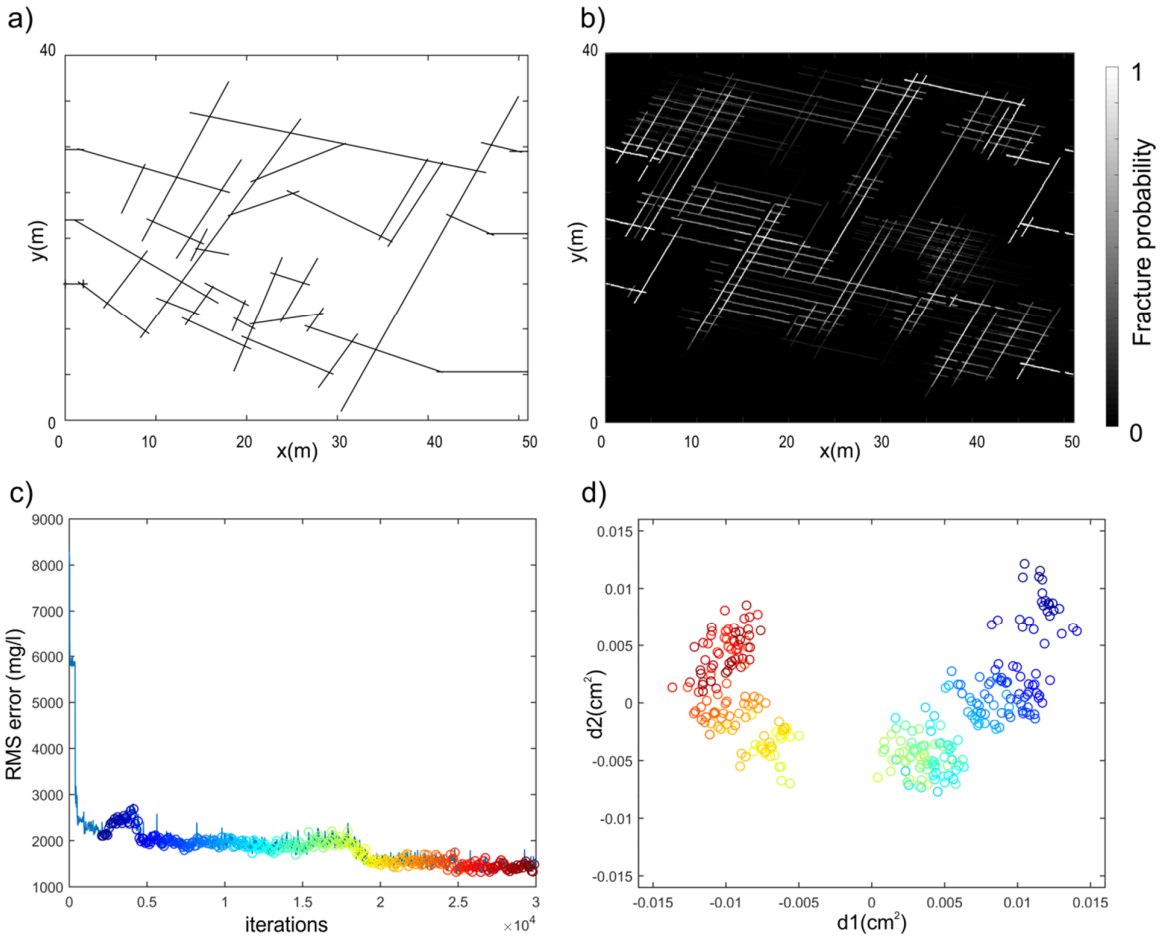

Figure 4-9. Inversion results of the outcrop-based scenario. a) Outcrop based fracture network model b) Fracture probability map of the reconstruction c) Convergence rate of rjMCMC (with the selected samples marked) d) MDS mapping of the ensemble subset.

The used discretization length was chosen to support fast computations. Since the value of 0.5 m is larger than the smallest fracture spacing in the outcrop and the distance of the two wells are 50 m, it is considered small enough for the DFN reconstruction. It is also smaller than the shortest mapped fractures of the investigated fracture network. Under field conditions, the discretization level can be chosen based on the observed spacing of the fractures. Using a small discretization length improves the resolution of the reconstruction and it improves the fracture length estimation since the used FLD is also discrete. However, the associated increase in degrees of freedom for fracture calibration means higher computation times and hampers discrete identification of fractures. Coarser discretization levels may cause a neglect of relevant small scale features and could strongly limit the number of possible solutions delivered by the inversion. Long fractures are more likely to be reconstructed, but with less accurate fracture length estimation.

The MDS map (Figure 4-9d) shows that the differences between the DFN realizations are significantly smaller than in the hypothetical case. This means that the realizations are more similar to each other and the solution provides less equivalent tracer pathways than the hypothetical case. The point cloud is more mixed even though it shows a general clockwise trend, but the points do not follow each other sequentially. This could be an indicator on the completeness of the sampling, but also can be an effect of the small differences in the DFN geometries.

4.6 Conclusions

Fracture systems in hard rocks are commonly described by statistical information on orientation, spacing and intensity of fracture sets. This information is used to generate candidates of discrete fracture networks (DFNs) that describe the hydrogeological conditions in the field. There is still a lack of techniques that allow flexible calibration of DFNs to data from spatially resolved field measurements, which were obtained from geophysical, hydrogeophysical or hydrogeological investigations. A main hurdle is the often large number of tuning parameters which is tied to the number of fractures used in the model. The number of fractures, however, is not known a priori. This is tackled in this study by introducing a transdimensional inversion procedure (rjMCMC) that adjusts geometrical values and fracture numbers during the calibration. By processing both the statistical description of the fractured rock and data from field experiments, a new concept of DFN model calibration is developed.

The presented implementation of rjMCMC automatically develops a connected fracture network by sequentially creating, deleting and moving fracture segments in space. Its potential is evaluated with a simple synthetic and a field-derived fracture network, which are both reconstructed based on conservative tracer tomography experiments. As a result, an ensemble of DFN realizations is obtained that reveals highly probable locations of those fractures relevant for tracer transport. We introduced fracture probability maps, extracted from the ensemble representative realizations based on clustering and multi-dimensional scaling. These results can also be exploited for case-specific production probability assessment or risk assessment.

By comparison to the original DFNs, it was demonstrated that major geometrical features could be identified. It is also revealed that often equally probable geometries exist and adjacent fractures yield similar results. Accordingly, small-scale variations could not be resolved. Ideally local high fracture intensities appear in the fracture probability map as densely spaced active fractures with high probabilities. The main control parameter for the obtained fracture resolution is the discretization, the role of which needs to be further explored in sensitivity analyses. A logical next step is to include additional data from complementary field tests, such as from near-surface geophysics which could reduce the non-unique behavior of the results. As the presented Bayesian inversion framework allows joint consideration of different types of data, DFN reconstruction could be improved when compared with using only tracer data as in the presented work. There is also room for improvement by refining the misfit calculation of tracer BTCs, which is based on standard RMS error computation. For example, a weighted error calculation may be applied to adjust the significance of different source receiver combinations, or to control the importance of early, normal and late breakthroughs. Another possible option is to use selected tracer travel times instead of direct BTC comparison.

In future work, we will also consider three-dimensional DFN reconstruction and calibration of the fracture apertures. This will require a higher information density from (simulated) field experiments, or tighter constraints to localize sensitive (or active) fractures. The presented inversion framework is not limited to 2-D, but an additional dimension will raise the computational time for the forward model and it will reduce the convergence rate of the Markov chain. Note that for the presented cross-well sections, the forward model was executed in a few seconds. So even with an additional dimension, and when simulating alternative transport behavior (e.g. retardation of tracer), computation times will be in a

feasible range. Aside from this, promising advanced rjMCMC schemes (e.g. delayed rejection (Bodin and Sambridge, 2009)) and high-performance computers have not been considered yet. Computational performance may be improved by simulating shorter Markov chains in parallel and handling the results together. As with discarding realizations of the burn-in phase, the influence of the used initial solution can be minimized and sequences generated with the same control parameters may be handled together. However, during the development of the method so far, we have focused on optimization for single chain performance. In the current version the implemented algorithm runs best on high single thread performance CPUs. Involving the fracture aperture in the inversion would greatly reduce the convergence rate and increase the instability of the inverse problem. Thus inverting apertures will require additional constrains on the model parameters, or the involvement of additional data in the inversion. Although the proposed methodology is presented for conservative tracer tomography, other types of experiments, such as hydraulic tomography or alternative hydrogeophysical investigations can be interpreted.

Acknowledgements

This work was supported by the Swiss National Science Foundation under grant number 200021_149128. We Walter Illman and two anonymous reviewers for the constructive comments and Rachael Colldeweih for language corrections.

Supplementary Information

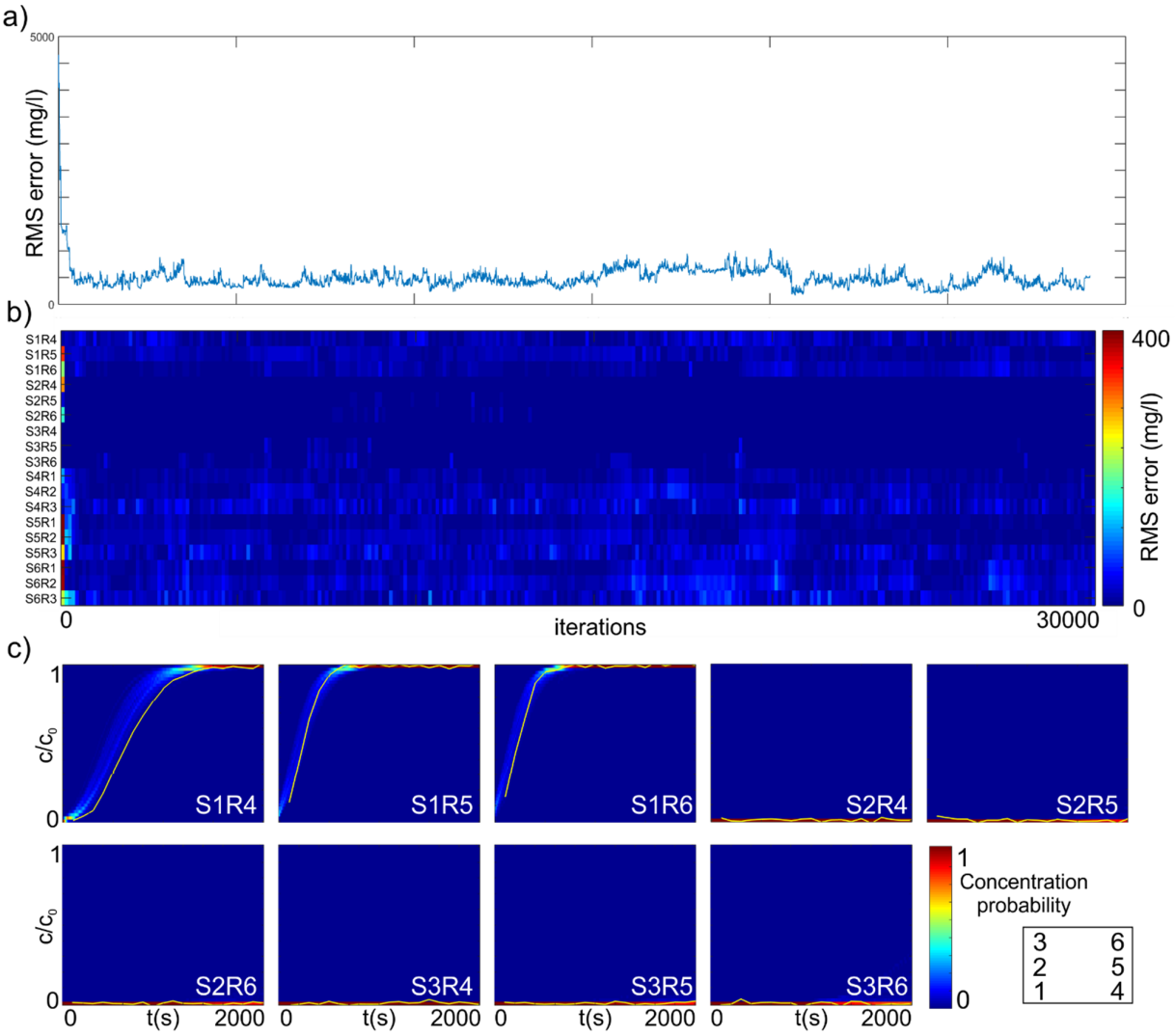

Figure S4-1. Inversion quality assessment. a) RMS error of the accepted realizations through the Markov chain sequence. b) Evolution of the misfits on the simulated breakthrough curves. c) Fit quality of breakthrough curves of the first half of the experiment (forward direction) in the whole ensemble (breakthrough probability maps). "S#" represents the source number, "R#" denotes the observation point (receiver) number, according to the source receiver configuration shown in the bottom right corner.

5 Summary and outlook

5.1 Summary

The main goal of this PhD research project was to develop robust methods to reconstruct the hydraulic heterogeneity of aquifers using tomographic thermal tracer tests. This included the design of field experiments and the development of inversion methods both for porous and fractured aquifers. In addition, techniques suitable for practical applications were investigated.

In Chapter 2 the travel-time-based thermal tracer tomography concept is presented. A tomographic setup with multi-level tracer injections and observations is implemented in a model with a 3-D high-resolution aquifer analog, and the capability of the inversion procedure to reconstruct the heterogeneous distribution of hydraulic conductivity is examined. Heat is selected as a tracer, which offers several advantages in comparison to many solute tracers, but its applicability is traditionally considered limited due to the higher diffusion and coupled thermal-hydraulic processes.

By picking early arrival times, the impacts of thermal diffusion, buoyancy, and viscosity variation are minimized and, in this way, inversion becomes almost completely insensitive to the temperature range. A key principle is that the transport in the aquifer is dominated by advection, and injection of hot water causes minor distortions in the existing flow patterns. This can be controlled, for instance, by establishing a forced gradient between injection and observation point by operating an adjacent pumping well.

The presented travel-time-based inversion is a fast and computationally efficient procedure, which delivers a result in a few minutes for a 2-D and in about an hour for a 3-D model configuration. I demonstrate that not only structures of highly conductive zones can be reconstructed, but also the values of hydraulic conductivity can be closely matched. This is appealing, keeping in mind that the presented eikonal inversion is based on a rough approximation of groundwater flow and transport by a wave equation.

Motivated by the promising results with synthetic examples, in Chapter 3 I examine the suitability of travel-time-based thermal tracer tomography to a field case. Field experiments with multiple injections of heat can be technically demanding and time-consuming. Hence, a fundamental issue was the development of a fast, simple and cost-effective test design, which would facilitate the first inversion of a thermal tracer tomogram in the field. As a test site, a heterogeneous alluvial aquifer was chosen, which was already investigated in numerous previous field campaigns. By focusing on a small, 7 m deep cross-section between two

boreholes approximately 1.20 m apart, short-term and multi-level warm water injections in the one borehole were sufficient to detect different thermal breakthroughs in the downstream observation borehole. This saved time, equipment costs, and heating devices, which would be required for more extensive continuous injections.

The chosen thermal pulse signals were employed sequentially over three days between the multi-level sources and receivers, and the recorded signals in the downgradient observation borehole indicated significant connectivity. In the experiment, forced gradient conditions were applied to establish a controlled flow regime with advection-dominated transport. This allowed a travel-time-based tomographic inversion of the tracer breakthroughs to reconstruct hydraulic aquifer heterogeneity.

The inverted tomogram is compared to findings from previous investigations at the field site and results show that similar features are captured by thermal tracer tomography. In particular, a known central low-K layer and the steep aquifer bed are successfully reconstructed on the tomogram. In addition, the magnitudes of inverted K values are consistent with those from earlier hydraulic field investigations. A low conductivity zone in the tomogram at the bottom part of the aquifer is interpreted as a sand lens or local sandy zone, which is a common feature of the gravel hosting the aquifer. This is also validated by a recent field investigation with colloid tracers.

The presented thermal tracer tomography design provides a cost-effective alternative to using other tracers, like solute tracers. Although the experimental times are longer because of the slower propagation of thermal signals, the recorded temperature breakthrough curves can be obtained real-time with highly sensitive sensors or DTS. The observed temperature breakthrough curves exhibit low noise and are thus ideal for travel time detection. The inversion of the travel time dataset is fast, and it does not require any special hardware. For investigation of greater aquifer volumes, the thermal signals need to be adjusted, either by longer injection times or by higher temperature. Here, the challenge would be finding the balance between the amount of heat per injection and the temperature recovery time of the aquifer.

This first complete aquifer characterization campaign using thermal tracer tomography confirmed, that this experimental method is suitable for aquifer heterogeneity reconstruction. I demonstrated, that the travel-time-based inversion is a fast and robust algorithm and it is applicable under a large range of conditions in porous media.

While the travel-time-based thermal tracer tomography concept shows great potential for investigating porous aquifers, the realistic reconstruction of fractured aquifers requires a different approach. Approximating fractured rock as a highly heterogeneous porous aquifer would limit the reconstruction to the preferential flowpaths or to highly fractured conditions. Discrete fracture networks (DFN), however, provide realistic representations of hard rock aquifers. Comprising an impermeable matrix and interconnected permeable fractures, these models are especially suited to simulate flow and transport in fractured media. However, there remains a lack of techniques that allow flexible calibration of DFNs to data from spatially resolved field measurements, which are obtained from geophysical, hydrogeophysical or hydrogeological investigations. A main hurdle is the number of fractures not known a priori. This is tackled in Chapter 4 by introducing a transdimensional inversion procedure (rjMCMC) that adjusts geometric values and fracture numbers during the calibration. By processing both the statistical description of the fractured rock and data from tracer tomography experiments, a new concept of DFN model calibration is developed.

The presented implementation of rjMCMC automatically develops a fracture network by sequentially creating, deleting and moving fracture segments in space. Its potential is evaluated with simple synthetic and field-derived fracture networks, which are both reconstructed based on conservative tracer tomography experiments. As a result, an ensemble of DFN realizations is obtained that reveals highly probable locations of those fractures relevant for tracer transport. I introduce fracture probability maps, extracted from the ensemble representative realizations based on clustering and multidimensional scaling. These results can also be exploited for case-specific production probability assessment or risk assessment.

By comparison to the original DFNs, it is demonstrated that major geometric features can be identified. It is also shown that often equally probable geometries exist and adjacent fractures yield similar results. Accordingly, small-scale variations could not be resolved without involving additional measurements. Ideally, local high fracture intensities appear in the fracture probability map as densely spaced active fractures with high probabilities. The main control parameter for the obtained fracture resolution is the discretization, the role of which needs to be further explored in sensitivity analyses. Although the method is demonstrated on the example of conservative tracer tomography, it is directly applicable to thermal tracer tomography data by modifying the forward model.

5.2 Outlook

5.2.1 Travel-time-based thermal tracer tomography

The presented travel-time-based thermal tracer tomography concept in Chapter 2 and 3 applies approximations that may reduce the quality of results, especially in highly heterogeneous aquifers. For instance, the calculation of the *K* field from the inverted tracer velocity distribution considers the same hydraulic gradient over the whole domain. This approximation is only valid for homogeneous media, but leads to distorted *K* values when heterogeneities exist. This may be improved by adding a sequential calibration step to the algorithm, where the distribution of gradients is adjusted to the reconstructed aquifer structure.

The used null-space energy approach is considered a representative quantification of local reconstruction reliability. However, the reconstruction quality of embedded non-permeable features is always better than similar zones close to the boundaries of the tomogram. In the first case, the transport pathways surround the low-*K* structure, while in the second they simply avoid it. This difference is not visible in the null-space energy maps. We suggest further investigations towards this direction to find more suitable methods for tomogram quality assessment.

The presented field validation showed promising results, but its small scale restricted the practical suitability of the experimental design. Increasing the scale of thermal tracer tomography requires the optimization of the pulse injection to provide a measurable signal but minimalize the temperature recovery times between the individual injections.

Several thermal tracer tests reported in the literature utilized distributed temperature measurements for monitoring, but injected the thermal tracer without isolating any borehole interval, using the complete borehole screen. An interesting direction to inspect whether these measurements are sufficient for tomographic reconstructions. Is it possible to approximate a tomographic array from a thermal tracer test with a line source? This solution would greatly increase the practical applicability of this investigation method.

5.2.2 Transdimensional DFN inversion

A logical next step of the DFN inversion is to include additional data from complementary field tests, such as from near-surface geophysics. As the presented Bayesian inversion

framework allows joint consideration of different types of data, DFN reconstruction could be improved when compared with using only tracer data as in the presented work. There is also room for improvement by refining the misfit calculation of tracer BTCs, which is based on standard RMS error computation. For example, a weighted error calculation may be applied to adjust the significance of different source-receiver combinations, or to control the importance of early, normal and late breakthroughs. Another possible option is to use selected tracer travel times instead of direct BTC comparison.

The presented DFN reconstruction method is limited to 2-D fracture network geometry reconstruction in its current state. The used rjMCMC algorithm does allow the extension to 3-D and also to estimate the fracture apertures. However, including the individual fracture apertures in the inversion would dramatically increase the freedom of the inverse problem, leading to unstable solutions. This problem may be overcome by including more observations in the inversion. As the presented approach is Bayesian this is easily possible.

Another solution is to relate the fracture apertures to the fracture length. This way the number of free parameters does not increase, and the stability of the inversion persists. This approximation is valid, as these two fracture properties are usually related (Childs et al., 2009; Kolyukhin and Torabi, 2012, 2013; Torabi and Berg, 2011) .

The reconstruction of 3-D fracture networks requires a higher information density from (simulated) field experiments, or tighter constraints to localize sensitive (or active) fractures. An additional dimension will raise the computational time for the forward model and it will reduce the convergence rate of the Markov chain. Aside from this, promising advanced rjMCMC schemes (e.g. delayed rejection (Bodin and Sambridge, 2009)) and high-performance computers have not been considered yet. Computational performance may be improved by simulating shorter Markov chains in parallel and handling the results together. As with discarding realizations of the burn-in phase, the influence of the used initial solution can be minimized and sequences generated with the same control parameters may be handled together.

To validate the proposed methodology the interpretation of a real-life dataset is the next phase of development. The joint inversion of multiple experiments is recommended, to exploit the full potential of the proposed methodology.

Acknowledgements

I would first like to thank Simon Löw for giving me the opportunity to do a PhD at the Engineering Geology group of ETH Zurich.

I also want to thank Peter Bayer for his great continuous support. This research project could not have been successful if I would not have benefited from his trust, patience and guidance. His constant help and advices helped me to find my way in academic research.

I would like to thank the supervision of Ralf Brauchler whose expertise led me into the world of tracer tomography, and of Reza Jalali who revealed the secrets of fractured networks. I can happily think back to the collaborations and discussions with Santos Jiménez, through which his (sometimes confusing) tips helped me many times to overcome difficulties. I thank Linwei Hu for helping me with the development of the inversion scripts, and Jaime Rivera for checking my mathematical derivations. I thank the great discussions with Bernard Brixel and Maria Klepikova.

I also would like to thank the great help of Mischa Schweingruber and Berrak Firat as their hard work helped to conduct the field experiments presented. I am happy to have shared an office with Peter Achtziger, who could always cheer me up with a funny joke or comment and helped me with many-many decisions. I thank Andrea Wolter for proof reading this thesis and Rachael Colldeweih for the language corrections of the research papers.

I have had the chance to work in a friendly and motivating environment, where I could count on any colleague of mine whenever I was in need for help. So I would like to thank Andrea, Benedetta, Bernie, Clément, Daniel, Fanny, Florian, Franzi, Gregoire, Hannes, Katrin, Kerry, Larissa, Lorenz, Martin, Matt, Mohammad, Molly, Reto and Sophie.

Finally, I would like to thank my dear Luca for joining me on this adventure, and my family for their continuous help and support.

References

Anderson, M. P.: Heat as a Ground Water Tracer, Ground Water, 43(6), 951–968, doi:10.1111/j.1745-6584.2005.00052.x, 2005.

Aster, R. C., Borchers, B. and Thurber, C. H.: Parameter Estimation and Inverse Problems, Elsevier., 2013.

Bakker, M., Caljé, R., Schaars, F., van der Made, K.-J. and de Haas, S.: An active heat tracer experiment to determine groundwater velocities using fiber optic cables installed with direct push equipment, Water Resour. Res., 51(4), 2760–2772, doi:10.1002/2014WR016632, 2015.

Bayer, P., Comunian, A., Höyng, D. and Mariethoz, G.: High resolution multi-facies realizations of sedimentary reservoir and aquifer analogs, Sci. Data, 2, 150033, doi:10.1038/sdata.2015.33, 2015.

Bense, V. F., Read, T., Bour, O., Le Borgne, T., Coleman, T., Krause, S., Chalari, A., Mondanos, M., Ciocca, F. and Selker, J. S.: Distributed temperature sensing as a down-hole tool in hydrogeology, Water Resour. Res., doi:10.1002/2016WR018869, 2016.

Benz, S. A., Bayer, P., Menberg, K., Jung, S. and Blum, P.: Spatial resolution of anthropogenic heat fluxes into urban aquifers, Sci. Total Environ., 524–525, 427–439, doi:10.1016/j.scitotenv.2015.04.003, 2015.

Berg, S. J. and Illman, W. A.: Capturing aquifer heterogeneity: Comparison of approaches through controlled sandbox experiments, Water Resour. Res., 47(9), n/a-n/a, doi:10.1029/2011WR010429, 2011.

Berkowitz, B.: Characterizing flow and transport in fractured geological media: A review, Adv. Water Resour., 25(8–12), 861–884, doi:10.1016/S0309-1708(02)00042-8, 2002.

Bodin, T. and Sambridge, M.: Seismic tomography with the reversible jump algorithm, Geophys. J. Int., 178(3), 1411–1436, doi:10.1111/j.1365-246X.2009.04226.x, 2009.

Borg, I. and Groenen, P. J. F.: Modern multidimensional scaling: Theory and applications, Springer Science & Business Media., 2005.

Le Borgne, T., Bour, O., Riley, M. S., Gouze, P., Pezard, P. A., Belghoul, A., Lods, G., Le Provost, R., Greswell, R. B., Ellis, P. A., Isakov, E. and Last, B. J.: Comparison of alternative methodologies for identifying and characterizing preferential flow paths in heterogeneous aquifers, J. Hydrol., 345(3–4), 134–148, doi:10.1016/j.jhydrol.2007.07.007, 2007.

Bossart, P. and Mazurek, M.: Structural Geology and Water Flow-Paths in the Migration Shear Zone, Wettingen., 1991.

Brauchler, R., Liedl, R. and Dietrich, P.: A travel time based hydraulic tomographic approach, Water Resour. Res., 39(12), doi:10.1029/2003WR002262, 2003.

Brauchler, R., Cheng, J.-T., Dietrich, P., Everett, M., Johnson, B., Liedl, R. and Sauter, M.: An inversion strategy for hydraulic tomography: Coupling travel time and amplitude inversion, J. Hydrol., 345(3–4), 184–198, doi:10.1016/j.jhydrol.2007.08.011, 2007.

Brauchler, R., Hu, R., Dietrich, P. and Sauter, M.: A field assessment of high-resolution aquifer characterization based on hydraulic travel time and hydraulic attenuation tomography, Water Resour. Res., 47(3), doi:10.1029/2010WR009635, 2011.

Brauchler, R., Böhm, G., Leven, C., Dietrich, P. and Sauter, M.: A laboratory study of tracer tomography, Hydrogeol. J., 21(6), 1265–1274, doi:10.1007/s10040-013-1006-z, 2013a.

Brauchler, R., Hu, R., Hu, L., Jiménez, S., Bayer, P., Dietrich, P. and Ptak, T.: Rapid field application of hydraulic tomography for resolving aquifer heterogeneity in unconsolidated sediments, Water Resour. Res., 49(4), 2013–2024, doi:10.1002/wrcr.20181, 2013b.

Brooks, A. N. and Hughes, T. J. R.: Streamline upwind/Petrov-Galerkin formulations for convection dominated flows with particular emphasis on the incompressible Navier-Stokes equations, Comput. Methods Appl. Mech. Eng., 32(1–3), 199–259, doi:10.1016/0045-7825(82)90071-8, 1982.

Butler, J. J., McElwee, C. D. and Bohling, G. C.: Pumping tests in networks of multilevel sampling wells: Motivation and methodology, Water Resour. Res., 35(11), 3553–3560, doi:10.1029/1999WR900231, 1999.

Caers, J., Park, K. and Scheidt, C.: Modeling Uncertainty of Complex Earth Systems in Metric Space, in Handbook of Geomathematics, pp. 865–889, Springer Berlin Heidelberg, Berlin, Heidelberg., 2010.

Cardiff, M., Barrash, W., Kitanidis, P. K., Malama, B., Revil, A., Straface, S. and Rizzo, E.: A Potential-Based Inversion of Unconfined Steady-State Hydraulic Tomography, Ground Water, 47(2), 259–270, doi:10.1111/j.1745-6584.2008.00541.x, 2009.

Cardiff, M., Barrash, W. and Kitanidis, P. K.: A field proof-of-concept of aquifer imaging using 3-D transient hydraulic tomography with modular, temporarily-emplaced equipment, Water Resour. Res., 48(5), doi:10.1029/2011WR011704, 2012.

Cardiff, M., Barrash, W. and Kitanidis, P. K.: Hydraulic conductivity imaging from 3-D transient hydraulic tomography at several pumping/observation densities, Water Resour. Res., 49(11), 7311–7326, doi:10.1002/wrcr.20519, 2013.

Castagna, M., Becker, M. W. and Bellin, A.: Joint estimation of transmissivity and storativity in a bedrock fracture, Water Resour. Res., 47(9), 1–19, doi:10.1029/2010WR009262, 2011.

Cherubini, C., Pastore, N., Giasi, C. I. and Allegretti, N. M.: Laboratory experimental investigation of heat transport in fractured media, Nonlinear Process. Geophys., 24(1), 23–42, doi:10.5194/npg-24-23-2017, 2017.

Childs, C., Manzocchi, T., Walsh, J. J., Bonson, C. G., Nicol, A. and Schöpfer, M. P. J.: A geometric model of fault zone and fault rock thickness variations, J. Struct. Geol., 31(2), 117–127, doi:10.1016/j.jsg.2008.08.009, 2009.

Coleman, T. I., Parker, B. L., Maldaner, C. H. and Mondanos, M. J.: Groundwater flow characterization in a fractured bedrock aquifer using active DTS tests in sealed boreholes, J. Hydrol., 528, 449–462, doi:10.1016/j.jhydrol.2015.06.061, 2015.

Colombani, N., Giambastiani, B. M. S. and Mastrocicco, M.: Combined use of heat and saline tracer to estimate aquifer properties in a forced gradient test, J. Hydrol., 525, 650–657, doi:10.1016/j.jhydrol.2015.04.026, 2015.

Comunian, a., Renard, P., Straubhaar, J. and Bayer, P.: Three-dimensional high resolution fluvio-glacial aquifer analog - Part 2: Geostatistical modeling, J. Hydrol., 405(1–2), 10–23, doi:10.1016/j.jhydrol.2011.03.037, 2011.

Coscia, I., Greenhalgh, S. a., Linde, N., Doetsch, J., Marescot, L., Günther, T., Vogt, T. and Green, A. G.: 3D crosshole ERT for aquifer characterization and monitoring of infiltrating river water, Geophysics, 76(2), G49, 2011.

Dadi, S., Gibson Jr., R. L. and Wang, K.: Quantification of uncertainty in velocity log upscaling using reversible jump MCMC, in SEG Technical Program Expanded Abstracts

2015, pp. 3476–3481, Society of Exploration Geophysicists., 2015.

Dagan, G.: Time-dependent macrodispersion for solute transport in anisotropic heterogeneous aquifers, Water Resour. Res., 24(9), 1491–1500, doi:10.1029/WR024i009p01491, 1988.

Datta-Gupta, A.: Inverse modeling of partitioning interwell tracer tests: A streamline approach, Water Resour. Res., 38(6), doi:10.1029/2001WR000597, 2002.

Datta-Gupta, A., Vasco, D. W. and Long, J. C. .: Detailed Characterization of a Fractured Limestone Formation by Use of Stochastic Inverse Approaches, SPE Form. Eval., 10(3), 133–140, doi:10.2118/27744-PA, 1995.

Datta-Gupta, A., Yoon, S., Vasco, D. W. and Pope, G. A.: Inverse modeling of partitioning interwell tracer tests: A streamline approach, Water Resour. Res., 38(6), 15-1-15–17, doi:10.1029/2001WR000597, 2002.

Day-Lewis, F. D., Hsieh, P. A. and Gorelick, S. M.: Identifying fracture-zone geometry using simulated annealing and hydraulic-connection data, Water Resour. Res., 36(7), 1707–1721, doi:10.1029/2000WR900073, 2000.

Dettmer, J. and Dosso, S. E.: Trans-dimensional matched-field geoacoustic inversion with hierarchical error models and interacting Markov chains., J. Acoust. Soc. Am., 132(4), 2239–50, doi:10.1121/1.4746016, 2012.

Deuber, C. A., Kittilae, A., Somogyvári, M., Mikutis, G., Bayer, P., Stark, W. J. and Saar, M. O.: DNA-labeled silica nanoparticles as subsurface fluid flow tracers, Water Resour. Res., 2017.

Diersch, H.-J. G.: FEFLOW Finite Element Modeling of Flow, Mass and Heat Transport on Porous and Fractured Media, Springer Science & Business Media., 2014.

Djibrilla Saley, A., Jardani, A., Soueid Ahmed, A., Raphael, A. and Dupont, J. P.: Hamiltonian Monte Carlo algorithm for the characterization of hydraulic conductivity from the heat tracing data, Adv. Water Resour., 97, 120–129, doi:10.1016/j.advwatres.2016.09.004, 2016.

Doetsch, J., Linde, N., Coscia, I., Greenhalgh, S. a. and Green, A. G.: Zonation for 3D aquifer characterization based on joint inversions of multimethod crosshole geophysical data, GEOPHYSICS, 75(6), G53–G64, doi:10.1190/1.3496476, 2010.

Doherty, J.: Ground water model calibration using pilot points and regularization, Ground Water, 41(2), 170–177, doi:10.1111/j.1745-6584.2003.tb02580.x, 2003.

Dorn, C., Linde, N., Borgne, T. Le, Bour, O. and de Dreuzy, J. R.: Conditioning of stochastic 3-D fracture networks to hydrological and geophysical data, Adv. Water Resour., 62(PA), 79–89, doi:10.1016/j.advwatres.2013.10.005, 2013.

Doro, K. O., Cirpka, O. a and Leven, C.: Tracer Tomography: Design Concepts and Field Experiments Using Heat as a Tracer, Groundwater, 53(S1), 139–148, doi:10.1111/gwat.12299, 2015.

Einarson, M. D. and Cherry, J. A.: A New Multilevel Ground Water Monitoring System Using Multichannel Tubing, Ground Water Monit. Remediat., 22(4), 52–65, doi:10.1111/j.1745-6592.2002.tb00771.x, 2002.

Evans, G. V.: Tracer techniques in hydrology, Int. J. Appl. Radiat. Isot., 34(1), 451–475, doi:10.1016/0020-708X(83)90144-8, 1983.

Fatemi, E., Engquist, B. and Osher, S.: Numerical Solution of the High Frequency Asymptotic Expansion for the Scalar Wave Equation, J. Comput. Phys., 120(1), 145–155, doi:10.1006/jcph.1995.1154, 1995.

Feehley, C. E., Zheng, C. and Molz, F. J.: A dual-domain mass transfer approach for modeling solute transport in heterogeneous aquifers: Application to the Macrodispersion Experiment (MADE) site, Water Resour. Res., 36(9), 2501–2515, doi:10.1029/2000WR900148, 2000.

Fox, M., Bodin, T. and Shuster, D. L.: Abrupt changes in the rate of Andean Plateau uplift from reversible jump Markov Chain Monte Carlo inversion of river profiles, Geomorphology, 238, 1–14, doi:10.1016/j.geomorph.2015.02.022, 2015.

Frampton, A. and Cvetkovic, V.: Inference of field-scale fracture transmissivities in crystalline rock using flow log measurements, Water Resour. Res., 46(11), 1–17, doi:10.1029/2009WR008367, 2010.

Francis, A. M.: Understanding stochastic inversion: part 1, First Break, 24(1101), 79–84, doi:10.3997/1365-2397.2006026, 2006.

Franssen, H. J. W. M. H. and Gómez-Hernández, J. J.: 3D inverse modelling of groundwater flow at a fractured site using a stochastic continuum model with multiple statistical populations, Stoch. Environ. Res. Risk Assess., 16(2), 155–174, doi:10.1007/s00477-002-0091-7, 2002.

Freeze, R. A. and Witherspoon, P. A.: Theoretical analysis of regional groundwater flow: 2. Effect of water-table configuration and subsurface permeability variation, Water Resour. Res., 3(2), 623–634, doi:10.1029/WR003i002p00623, 1967.

Gelman, A., Carlin, J. B., Stern, H. S. and Rubin, D. B.: Bayesian Data Analysis., 2004.

Geyer, C.: Introduction to Markov Chain Monte Carlo, in Handbook of Markov Chain Monte Carlo, vol. 20116022, edited by S. Brooks, A. Gelman, G. Jones, and X.-L. Meng, p. 45, Chapman and Hall/CRC., 2011.

Le Goc, R., de Dreuzy, J.-R. and Davy, P.: An inverse problem methodology to identify flow channels in fractured media using synthetic steady-state head and geometrical data, Adv. Water Resour., 33(7), 782–800, doi:10.1016/j.advwatres.2010.04.011, 2010.

Green, P. J.: Reversible jump Markov chain monte carlo computation and Bayesian model determination, Biometrika, 82(4), 711–732, doi:10.1093/biomet/82.4.711, 1995.

Hao, Y., Yeh, T.-C. J., Xiang, J., Illman, W. A., Ando, K., Hsu, K.-C. and Lee, C.-H.: Hydraulic Tomography for Detecting Fracture Zone Connectivity, Ground Water, 46(2), 183–192, doi:10.1111/j.1745-6584.2007.00388.x, 2008.

Hart, P. E., Nilsson, N. J. and Raphael, B.: A Formal Basis for the Heuristic Determination of Minimum Cost Paths, IEEE Trans. Syst. Sci. Cybern., 4(2), 100–107, doi:10.1109/TSSC.1968.300136, 1968.

Hawkins, A., Fox, D., Zhao, R., Tester, J. W., Cathles, L., Koch, D. and Becker, M.: Predicting Thermal Breakthrough from Tracer Tests: Simulations and Observations in a Low-Temperature Field Laboratory, Proceedings, 40th Work. Geotherm. Reserv. Eng. Stanford Univ., 1–15, 2015.

Hermans, T., Nguyen, F., Robert, T. and Revil, A.: Geophysical Methods for Monitoring Temperature Changes in Shallow Low Enthalpy Geothermal Systems, Energies, 7(8), 5083–5118, doi:10.3390/en7085083, 2014.

Hermans, T., Wildemeersch, S., Jamin, P., Orban, P., Brouyère, S., Dassargues, A. and Nguyen, F.: Quantitative temperature monitoring of a heat tracing experiment using cross-borehole ERT, Geothermics, 53, 14–26, doi:10.1016/j.geothermics.2014.03.013, 2015.

Hestir, K., Martel, S. J., Vail, S., Long, J., D'Onfro, P. and Rizer, W. D.: Inverse hydrologic modeling using stochastic growth algorithms, Water Resour. Res., 34(12), 3335–3347, doi:10.1029/98WR01549, 1998.

Hestir, K., Martel, S. J., Yang, J., Evans, J. P., Long, J. O. S., D'Onfro, P. and Rizer, W. D.: Use of conditional simulation, mechanical theory, and field observations to characterize the structure of faults and fracture networks, pp. 61–73., 2001.

Hidalgo, J. J., Carrera, J. and Dentz, M.: Steady state heat transport in 3D heterogeneous porous media, Adv. Water Resour., 32(8), 1206–1212, doi:10.1016/j.advwatres.2009.04.003, 2009.

Höyng, D., D'Affonseca, F. M., Bayer, P., de Oliveira, E. G., Perinotto, J. A. J., Reis, F., Weiß, H. and Grathwohl, P.: High-resolution aquifer analog of fluvial-aeolian sediments of the Guarani aquifer system, Environ. Earth Sci., 71, 3081–3094, doi:10.1007/s12665-013-2684-5, 2014.

Hu, L., Bayer, P., Alt-Epping, P., Tatomir, A., Sauter, M. and Brauchler, R.: Time-lapse pressure tomography for characterizing CO2 plume evolution in a deep saline aquifer, Int. J. Greenh. Gas Control, 39, 91–106, doi:10.1016/j.ijggc.2015.04.013, 2015.

Hu, R., Brauchler, R., Herold, M. and Bayer, P.: Hydraulic tomography analog outcrop study: Combining travel time and steady shape inversion, J. Hydrol., 409(1–2), 350–362, doi:10.1016/j.jhydrol.2011.08.031, 2011.

Illman, W. a., Berg, S. J., Liu, X. and Massi, A.: Hydraulic/Partitioning Tracer Tomography for DNAPL Source Zone Characterization: Small-Scale Sandbox Experiments, Environ. Sci. Technol., 44(22), 8609–8614, doi:10.1021/es101654j, 2010.

Illman, W. A.: Hydraulic tomography offers improved imaging of heterogeneity in fractured rocks, Groundwater, 52(5), 659–684, doi:10.1111/gwat.12119, 2014.

Illman, W. A. and Neuman, S. P.: Steady-state analysis of cross-hole pneumatic injection tests in unsaturated fractured tuff, J. Hydrol., 281(1–2), 36–54, doi:10.1016/S0022-1694(03)00199-9, 2003.

Illman, W. A., Liu, X., Takeuchi, S., Yeh, T.-C. J., Ando, K. and Saegusa, H.: Hydraulic tomography in fractured granite: Mizunami Underground Research site, Japan, Water Resour. Res., 45(1), n/a-n/a, doi:10.1029/2007WR006715, 2009a.

Illman, W. A., Liu, X., Takeuchi, S., Yeh, T.-C. J., Ando, K. and Saegusa, H.: Hydraulic tomography in fractured granite: Mizunami Underground Research site, Japan, Water Resour. Res., 45(1), n/a-n/a, doi:10.1029/2007WR006715, 2009b.

Illman, W. A., Berg, S. J. and Zhao, Z.: Should hydraulic tomography data be interpreted using geostatistical inverse modeling? A laboratory sandbox investigation, Water Resour. Res., 51(5), 3219–3237, doi:10.1002/2014WR016552, 2015.

Irvine, D. J., Simmons, C. T., Werner, A. D. and Graf, T.: Heat and Solute Tracers: How Do They Compare in Heterogeneous Aquifers?, Groundwater, 53, 10–20, doi:10.1111/gwat.12146, 2013.

Jackson, M. J. and Tweeton, D. R.: 3DTOM, Three-dimensional Geophysical Tomography, US Department of the Interior, Bureau of Mines., 1996.

Jang, I. S., Kang, J. M. and Park, C. H.: Inverse Fracture Model Integrating Fracture Statistics and Well-testing Data, Energy Sources, Part A Recover. Util. Environ. Eff., 30(18), 1677–1688, doi:10.1080/15567030802087510, 2008.

Jardani, A., Revil, A. and Dupont, J. P.: Stochastic joint inversion of hydrogeophysical data for salt tracer test monitoring and hydraulic conductivity imaging, Adv. Water Resour., 52, 62–77, doi:10.1016/j.advwatres.2012.08.005, 2013.

Jiménez, S., Brauchler, R. and Bayer, P.: A new sequential procedure for hydraulic tomographic inversion, Adv. Water Resour., 62(PA), 59–70, doi:10.1016/j.advwatres.2013.10.002, 2013.

Jiménez, S., Brauchler, R., Hu, R., Hu, L., Schmidt, S., Ptak, T. and Bayer, P.: Prediction of solute transport in a heterogeneous aquifer utilizing hydraulic conductivity and specific storage tomograms, Water Resour. Res., 51(7), 5504–5520, doi:10.1002/2014WR016402, 2015.

Jiménez, S., Mariethoz, G., Brauchler, R. and Bayer, P.: Smart pilot points using reversible-jump Markov-chain Monte Carlo, Water Resour. Res., n/a-n/a, doi:10.1002/2015WR017922, 2016.

Jussel, P., Stauffer, F. and Dracos, T.: Transport modeling in heterogeneous aquifers: 1. Statistical description and numerical generation of gravel deposits, Water Resour. Res., 30(6), 1803–1817, doi:10.1029/94WR00162, 1994.

Keys, W. S. and Brown, R. F.: The Use of Temperature Logs to Trace the Movement of Injected Water, Ground Water, doi:10.1111/j.1745-6584.1978.tb03201.x, 1978.

Klepikova, M. V., Le Borgne, T., Bour, O., Gallagher, K., Hochreutener, R. and Lavenant, N.: Passive temperature tomography experiments to characterize transmissivity and connectivity of preferential flow paths in fractured media, J. Hydrol., 512, 549–562, doi:10.1016/j.jhydrol.2014.03.018, 2014.

Kline, M. and Kay, I. W.: Electromagnetic theory and geometrical optics, , xii, 527 [online] Available from: http://catalog.hathitrust.org/Record/001480567, 1965.

Kolyukhin, D. and Torabi, A.: Statistical analysis of the relationships between faults attributes, J. Geophys. Res. Solid Earth, 117(B5), n/a-n/a, doi:10.1029/2011JB008880, 2012.

Kolyukhin, D. and Torabi, A.: Power-Law Testing for Fault Attributes Distributions, Pure Appl. Geophys., 170(12), 2173–2183, doi:10.1007/s00024-013-0644-3, 2013.

Kowalsky, M. B., Finsterle, S., Williams, K. H., Murray, C., Commer, M., Newcomer, D., Englert, A., Steefel, C. I. and Hubbard, S. S.: On parameterization of the inverse problem for estimating aquifer properties using tracer data, Water Resour. Res., 48(6), W06535, doi:10.1029/2011WR011203, 2012.

Leaf, A. T., Hart, D. J. and Bahr, J. M.: Active Thermal Tracer Tests for Improved Hydrostratigraphic Characterization, Ground Water, 50(5), 726–735, doi:10.1111/j.1745-6584.2012.00913.x, 2012.

Li, Z. Y., Zhao, J. H., Qiao, X. H. and Zhang, Y. X.: An automated approach for conditioning discrete fracture network modelling to *in situ* measurements, Aust. J. Earth Sci., 61(5), 755–763, doi:10.1080/08120099.2014.920726, 2014.

Linde, N., Chen, J., Kowalsky, M. B. and Hubbard, S.: HYDROGEOPHYSICAL PARAMETER ESTIMATION APPROACHES FOR FIELD SCALE CHARACTERIZATION, in Applied Hydrogeophysics, vol. i, pp. 9–44, Springer

Netherlands, Dordrecht., 2006.

Long, J. C. S., Remer, J. S., Wilson, C. R. and Witherspoon, P. A.: Porous media equivalents for networks of discontinuous fractures, Water Resour. Res., 18(3), 645–658, doi:10.1029/WR018i003p00645, 1982.

Ma, R. and Zheng, C.: Effects of Density and Viscosity in Modeling Heat as a Groundwater Tracer, Ground Water, 48(3), 380–389, doi:10.1111/j.1745-6584.2009.00660.x, 2010.

Ma, R., Zheng, C., Zachara, J. M. and Tonkin, M.: Utility of bromide and heat tracers for aquifer characterization affected by highly transient flow conditions, Water Resour. Res., 48(8), doi:10.1029/2011WR011281, 2012.

Macfarlane, P. A., Förster, A., Merriam, D. F., Schrötter, J. and Healey, J. M.: Monitoring artificially stimulated fluid movement in the Cretaceous Dakota aquifer, western Kansas, Hydrogeol. J., 10(6), 662–673, doi:10.1007/s10040-002-0223-7, 2002.

Malinverno, A. and Leaney, W. S.: Monte-Carlo Bayesian look-ahead inversion of walkaway vertical seismic profiles, Geophys. Prospect., 53(5), 689–703, doi:10.1111/j.1365-2478.2005.00496.x, 2005.

Mardia, K. V., Nyirongo, V. B., Walder, A. N., Xu, C., Dowd, P. A., Fowell, R. J. and Kent, J. T.: Markov Chain Monte Carlo implementation of rock fracture modelling, Math. Geol., 39(4), 355–381, doi:10.1007/s11004-007-9099-3, 2007.

de Marsily, G., Lavedan, G., Boucher, M. and Fasanino, G.: Interpretation of interference tests in a well field using geostatistical techniques to fit the permeability distribution in a reservoir model, Geostatistics Nat. Resour. Charact. Part, 2, 831–849, 1984.

Martinez-Landa, L. and Carrera, J.: A methodology to interpret cross-hole tests in a granite block, J. Hydrol., 325(1–4), 222–240, doi:10.1016/j.jhydrol.2005.10.017, 2006.

Mauldon, A. D., Karasaki, K., Martel, S. J., Long, J. C. S., Landsfeld, M., Mensch, A. and Vomvoris, S.: An inverse technique for developing models for fluid flow in fracture systems using simulated annealing, Water Resour. Res., 29(11), 3775–3789, doi:10.1029/93WR00664, 1993.

Meier, P. M., Medina, A. and Carrera, J.: Geostatistical Inversion of Cross-Hole Pumping Tests for Identifying Preferential Flow Channels Within a Shear Zone, Ground Water, 39(1), 10–17, doi:10.1111/j.1745-6584.2001.tb00346.x, 2001.

Menke, W.: Geophysical Data Analysis: Discrete Inverse Theory Academic, New York, 1984.

Molson, J. W., Frind, E. O. and Palmer, C. D.: Thermal energy storage in an unconfined aquifer: 2. Model development, validation, and application, Water Resour. Res., 28(10), 2857–2867, doi:10.1029/92WR01472, 1992.

Molz, F. J., Parr, a. D. and Andersen, P. F.: Thermal energy storage in a confined aquifer: Second cycle, Water Resour. Res., 17(3), 641, doi:10.1029/WR017i003p00641, 1981.

Mondal, A., Efendiev, Y., Mallick, B. and Datta-Gupta, A.: Bayesian uncertainty quantification for flows in heterogeneous porous media using reversible jump Markov chain Monte Carlo methods, Adv. Water Resour., 33(3), 241–256, doi:10.1016/j.advwatres.2009.10.010, 2010.

Neretnieks, I.: Diffusion in the rock matrix: An important factor in radionuclide retardation?, J. Geophys. Res. Solid Earth, 85(B8), 4379–4397, doi:10.1029/JB085iB08p04379, 1980.

Neuman, S. P.: Stochastic Continuum Representation of Fractured Rock Permeability as an Alternative to the REV and Fracture Network Concepts, in Groundwater Flow and Quality Modelling, pp. 331–362, Springer Netherlands, Dordrecht., 1988.

Neuman, S. P.: Trends, prospects and challenges in quantifying flow and transport through fractured rocks, Hydrogeol. J., 13(1), 124–147, doi:10.1007/s10040-004-0397-2, 2005.

Ni, C. F. and Yeh, T. C. J.: Stochastic inversion of pneumatic cross-hole tests and barometric pressure fluctuations in heterogeneous unsaturated formations, Adv. Water Resour., 31(12), 1708–1718, doi:10.1016/j.advwatres.2008.08.007, 2008.

Niven, E. B. and Deutsch, C. V.: Non-random Discrete Fracture Network Modeling, in Quantitative Geology and Geostatistics, vol. 17, edited by P. Abrahamsen, R. Hauge, and O. Kolbjørnsen, pp. 275–286, Springer Netherlands, Dordrecht., 2012.

Noetinger, B., Roubinet, D., Russian, A., Le Borgne, T., Delay, F., Dentz, M., de Dreuzy, J.-R. and Gouze, P.: Random Walk Methods for Modeling Hydrodynamic Transport in Porous and Fractured Media from Pore to Reservoir Scale, Transp. Porous Media, 115(2), 345–385, doi:10.1007/s11242-016-0693-z, 2016.

Nolet, G.: Seismic Tomography, edited by G. Nolet, Springer Netherlands, Dordrecht., 1987.

Ogata, A. and Banks, R. B.: A solution of the differential equation of longitudinal dispersion in porous media, U. S. Geol. Surv. Prof. Pap. 411-A, 1961.

Oppenheim, A. V. and Lim, J. S.: The Importance of Phase in Signals, Proc. IEEE, 69(5), 529–541, doi:10.1109/PROC.1981.12022, 1981.

Palmer, C. D., Blowes, D. W., Frind, E. O. and Molson, J. W.: Thermal energy storage in an unconfined aquifer: 1. Field Injection Experiment, Water Resour. Res., 28(10), 2845–2856, doi:10.1029/92WR01471, 1992.

Paradis, D., Gloaguen, E., Lefebvre, R. and Giroux, B.: Resolution analysis of tomographic slug test head data: Two-dimensional radial case, Water Resour. Res., 51(4), 2356–2376, doi:10.1002/2013WR014785, 2015.

La Pointe, P. R.: A method to characterize fracture density and connectivity through fractal geometry, Int. J. Rock Mech. Min. Sci. Geomech. Abstr., 25(6), 421–429, doi:10.1016/0148-9062(88)90982-5, 1988.

Rau, G. C., Andersen, M. S., McCallum, A. M., Roshan, H. and Acworth, R. I.: Heat as a tracer to quantify water flow in near-surface sediments, Earth-Science Rev., 129, 40–58, doi:10.1016/j.earscirev.2013.10.015, 2014.

Raymond, J., Therrien, R., Gosselin, L. and Lefebvre, R.: A Review of Thermal Response Test Analysis Using Pumping Test Concepts, Ground Water, 49(6), 932–945, doi:10.1111/j.1745-6584.2010.00791.x, 2011.

Read, T., Bour, O., Bense, V., Le Borgne, T., Goderniaux, P., Klepikova, M. V., Hochreutener, R., Lavenant, N. and Boschero, V.: Characterizing groundwater flow and heat transport in fractured rock using fiber-optic distributed temperature sensing, Geophys. Res. Lett., 40(10), 2055–2059, doi:10.1002/grl.50397, 2013.

Read, T., Bense, V. F., Hochreutener, R., Bour, O., Le Borgne, T., Lavenant, N. and Selker, J. S.: Thermal-plume fibre optic tracking (T-POT) test for flow velocity measurement in groundwater boreholes, Geosci. Instrumentation, Methods Data Syst., 4(2), 197–202, doi:10.5194/gi-4-197-2015, 2015.

Reist, F.: Characterization of unconsolidated sediments based on hydraulic and tracer testing

at the test site Widen , Thur valley., Master thesis, ETH Zürich, (August), 2013.

Russo: Advective Heat Transport in an Unconfined Aquifer Induced by the Field Injection of an Open-Loop Groundwater Heat Pump, Am. J. Environ. Sci., 6(3), 253–259, doi:10.3844/ajessp.2010.253.259, 2010.

Saar, M. O.: Review: Geothermal heat as a tracer of large-scale groundwater flow and as a means to determine permeability fields, Hydrogeol. J., 19(1), 31–52, doi:10.1007/s10040-010-0657-2, 2011.

Sahimi, M.: Flow and transport in porous media and fractured rock: from classical methods to modern approaches, John Wiley & Sons., 2011.

Sambridge, M., Bodin, T., Gallagher, K. and Tkalcic, H.: Transdimensional inference in the geosciences, Philos. Trans. R. Soc. A Math. Phys. Eng. Sci., 371(1984), 20110547–20110547, doi:10.1098/rsta.2011.0547, 2012.

Sanchez-León, E., Leven, C., Haslauer, C. P. and Cirpka, O. A.: Combining 3D Hydraulic Tomography with Tracer Tests for Improved Transport Characterization, Groundwater, 54(4), 498–507, doi:10.1111/gwat.12381, 2016.

Sauty, J. P., Gringarten, A. C., Menjoz, A. and Landel, P. A.: Sensible energy storage in aquifers: 1. Theoretical study, Water Resour. Res., 18(2), 245, doi:10.1029/WR018i002p00245, 1982a.

Sauty, J. P., Gringarten, A. C., Fabris, H., Thiery, D., Menjoz, A. and Landel, P. A.: Sensible energy storage in aquifers: 2. Field experiments and comparison with theoretical results, Water Resour. Res., 18(2), 253–265, doi:10.1029/WR018i002p00253, 1982b.

Schincariol, R. A. and Schwartz, F. W.: An experimental investigation of variable density flow and mixing in homogeneous and heterogeneous media, Water Resour. Res., 26(10), 2317–2329, doi:10.1029/90WR01161, 1990.

Schöniger, A., Nowak, W. and Hendricks Franssen, H.-J.: Parameter estimation by ensemble Kalman filters with transformed data: Approach and application to hydraulic tomography, Water Resour. Res., 48(4), n/a-n/a, doi:10.1029/2011WR010462, 2012.

Schwede, R. L., Li, W., Leven, C. and Cirpka, O. a.: Three-dimensional geostatistical inversion of synthetic tomographic pumping and heat-tracer tests in a nested-cell setup, Adv. Water Resour., 63, 77–90, doi:10.1016/j.advwatres.2013.11.004, 2014.

Schweingruber, M.: Developing an active thermal tracer test for characterization of heterogeneity in an alluvial aquifer, Master thesis, ETH Zürich, 2014.

Schweingruber, M., Somogyvári, M. and Bayer, P.: Active thermal tracer testing in a shallow aquifer of the Thur valley, Switzerland, in EGU General Assembly Conference Abstracts, vol. 17, p. 9590., 2015.

Seibertz, K. S. O., Chirila, M. A., Bumberger, J., Dietrich, P. and Vienken, T.: Development of in-aquifer heat testing for high resolution subsurface thermal-storage capability characterisation, J. Hydrol., 534, 113–123, doi:10.1016/j.jhydrol.2015.12.013, 2016.

Sharmeen, R., Illman, W. A., Berg, S. J., Yeh, T.-C. J., Park, Y.-J., Sudicky, E. A. and Ando, K.: Transient hydraulic tomography in a fractured dolostone: Laboratory rock block experiments, Water Resour. Res., 48(10), n/a-n/a, doi:10.1029/2012WR012216, 2012.

Shewchuk, J. R.: Triangle: Engineering a 2D Quality Mesh Generator and Delaunay Triangulator, Appl. Comput. Geom. Towar. Geom. Eng., 1148, 203–222, doi:10.1007/BFb0014497, 1996.

Shook, G. M.: PREDICTION OF THERMAL BREAKTHROUGH FROM TRACER TESTS, in Twenty-Fourth Workshop on Geothermal Reservoir Engineering., 1999.

Shook, G. M.: Predicting thermal breakthrough in heterogeneous media from tracer tests, Geothermics, 30(6), 573–589, 2001.

Somogyvári, M., Bayer, P. and Brauchler, R.: Travel-time-based thermal tracer tomography, Hydrol. Earth Syst. Sci., 20(5), 1885–1901, doi:10.5194/hess-20-1885-2016, 2016.

Stauffer, F., Bayer, P., Blum, P., Giraldo, N. M. and Kinzelbach, W.: Thermal use of shallow groundwater, CRC Press., 2013.

Thum, P. and Stüben, K.: Advanced algebraic multigrid application for the acceleration of groundwater simulations, XIX Int. Conf. Water Recources, 8, 2012.

Torabi, A. and Berg, S. S.: Scaling of fault attributes: A review, Mar. Pet. Geol., 28(8), 1444–1460, doi:10.1016/j.marpetgeo.2011.04.003, 2011.

Valley, B. C.: The relation between natural fracturing and stress heterogeneities in deep-seated crystalline rocks at Soultz-sous-Forêts (France)., ETH Reprozentrale Hönggerberg, HIL C45, Zürich (2007). http//dx.doi.org/10.3929/ethz-a-005562794, (17385), 260, doi:10.3929/ethz-a-005562794, 2007.

Vandenbohede, A., Van Houtte, E. and Lebbe, L.: Study of the feasibility of an aquifer storage and recovery system in a deep aquifer in Belgium, Hydrol. Sci. J., 53(4), 844–856, doi:10.1623/hysj.53.4.844, 2008.

Vandenbohede, A., Hermans, T., Nguyen, F. and Lebbe, L.: Shallow heat injection and storage experiment: Heat transport simulation and sensitivity analysis, J. Hydrol., 409(1–2), 262–272, doi:10.1016/j.jhydrol.2011.08.024, 2011.

Vasco, D. W. and Datta-Gupta, A.: Asymptotic solutions for solute transport: A formalism for tracer tomography, Water Resour. Res., 35(1), 1–16, doi:10.1029/98WR02742, 1999.

Vasco, D. W. and Finsterle, S.: Numerical trajectory calculations for the efficient inversion of transient flow and tracer observations, Water Resour. Res., 40(1), 1–17, doi:10.1029/2003wr002362, 2004.

Vasco, D. W., Keers, H. and Karasaki, K.: Estimation of reservoir properties using transient pressure data: An asymptotic approach, Water Resour. Res., 36(12), 3447–3465, doi:10.1029/2000WR900179, 2000.

Vesnaver, A. and Böhm, G.: Staggered or adapted grids for seismic tomography?, Lead. Edge, 19(9), 944, doi:10.1190/1.1438762, 2000.

Vesselinov, V. V, Neuman, S. P. and Illman, W. A.: Three-dimensional numerical inversion of pneumatic cross-hole tests in unsaturated fractured tuff: 1. Methodology and borehole effects, Water Resour. Res., 37(12), 3001–3017, doi:10.1029/2000WR000133, 2001a.

Vesselinov, V. V., Neuman, S. P. and Illman, W. A.: Three-dimensional numerical inversion of pneumatic cross-hole tests in unsaturated fractured tuff: 2. Equivalent parameters, high-resolution stochastic imaging and scale effects, Water Resour. Res., 37(12), 3019–3041, doi:10.1029/2000WR000135, 2001b.

Vesselinov, V. V., Neuman, S. P. and Illman, W. A.: Three-dimensional numerical inversion of pneumatic cross-hole tests in unsaturated fractured tuff: 2. Equivalent parameters, high-resolution stochastic imaging and scale effects, Water Resour. Res., 37(12), 3019–3041, doi:10.1029/2000WR000135, 2001c.

Wagner, V., Bayer, P., Bisch, G., Kübert, M. and Blum, P.: Hydraulic characterization of aquifers by thermal response testing: Validation by large-scale tank and field experiments, Water Resour. Res., 50(1), 71–85, doi:10.1002/2013WR013939, 2014a.

Wagner, V., Li, T., Bayer, P., Leven, C., Dietrich, P. and Blum, P.: Thermal tracer testing in a sedimentary aquifer:Field experiment (Lauswiesen, Germany) and numerical simulation, Hydrogeol. J., 22(1), 175–187, doi:10.1007/s10040-013-1059-z, 2014b.

Weisstein, E. W.: Lambert W-function, 2002.

Wildemeersch, S., Jamin, P., Orban, P., Hermans, T., Klepikova, M., Nguyen, F., Brouyère, S. and Dassargues, a.: Coupling heat and chemical tracer experiments for estimating heat transfer parameters in shallow alluvial aquifers, J. Contam. Hydrol., 169, 90–99, doi:10.1016/j.jconhyd.2014.08.001, 2014.

Xie, Y., Cook, P. G., Simmons, C. T. and Zheng, C.: On the limits of heat as a tracer to estimate reach-scale river-aquifer exchange flux, Water Resour. Res., 51(9), 7401–7416, doi:10.1002/2014WR016741, 2015.

Xue, Y., Xie, C. and Li, Q.: Aquifer thermal energy storage: A numerical simulation of field experiments in China, Water Resour. Res., 26(10), 2365–2375, doi:10.1029/WR026i010p02365, 1990.

Yeh, T.-C. J. and Liu, S.: Hydraulic tomography: Development of a new aquifer test method, Water Resour. Res., 36(8), 2095–2105, doi:10.1029/2000WR900114, 2000.

Yeh, T.-C. J. and Zhu, J.: Hydraulic/partitioning tracer tomography for characterization of dense nonaqueous phase liquid source zones, Water Resour. Res., 43(6), doi:10.1029/2006WR004877, 2007.

Yeh, T.-C. J., Jin, M. and Hanna, S.: An Iterative Stochastic Inverse Method: Conditional Effective Transmissivity and Hydraulic Head Fields, Water Resour. Res., 32(1), 85–92, doi:10.1029/95WR02869, 1996.

Yeh, W. W.: Review of Parameter Identification Procedures in Groundwater Hydrology: The Inverse Problem, Water Resour. Res., 22(2), 95–108, doi:10.1029/WR022i002p00095, 1986.

Yoon, H. and McKenna, S. A.: Highly parameterized inverse estimation of hydraulic conductivity and porosity in a three-dimensional, heterogeneous transport experiment, Water Resour. Res., 48(10), 1–17, doi:10.1029/2012WR012149, 2012.

Zha, Y., Yeh, T.-C. J., Illman, W. A., Tanaka, T., Bruines, P., Onoe, H. and Saegusa, H.: What does hydraulic tomography tell us about fractured geological media? A field study and synthetic experiments, J. Hydrol., 531, 17–30, doi:10.1016/j.jhydrol.2015.06.013, 2015.

Zha, Y., Yeh, T.-C. J., Illman, W. A., Tanaka, T., Bruines, P., Onoe, H., Saegusa, H., Mao, D., Takeuchi, S. and Wen, J.-C.: An Application of Hydraulic Tomography to a Large-Scale Fractured Granite Site, Mizunami, Japan, Groundwater, (August 2015), 1–12, doi:10.1111/gwat.12421, 2016.

Zhou, Y., Lim, D., Cupola, F. and Cardiff, M.: Aquifer imaging with pressure waves-Evaluation of low-impact characterization through sandbox experiments, Water Resour. Res., 52(3), 2141–2156, doi:10.1002/2015WR017751, 2016.

Zhu, J., Cai, X. and Jim Yeh, T.-C.: Analysis of tracer tomography using temporal moments of tracer breakthrough curves, Adv. Water Resour., 32(3), 391–400, doi:10.1016/j.advwatres.2008.12.001, 2009.

Ziegler, M., Loew, S. and Moore, J. R.: Distribution and inferred age of exfoliation joints in

the Aar Granite of the central Swiss Alps and relationship to Quaternary landscape evolution, Geomorphology, 201, 344–362, doi:10.1016/j.geomorph.2013.07.010, 2013.

Ziegler, M., Loew, S. and Bahat, D.: Growth of exfoliation joints and near-surface stress orientations inferred from fractographic markings observed in the upper Aar valley (Swiss Alps), Tectonophysics, 626, 1–20, doi:10.1016/j.tecto.2014.03.017, 2014.

Ziegler, M., Valley, B. and Evans, K. F.: Characterisation of Natural Fractures an Fracture Zones of the Basel EGS Reservoir inferred from Geophysical Logging of the Basel-1 Well, World Geotherm. Congr. April 19-25, Melbourne, Aust., (April), 19–25, 2015.

Márk Somogyvári

ETH Zürich, Engineering geology
Sonneggstrasse 5
8092 Zürich
Phone: +41-44-633-2286
E-mail: mark.somogyvari@erdw.ethz.ch
Citizen of Hungary

Research interests:

- Development of inversion methods to interpret tomographic experiments for aquifer characterization
- Transdimensional inversion methods to characterize discrete fracture networks based on flow and transport data
- Numerical modelling of flow and transport
- Geophysical inversion

Education:

2013 – 2017 PhD Student at ETH Zürich
PhD thesis: *"Thermal tracer tomography to characterize aquifer heterogeneity"*

2011 – 2013 MSc in Geophysics, Eötvös Loránd University, Budapest
MSc thesis: "*Petrophysical inversion of well log data with prior information*"

2008 – 2011 BSc in Earth Sciences, specialized in geophysics,
Eötvös Loránd University, Budapest
BSc thesis: "*Inversion of well log data with prior information*"

2004 – 2008 Fazekas Mihály High School, Budapest

Publications:

Somogyvári, Márk and Peter Bayer. "Field validation of thermal tracer tomography" *Water Resources Research* (under review)

Deuber, Claudia, Anniina Kittilae, Márk Somogyvári, Gediminas Mikutis, Wendelin Stark, Peter Bayer and Martin O. Saar. "DNA-labeled silica nanoparticles as subsurface fluid flow tracers" *Water Resources Research* (in preparation)

Somogyvári, Márk, Mohammadreza Jalali, Santos Jimenez Parras, and Peter Bayer. "Fracture network characterization with transdimensional inversion" *Water Resources Research* (under review)

Somogyvári, Márk, Peter Bayer, and Ralf Brauchler. "Travel-time-based thermal tracer tomography." *Hydrology and Earth System Sciences* 20.5 (2016): 1885-1901.

Conferences:

Somogyvári, Márk, Mohammadreza Jalali and Peter Bayer. "Fracture network characterization using a stochastic transdimensional algorithm." *14th Swiss Geoscience Meeting.* Geneva, Switzerland 2016.

Somogyvári, Márk, Mohammadreza Jalali and Peter Bayer. "Reconstruction of fracture network geometry using thermal tracer tomography." *ZHydro Conference.* Zürich, Switzerland 2016.

Somogyvári, Márk, Mohammadreza Jalali, Santos Jiménez Parras and Peter Bayer. "Advanced Geometrical Characterization of Fracture Networks via Tomographic Imaging" *43rd IAH Congress.* Montpellier, France 2016.

Somogyvári, Márk, et al. "Tracer tomography (in) rocks!" *EGU General Assembly Conference Abstracts*. Vol. 18. 2016.

Somogyvári, Márk, Ralf Brauchler, and Peter Bayer. "Thermal tracer tomography: from numerical simulation to field implementation." *EGU General Assembly Conference Abstracts*. Vol. 18. 2016.

Somogyvári, Márk, Peter Bayer, and Ralf Brauchler. "A New Concept for Thermal Tracer Tomography to Identify Heterogeneous Aquifer Structures." *AGU Fall Meeting Abstracts*. 2015.

Somogyvári, Márk, Mohammadreza Jalali, Santos Jiménez Parras and Peter Bayer. "From Stochastic toward Deterministic Characterization of Discrete Fracture Network via Thermal Tracer Tests." *AGU Fall Meeting Abstracts*. 2015.

Somogyvári, Márk, Mohammadreza Jalali, Santos Jiménez Parras and Peter Bayer. "A Stochastic Approach to Characterize Discrete Fracture Network Patterns." *The MADE Challenge for Groundwater Transport in Highly Heterogeneous Aquifers: Insights from 30 Years of Modeling and Characterization at the Field Scale and Promising Future Directions, AGU Chapman Conference.* Valencia, Spain 2015.

Schweingruber, Mischa, Márk Somogyvári, and Peter Bayer. "Active thermal tracer testing in a shallow aquifer of the Thur valley, Switzerland." *EGU General Assembly Conference Abstracts*. Vol. 17. 2015.

Somogyvári, Márk, Peter Bayer, and Ralf Brauchler. "Tomographic inversion of active thermal tracer experiments to characterize aquifer heterogeneity." *EGU General Assembly Conference Abstracts*. Vol. 17. 2015.

Somogyvári, Márk, Peter Bayer, and Ralf Brauchler. "Tomographic thermal tracer investigation of aquifer heterogeneity." *ZHydro Seminar Day 2014.* Zürich, Switzerland 2014.

Somogyvári, Márk. "Petrophysical inversion of well log data with apriori information." *Ifjú Szakemberek Ankétja – Meeting of Young Geoscientists.* Békéscsaba, Hungary 2013.

Somogyvári Márk "Szénhidrogén kutató fúrásokban végzett geofizikai mérések inverziója apriori információk segítségével" *Inverziós Ankét,* Miskolc, Hungary 2011.

Somogyvári, Márk and László Balázs. "Inversion of Well Log Data with Apriori Information." *6th Congress of Balkan Geophysical Society,* Budapest, Hungary 2011.

Somogyvári, Márk. "Inversion of well log data with apriori information." *Ifjú Szakemberek Ankétja – Meeting of Young Geoscientists*, Győr, Hungary 2011.